

Master Thesis

**Modeling and Validation
of Reflecting Metasurfaces for
Improved mmWave Coverage**

Padmashree Reddy Malur Vemana, B.Tech.

Supervisors : Prof. Dr.-Ing. Christian Wietfeld
 Simon Häger, M.Sc.
Submission Date : January 26, 2024

Eidesstattliche Versicherung

(Affidavit)

Malur Vemana, Padmashree Reddy

223181

Name, Vorname
(surname, first name)

Matrikelnummer
(student ID number)

Bachelorarbeit
(Bachelor's thesis)

Masterarbeit
(Master's thesis)

Titel
(Title)

Modeling and Validation of Reflecting Metasurfaces for Improved mmWave
Coverage

Ich versichere hiermit an Eides statt, dass ich die vorliegende Abschlussarbeit mit dem oben genannten Titel selbstständig und ohne unzulässige fremde Hilfe erbracht habe. Ich habe keine anderen als die angegebenen Quellen und Hilfsmittel benutzt sowie wörtliche und sinngemäße Zitate kenntlich gemacht. Die Arbeit hat in gleicher oder ähnlicher Form noch keiner Prüfungsbehörde vorgelegen.

I declare in lieu of oath that I have completed the present thesis with the above-mentioned title independently and without any unauthorized assistance. I have not used any other sources or aids than the ones listed and have documented quotations and paraphrases as such. The thesis in its current or similar version has not been submitted to an auditing institution before.

Dortmund, 26.01.2024

Ort, Datum
(place, date)

Unterschrift
(signature)

Belehrung:

Wer vorsätzlich gegen eine die Täuschung über Prüfungsleistungen betreffende Regelung einer Hochschulprüfungsordnung verstößt, handelt ordnungswidrig. Die Ordnungswidrigkeit kann mit einer Geldbuße von bis zu 50.000,00 € geahndet werden. Zuständige Verwaltungsbehörde für die Verfolgung und Ahndung von Ordnungswidrigkeiten ist der Kanzler/die Kanzlerin der Technischen Universität Dortmund. Im Falle eines mehrfachen oder sonstigen schwerwiegenden Täuschungsversuches kann der Prüfling zudem exmatrikuliert werden. (§ 63 Abs. 5 Hochschulgesetz - HG -).

Die Abgabe einer falschen Versicherung an Eides statt wird mit Freiheitsstrafe bis zu 3 Jahren oder mit Geldstrafe bestraft.

Die Technische Universität Dortmund wird ggf. elektronische Vergleichswerkzeuge (wie z.B. die Software „turnitin“) zur Überprüfung von Ordnungswidrigkeiten in Prüfungsverfahren nutzen.

Die oben stehende Belehrung habe ich zur Kenntnis genommen:

Official notification:

Any person who intentionally breaches any regulation of university examination regulations relating to deception in examination performance is acting improperly. This offense can be punished with a fine of up to EUR 50,000.00. The competent administrative authority for the pursuit and prosecution of offenses of this type is the Chancellor of TU Dortmund University. In the case of multiple or other serious attempts at deception, the examinee can also be unenrolled, Section 63 (5) North Rhine-Westphalia Higher Education Act (*Hochschulgesetz, HG*).

The submission of a false affidavit will be punished with a prison sentence of up to three years or a fine.

As may be necessary, TU Dortmund University will make use of electronic plagiarism-prevention tools (e.g. the "turnitin" service) in order to monitor violations during the examination procedures.

I have taken note of the above official notification:*

Dortmund, 26.01.2024

Ort, Datum
(place, date)

Unterschrift
(signature)

***Please be aware that solely the German version of the affidavit ("Eidesstattliche Versicherung") for the Bachelor's/ Master's thesis is the official and legally binding version.**

Abstract

This thesis delves into the dynamic landscape of millimeter-Wave (mmWave) communication technology where the main focus is on conquering the challenges posed by increased path loss at mmWave frequencies, particularly due to obstructions. Moving towards 6G, the resulting shadow regions need to be illuminated to make mmWave networks investments feasible, where metasurface based Smart Radio Environments (SRE)s offer a pivotal solution by deliberately reflecting Electro-Magnetic (EM) waves to enhance performance. Addressing limitations of Intelligent Reflecting Surface (IRS), such as complex deployment logistics and active power requirements, have prompted a shift towards passive reflectors such as Holistic Enlightening of bLackspots with pas-sive reflectOr moduleS (HELIOS). This thesis aims to solve the lack of channel models for HELIOS reflectors by leveraging it as an efficient and scalable alternative, thus, offering a promising solution for future cellular networks. The thesis also highlights the potential advantages of HELIOS reflectors over IRS in terms of peak gain and beamwidth and emphasizes the need for optimizing the performance.

The thesis then proceeds to develop an analytical model for the bistatic Radar Cross Section (RCS) for the HELIOS reflectors and validate it by comparing with EM simulations. The thesis further highlights the main reflection lobes are well-represented, e.g., in regards to gain and beamwidth and also highlights the attained speed-up and the significant reduction in computing time of using the proposed model. Further focusing on implementing the analytical model in an urban scenario to predict the connectivity and improve the initial reflector geometry and position to optimize the mmWave communication. The result shows the better coverage and stronger signals by IRSs than HELIOS reflectors due to its dynamic nature which allows it to focus on each UE position individually. Further investigation reveals that by fixing the node for IRS, an equivalent coverage to that of HELIOS reflectors is achieved, thereby proving its applicability in sophisticated hybrid network planning and HELIOS customization process.

Keywords:

- Metasurface-aided mmWave communications
- Simulation and modeling of HELIOS reflectors
- Channel and reflection modeling

Contents

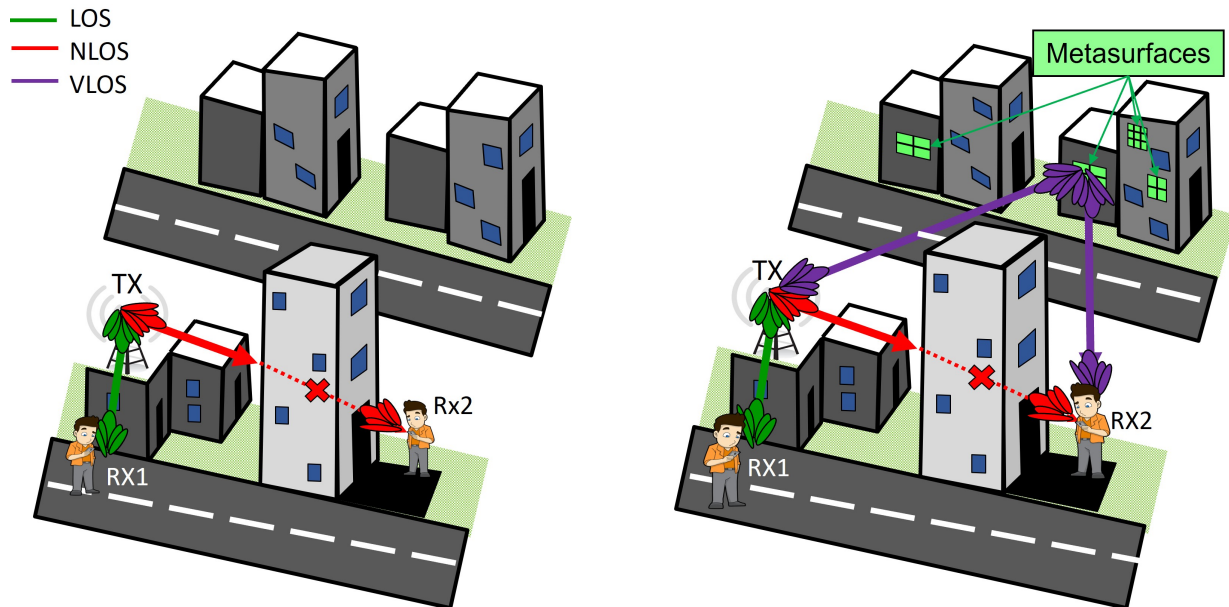
Abstract	V
1 Introduction	1
2 Background	3
2.1 Millimeter Wave Communication	3
2.1.1 Propagation Characteristics	5
2.1.2 Beamforming and Beam Management	5
2.2 Channel Modeling	6
2.2.1 Propagation Environment	7
2.2.2 Free-Space Propagation Model	8
2.2.3 3GPP Channel Model	10
2.3 Metasurfaces	12
2.3.1 Design and Architecture of Intelligent Reflecting Surfaces	14
2.3.2 Passive Reflectors and the HELIOS Concept	14
2.3.3 Common Coordinate System and Parameters for Metasurface Characterization	17
2.3.4 IRS Reflection Gains in Existing Channel Models	27
2.4 Scope of Thesis	29
3 Simulation and Analytical Modeling of HELIOS Reflectors	31
3.1 Methodology	31
3.2 Simulative Analyses of HELIOS Reflector Modules	33
3.2.1 Variation of Slope Angle	33
3.2.2 Effect of Different Reflector Sizes	35
3.2.3 Impact of Reflecting Surface Material	35
3.3 Analytical Modeling of HELIOS Modules	37
3.3.1 Bistatic Radar Cross Section	37
3.3.2 Analytical Model for the Reflection of Planar Surfaces	38
3.3.3 Modeling of HELIOS Module Reflection	39
3.3.4 Assessment of Differences between Simulations and Analytical Model	41
3.4 Analytical Model for Multi-Module HELIOS Reflectors	44
3.4.1 Independent Superposition of Overall Reflection Characteristics	44
3.4.2 Improved Model Using Inter-module Relations	52
3.5 Summary	58
4 Performance Evaluation and Case Study	59
4.1 Computing Time Analysis	59
4.2 Urban Case Study	63
4.2.1 Urban Scenario Implementation	64
4.2.2 Baseline Connectivity Using LOS Channel Models	67
4.2.3 Analyzing Connectivity Enhancement by HELIOS Reflectors	68

4.2.4	Optimizing Connectivity by Improving upon HELIOS Geometry	71
4.2.5	Optimizing Connectivity for Different Reflector Position	74
4.2.6	Analyzing IRS Based Connectivity	75
4.2.7	Comparison of IRS and HELIOS based Connectivity Enhancements	78
4.2.8	Sensitivity Point: HELIOS performance with UMi-Radar Equation	81
4.3	Outlook on Future Arbitrarily-Shaped HELIOS Reflecting Surfaces	85
5	Conclusion	88
5.1	Outlook	89
Abbreviations		90
Bibliography		92

1 Introduction

In the never-ending quest of advancing wireless communication technology, the use of mmWave frequencies has begun with 5G, thus offering future-proof data rates and network capacity due to the large available bandwidth [1–3]. However, path loss at mmWave frequency is much higher, particularly due to reduced object penetration, thus greatly reducing the effective cell and causing shadowing within [4, 5].

Looking toward the future 6G, this shall be addressed by new concepts such as SREs [6]. There, metasurfaces shall be used to improve connectivity, among other things, by using their capability to deliberately modify the reflection behavior of an impinging incident wave. There are two kinds of metasurfaces: IRS and passive reflectors.



(a) mmWave communication in a nutshell with RX1 in LOS has well connectivity, and RX2 in NLOS condition has a poor connection.

(b) Future metasurface-enhanced mmWave networks can provide good connectivity in the NLOS regions by illuminating shadow regions using smart reflection behavior.

Figure 1.1: mmWave communication links from the transmitter (TX) to two differently positioned receivers (RXs): (a) RX1 in Line-of-Sight (LOS) has a good connection, whereas RX2 in Non-Line-of-Sight (NLOS) cannot connect to the network. In (b) we illustrate how a metasurface that is mounted in the vicinity of the transceivers provides Virtual-Line-of-Sight (VLOS) connectivity to the NLOS RX.

IRS is a current hot topic in 6G research, primarily explored for its high flexibility by allowing dynamic control of reflected electromagnetic waves [7–9]. However, there are drawbacks to high energy consumption and active electronic components' complexity associated with IRS. These challenges are not expected for the passive reflectors such as HELIOS [10], making them the primary focus of this work.

In contrast to relying merely on simulations like current work, developing a HELIOS channel model or reflection model becomes critical since it provides a systematic analytical framework based on RCS concepts [11, 12]. While simulation-based methods provide useful insights, an analytical model not only speeds up the computation, but it also enables a more rapid design and evaluation of passive reflector applications in urban communication networks. To demonstrate this practicality, we conduct a detailed analytical case study using HELIOS reflectors and compare them to IRSs.

The remainder of this thesis is structured as follows. Sec. 2 of this master thesis introduces 5G mmWave communication before diving into the 6G metasurface concepts. Particularly, we introduce selected IRS channel models and point out the lack of such for the recently proposed HELIOS reflectors. Sec. 3 derives the analytical model of the bistatic RCS of HELIOS reflectors and compares the arising reflection patterns to EM simulations. Sec. 4 assess the computing times before exploring our model in the context of an urban network scenario. There, we use it to optimize the connectivity and, at last, we directly compare IRS and HELIOS performance. Sec. 5 concludes this work by summarizing the key contributions and a brief outlook on future research.

2 Background

This section contains the technical background for this thesis where we first introduce mmWave specific cellular communications technology aspects in Sec. 2.1. In Sec. 2.2, the focus is on channel modeling, highlighting the differences between LOS and NLOS conditions. Sec. 2.3 provides a comprehensive introduction to the technology concept of metasurfaces that are envisioned to be active components of future sixth-generation (6G) radio access networks, but passive variants may already be employed in conjunction with fifth-generation (5G) networks. We then introduce existing IRS channel models that are taken into consideration for further reinterpretation. Lastly, based on previously presented related works, Sec. 2.4 formulates the aims of this master thesis.

2.1 Millimeter Wave Communication

Globally, the demand for 5G networks is rising quickly. The wireless communication of upcoming generations needs to be improved to meet our constantly increasing demand for faster data speeds and lower latency. Applications such as the Internet of Things (IoT), augmented reality, and driverless vehicles necessitate higher performance networks to function successfully and deliver a smooth user experience [13, 14]. To keep up with these growing requirements and ensure that wireless networks can meet future demands, new technology is required. The much-needed scalable increases in network capacity and peak data rates can be achieved using mmWave communication technology. Due to more hostile propagation characteristics in terms of higher atmospheric absorption and increased susceptibility to obstacles and environmental conditions, the move to directional communications necessitates for compensating the additional path loss. Due to this, cellular mmWave communications will be drastically different from those of the current typically sub-6 GHz networks. These variations make it harder to use mmWave communications to their fullest potential, as discussed in this section.

In typical commercial mobile wireless telecommunication systems, wireless and mobile systems operate in a specific frequency band within the sub-6 GHz spectrum. However, these frequency bands are saturated as a result of the exponential growth in network data traffic in current wireless communication. According to recent studies by [15], the bandwidth currently present in the sub-6 GHz spectrum, which is covered by 5G Frequency Range 1 (FR1), will not be sufficient to achieve the capacity required for the upcoming systems.

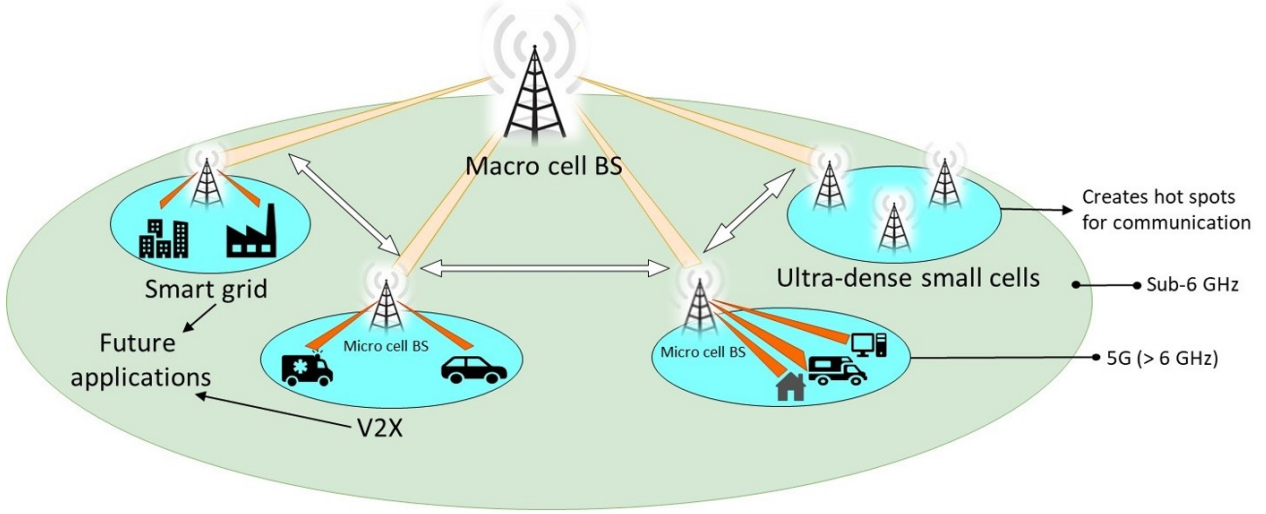


Figure 2.1: Illustration of typical deployment of mmWave communications with use cases and future applications with the communication established between macrocell base stations at sub-6 GHz to the microcell base stations [16, 17].

The mmWave frequency band, which offers greater frequency bandwidths, enters the picture at this point. The Third Generation Partnership Project (3GPP) supports an additional frequency range with 5G, so-called Frequency Range 2 (FR2) that includes seven operational bands between 24.2 GHz and 71 GHz, namely n257, n258, n259, n260, n261, n262, and, n263 [18]. However, not all frequencies are included because, depending on the nation, only the ranges between 24.25-29.5 GHz, 37-43.5 GHz, 47.2-48.2 GHz, and 57-71 GHz shall be used. More frequency ranges have recently been identified for 6G [18], including Frequency Range 4 (FR4) which covers the frequency range of 71 GHz to 114.2 GHz and is anticipated to be used for autonomous and connected vehicles under the umbrella of Intelligent Transportation Systems (ITS). The Frequency Range 5 (FR5) category includes frequencies above 114.2 GHz. Additionally, Frequency Range 3 (FR3) covers the majority of the space between FR1 and FR2, i.e., the "No Man's Land" [19] between 10 GHz to 20 GHz. As a result, with FRs 2–5, it is possible to see how crucial the spectrum above 6 GHz will be for future communication networks.

Fig. 2.1 depicts a typical mmWave communication deployment with several use cases. We see communication linkages formed in both the sub-6 GHz and greater than 6 GHz frequency ranges in this illustration. The deployment also includes ultra-dense tiny cells specifically placed to generate communication hotspots. In terms of future applications, the figure suggests smart grid and V2X (Vehicle-to-Everything) connectivity. These developing application cases demonstrate mmWave technology's adaptability and disruptive promise in enabling not only better mobile broadband but also critical infrastructure and intelligent transportation systems.

The mmWave spectrum is expected to be used by future mobile radio networks to deliver higher data rates for novel use cases like extended Reality (XR). Virtual reality, autonomous vehicles,

swift factory robots, and 8K video streaming are some additional cutting-edge services made possible by mmWave technology.

2.1.1 Propagation Characteristics

The EM waves with a wavelength λ of 1 mm to 10 mm are known as mmWave. Using the formula $f = \frac{c}{\lambda}$, where c is the speed of light ($\approx 3 \cdot 10^8$ m/s), we convert the wavelength to obtain a frequency range of 30 GHz to 300 GHz. mmWave is also referred to as the Extremely High Frequency (EHF) band or the Ultra High Frequency (UHF) band, according to the International Telecommunication Union (ITU) [20]. From an industry perspective, frequencies above 20 GHz, sometimes even from above 10 GHz, are also referred to as mmWave.

So far, we have emphasized the advantages of mmWave technology, namely that it allows for high network capacity that is future-proof and peak user data rates because of the wide available bandwidth. However, there are also drawbacks to using mmWave frequencies. Before the adoption of 5G, frequency bands above 6 GHz were thought to be unsuitable for mobile wireless communications due to their susceptibility to high path losses, especially as a result of obstruction by any objects, including buildings, people, and vegetation [4]. At various frequencies and distances, the path loss calculations show how frequency affects wireless communication. The path loss is roughly 92.4 dB at a frequency of 2 GHz and a distance of 100 m. In contrast, the path loss dramatically rises to almost 108.5 dB at a higher frequency of 28 GHz. This represents a large difference of roughly 16.1 dB. When comparing a concrete wall to a similar wall at lower frequencies, the penetration loss at 28 GHz through the wall may be much larger, up to about 30 dB. Furthermore, compared to absorption losses at lower frequencies, the human body is predicted to experience a greater path loss at 28 GHz, possibly approaching 20 dB.

Environmental factors include increased atmospheric absorption, a greater impact by rain and snow, increased penetration losses, and, increased diffuse scattering due to surface roughness becoming relatively large compared to the wavelength [4]. While these obstacles restrict the use of mmWave, improved antenna technology has been suggested to make up for the extra losses with the idea of grouping numerous, now smaller, antennas into arrays that are then used for beamforming.

2.1.2 Beamforming and Beam Management

As mmWave has short wavelengths and high frequencies, antennas get smaller and can be combined into antenna arrays with a small form factor. Through the use of beamforming and such antenna arrays, the antenna directivity is made possible in a specific direction. This will be used for transmission and reception. There, the impact of significant path loss can be lessened or even mitigated by the beamforming gain. The formed beam can be configured in any way, but the idea

is to direct the resulting antenna beam along the strongest propagation path for maximum efficiency. In addition, the antenna pattern can have some directions nulled to lessen interference from/at other devices. A multi-armed antenna beam may also be realized to serve multiple users, depending on the hardware architecture. When two or more antenna elements are arranged spatially and electrically in arrays that are connected, directional radiation patterns can be created. The feed network, which refers to the connections between the RF front end and the antenna elements, creates a phased array by assigning each element a phase. To improve the received signals, adjustments may even be made to the amplitude of the individual antenna branches [21]. The individual antenna elements' radiation patterns, mounting orientations, and polarizations as well as the geometry of the array all have an impact on how well the array works.

Because wireless communication frequently serves mobile users, the beam directions must be continuously aligned. Beam management processes include beam tracking and beam switching techniques for sustaining the established link. With slight adjustments, the former constantly modifies the Tx and Rx beam orientation. This dynamic alignment is critical for overcoming the hurdles given by mobile users' changing position, and maintaining a stable and high-quality connection. Beam tracking allows the system to monitor the user's location and modify the beam direction in real time to maintain the best possible link. Beam-switching techniques, in addition to beam tracking, play an important part in seamless communication by permitting smooth transitions between available propagation paths and base stations when the user's movement necessitates such handovers [22, 23]. These beam management approaches are critical for delivering the performance and dependability that current wireless communication systems demand.

2.2 Channel Modeling

Channel modeling is an essential part of the design of efficient wireless communication systems. To design a communication system that performs reliably and effectively, we need a process to characterize and optimize its behavior based on its fundamental mathematical representation of the physical channel [24, 25]. Thus, the representation of how transmitted EM waves interact with the environment is one of the core values of channel modeling. The properties such as free-space path loss and interactions with objects in terms of reflection, diffraction, and scattering are modeled [25,26]. Moreover, the antenna patterns of the transmitter and receiver are considered. These are quantifiable, making it possible to predict the channel conditions in particular environments. As we delve further into this subject, we investigate various channel modeling methodologies, approaches, and tools that are used to fully comprehend the mmWave communication environment and its effect on system performance.

A Tx and Rx scenario is succinctly illustrated in Fig. 2.2, which also shows the LOS path to the receiver at Rx1 with gain G_{Rx1} and NLOS path to the receiver at Rx2 with gain G_{Rx2} from the transmitter Tx with gain G_{Tx} . To enhance this illustration, a sample Channel Impulse Response (CIR) is shown on the right, providing a practical understanding of how the channel response could

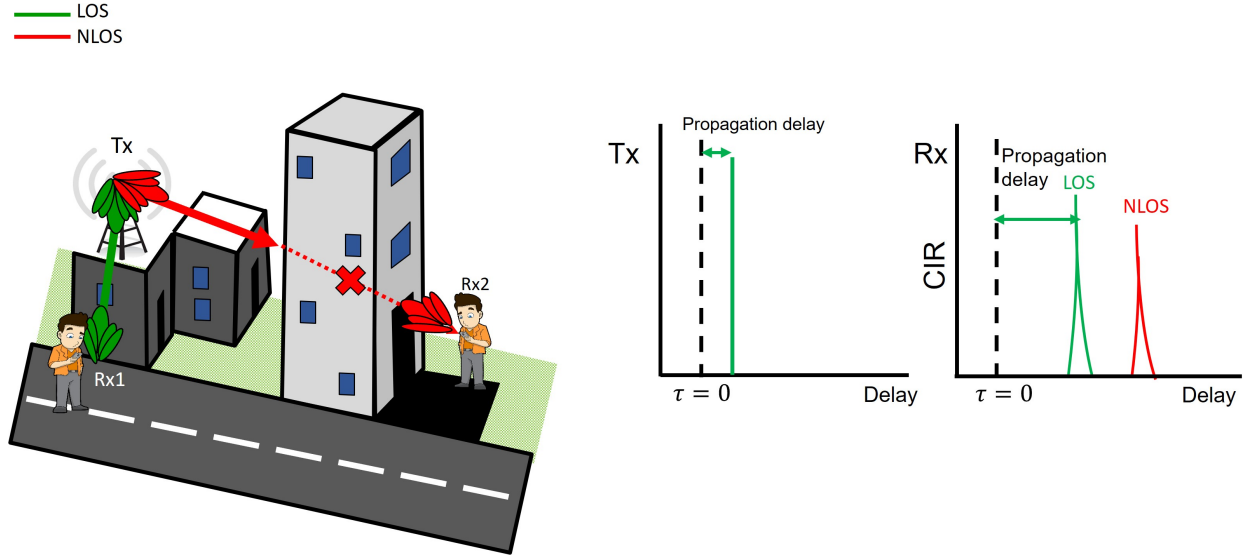


Figure 2.2: Illustration of a simple communication system with the transmitter Tx with gain G_{Tx} in LOS path with Rx1 with gain G_{Rx1} and NLOS path with Rx2 with gain G_{Rx2} . The sample CIR graphs on the right include both the LOS and NLOS paths for the general grasp of the idea [27].

seem for both LOS and NLOS paths with some amount of propagation delay. The time-varying reaction of a communication channel to an impulse signal is represented by the channel impulse reaction, which effectively characterizes the features of the channel [27].

2.2.1 Propagation Environment

Many different channel modeling techniques can be used in this setup for system and network planning [18, 28]. Popular models include WINNER and COST, and as the world transitions to mmWaves, models from the 3GPP, ITU, and IEEE are becoming increasingly important. A brief overview of existing schemes is followed by a detailed introduction of a few channel models [15].

The suitability or applicability of channel models depends on those traits. Others are restricted to 2D propagation, while some cannot be used at mmWaves because they only take into account sub-6 GHz frequencies. The computationally difficult and labor-intensive modeling alternative to any such method is ray-tracing which simulates the propagation of EM waves in a particular environment [25, 29] by following rays from the transmitter to the receiver and accounting for reflections, diffraction, and scattering [30]. Stochastic modeling is a form of statistical modeling, that uses probability distributions to describe the channel properties based on measurements or ray-tracing simulations. With these types of models, whether LOS or NLOS conditions are present is frequently a crucial parameter for path loss prediction.

Tab. 2.1 provides an overview of such available mmWave channel models. A hybrid propagation model that combines the previously described deterministic and stochastic elements serves

Table 2.1: mmWave channel modeling efforts by different organizations with their operating frequencies and the kind of propagation models that they support.

Channel Model	Source	Frequency	Year	Environment	Mobility Support	Propagation Models
5G Channel Model (5GCM)	[28, 32]	28 GHz, 38 GHz, 73 GHz	2011	Indoor, outdoor	Yes	Hybrid
Mobile and wireless communications Enablers for the Twenty-twenty Information Society (METIS)	[28, 33]	up to 100 GHz	2012	Indoor, outdoor	No	Hybrid
Third Generation Partnership Project (3GPP)	[18, 28]	up to 100 GHz	2017	Indoor, outdoor	Yes	Empirical
Millimeter-Wave Evolution for Backhaul and Access (MiWEBA)	[34, 35]	60 GHz	2014	Outdoor	No	Stochastic
QUAsi Deterministic RadIo channel GenerAtor (QuaDRiGa)	[34]	30 GHz	2014	Indoor, outdoor	Yes	Hybrid

as the foundation for the few-channel model. The deterministic component uses ray-tracing to simulate the spread of radio waves by following each individual ray as it interacts with various elements of the environment. To take into account the randomness and variability in the propagation environment, the stochastic component is based on statistical models [31]. Apart from these, 3GPP propagation models are empirical, i.e., they extract characteristics that describe radio wave propagation in various situations from real-world measurement data. Because these models are the result of intensive field testing and measurement, they are useful instruments for forecasting signal behavior and enhancing mobile communication system performance. In the following sections, we consider alternative channel models. The free-space path loss model is first introduced in Sec. 2.2.2 and then followed up by the 3GPP UMi and UMa models in Sec. 2.2.3.

2.2.2 Free-Space Propagation Model

The FSPL model constitutes the fundamental and most simplistic channel model considering a radio signal in free space, i.e., there is LOS between Tx and Rx and no multipath propagation. Eq. (2.1) describes the received power in free-space conditions.

$$P_{Rx} = P_{Tx} \frac{G_{Tx} \cdot G_{Rx} \cdot \lambda^2}{(4 \cdot \pi \cdot r_{Tx,Rx})^2} \quad (2.1)$$

Here P_{Tx} and P_{Rx} are the transmitted and received power in Watts, respectively, $r_{Tx,Rx}$ is the 3D LOS distance between the transmitter and the receiver, G_{Tx} and G_{Rx} are the gains of the transmitter and receiver antennas relative to an isotropic radiator with a unit gain, and λ is the wavelength of the carrier in m [36].

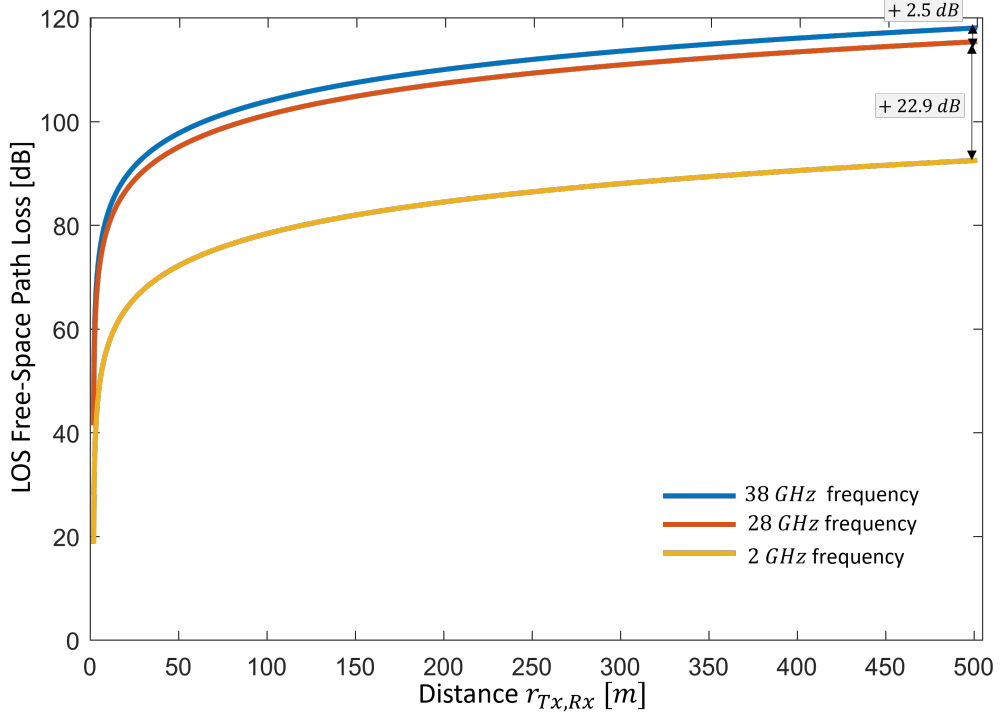


Figure 2.3: Free-space path loss propagation in dB as a function of Tx-Rx distance in m for the LOS condition at 38 GHz, 28 GHz, and 2 GHz frequency. A notable decrease in the path loss is observed as the frequencies decrease.

Accordingly, the power loss between P_{Tx} and P_{Rx} is referred to as propagation path loss PL_{dB} , as depicted in Eq. (2.2). Combining Eq. (2.1) and Eq. (2.2), and moving from linear to decibel presentation, we provide the logarithmic FSPL channel model in the FSPL in Eq. (2.3). Fig. 2.3 depicts the relation between path loss in dB as a function of Tx-Rx distance $r_{Tx,Rx}$ in m.

$$PL_{dB} = 10 \cdot \log_{10} \left(\frac{P_{Tx}}{P_{Rx}} \right) \quad (2.2)$$

$$PL_{dB} = -147.5 \text{ dB} + 20 \cdot \log_{10} \left(\frac{r_{Tx,Rx}}{1000 \text{ m}} \right) + 20 \cdot \log_{10} \left(\frac{f}{1000 \text{ MHz}} \right) + G_{Tx,dB} + G_{Rx,dB} \quad (2.3)$$

For the increase in Tx-Rx distance, the exponential curve depicts the inverse proportionality relation between received power and the path loss. The figure also depicts the variation in path loss curves for different frequencies: 38 GHz, 28 GHz, and 2 GHz, where we observe path loss differs by more than 2.5 dB and 22.9 dB between these three curves. Hence, the antenna gains G_{Tx} , and G_{Rx} must be sufficiently large to compensate for these higher losses.

$$P_{Rx,Radar} = P_{Tx} \cdot \frac{G_{Tx} \cdot G_{Rx} \cdot \lambda^2 \cdot \sigma_{Meta}}{(4 \cdot \pi)^3 \cdot (r_{Tx,Ref})^2 \cdot (r_{Ref,Rx})^2} \quad (2.4)$$

In the case of obstructions, a virtual LOS is established where the combined path loss from Tx to the reflector and from the reflector to Rx is no longer necessary as a different path passes via Tx-reflector-Rx. To address this, we present the notion of radar path loss in Eq. (2.5) in logarithmic

scale, which is developed from radar power received in Eq. (2.4).

$$\begin{aligned} PL_{FSPL_{Radar}} = & -136.5 \text{ dB} + 20 \cdot \log_{10}(r_{Tx,Ref}) + 20 \cdot \log_{10}(r_{Ref,Rx}) + 20 \cdot \log_{10}(f) \\ & - \sigma_{Meta} + G_{Tx,dB} + G_{Rx,dB} \end{aligned} \quad (2.5)$$

Here, σ_{Meta} is the gain at the reflecting metasurface. This method effectively conveys the essence of instances using virtual LOS. The FSPL model implicitly assumes that there are no obstructions that the EM wave can interact with, this is very different from terrestrial communications, where there are obstructions like ground and building reflections as well as obstructions like building, human, or vegetation penetration losses, radar equations can be used. Although the FSPL model is a helpful starting point for understanding signal propagation, it should be noted that it is a simplified representation and thus might not accurately depict real-world scenarios.

2.2.3 3GPP Channel Model

For greater accuracy in terrestrial situations, we employ more sophisticated propagation models or EM simulations such as ray-tracing. In the next section, we introduce key 3GPP channel models and their boundary conditions, giving an illustration of a straightforward model applicable to 5G communication scenarios on Earth. To address the diversity of 5G deployment scenarios in wireless communication systems, the 3GPP has defined several channel models. The Urban Micro (UMi) and Urban Macro (UMa) are two widely used models that capture the characteristics of urban and suburban areas, respectively.

UMi Channel Characterization

The radio propagation characteristics in UMi environments are represented by the 3GPP UMi model, as summarized in Tab. 2.2. It applies to urban areas with a high user density, small cell sizes, and a mix of indoor and outdoor users. To account for the important effects that carrier frequency and antenna heights have on the signal propagation characteristics in urban microcell deployment scenarios, find a channel model description suitable for such scenarios operating at various frequency bands, such as sub-6 GHz and mmWave. Path loss equations for the LOS and NLOS are given by Eq. (2.6) and Eq. (2.9), respectively. This channel model uses shadow fading σ_{SF} of 4 dB for LOS, and 7.82 dB for NLOS conditions. The applicability range for receiver h_{Rx} lies between 1.5 m to 22.5 m and the transmitting antenna height by default is 10 m with an Inter-Site Distance (ISD) of up to 500 m [37]. The applicability frequency ranges for path loss formulas are from $0.5 \text{ GHz} < f < 100 \text{ GHz}$. Tab. 2.2 consists of a break point distance d_{BP} , given by $d_{BP} = 4 \cdot h_{Tx} \cdot h_{Rx} \cdot \frac{f}{c}$, where after the path loss increases additionally as partial obstruction likelihood becomes more likely.

Table 2.2: UMi path loss model for LOS and NLOS conditions with their applicability parameters that can be deemed to be suitable for many scenarios as defined by 3GPP [37].

Modality	Path Loss [dB]	Shadow Fading Standard Deviation [dB]	Condition Parameters
LOS	$PL_{UMi-LOS} = \begin{cases} PL_1 & 10 \text{ m} \leq r_{Tx,Rx} \leq d_{BP} \\ PL_2 & d_{BP} \leq r_{Tx,Rx} \leq 5 \text{ km} \end{cases} \quad (2.6)$ $PL_1 = 32.4 + 21 \cdot \log_{10}(r_{Tx,Rx}) + 20 \cdot \log_{10}(f) \quad (2.7)$ $PL_2 = 32.4 + 40 \cdot \log_{10}(r_{Tx,Rx}) + 20 \cdot \log_{10}(f) - 9.5 \cdot \log_{10}((d_{BP})^2 + (h_{Tx} - h_{Rx})^2) \quad (2.8)$	$\sigma_{SF} = 4$	$1.5 \text{ m} \leq h_{Rx} \leq 22.5 \text{ m}$ $h_{Tx} = 10 \text{ m}$
NLOS	$PL_{UMi-NLOS} = \max(PL_{UMi-LOS}, PL'_{UMi-NLOS}) \quad (2.9)$ $\text{for } 10 \text{ m} \leq r_{Tx,Rx} \leq 5 \text{ km}$ $PL'_{UMi-NLOS} = 22.4 + 35.3 \cdot \log_{10}(r_{Tx,Rx}) + 21.3 \cdot \log_{10}(f) - 0.3(h_{Rx} - 1.5) \quad (2.10)$	$\sigma_{SF} = 7.82$	$1.5 \text{ m} \leq h_{Rx} \leq 22.5 \text{ m}$ $h_{Tx} = 10 \text{ m}$

The UMi channel model characterizes characteristics common in close-range urban microcell scenarios for short distances $r_{Tx,Rx} < 10 \text{ m}$. This setting results in increased path loss, which amplifies the impacts of multipath effects and produces noticeable channel impairments. The model does a good job of portraying the difficulties involved with small-scale urban deployments. However, the UMi model might not be the best option for longer distances, like 5 km. UMi is primarily designed for short-range applications in urban environments, and its accuracy decreases with increasing distance from the cell center. In these cases, as the communication range goes beyond the model's specified design parameters, one might expect an increase in path loss and a commensurate decrease in signal quality.

UMa Channel Characterization

Analog to the UMi channel model, the 3GPP defines the UMa model for urban macrocell deployments with the characteristics presented in Tab. 2.3. Path loss equations for the LOS and NLOS are given by Eq. (2.11) and Eq. (2.14), respectively.

The differences to the previously described model are as follows: the model uses shadow fading of 4 dB for LOS and 6 dB for NLOS conditions. The applicability range for the receiver lies between 1.5 m to 22.5 m and transmitting antenna height by default is 25 m.

UMa is designed with macro cellular scenarios in mind, with a focus on wide coverage across greater areas. There may be relatively little path loss for distances $r_{Tx,Rx} < 10 \text{ m}$ inside the cell service area. Nonetheless, the unique features of the urban macro environment have a significant impact on the channel conditions. However, UMa performs better over longer distances, like five kilometers and has a moderate path loss than UMi since it is designed to mimic the channel conditions found in macrocells, which cover large areas.

Table 2.3: UMa path loss model for LOS and NLOS conditions with their applicability parameters that can be deemed to be suitable for many scenarios as defined by 3GPP [37].

Modality	Path Loss [dB]	Shadow Fading Standard Deviation [dB]	Condition Parameters
LOS	$PL_{UMa-LOS} = \begin{cases} PL_1 & 10 \text{ m} \leq r_{Tx,Rx} \leq d_{BP} \\ PL_2 & d_{BP} \leq r_{Tx,Rx} \leq 5 \text{ km} \end{cases} \quad (2.11)$ $PL_1 = 28 + 22 \cdot \log_{10}(r_{Tx,Rx}) + 20 \cdot \log_{10}(f) \quad (2.12)$ $PL_2 = 28 + 40 \cdot \log_{10}(r_{Tx,Rx}) + 20 \cdot \log_{10}(f) - 9 \cdot \log_{10}((d_{BP})^2 + (h_{Tx} - h_{Rx})^2) \quad (2.13)$	$\sigma_{SF} = 4$	$1.5 \text{ m} \leq h_{Rx} \leq 22.5 \text{ m}$ $h_{Tx} = 25 \text{ m}$
NLOS	$PL_{UMa-NLOS} = \max(PL_{UMa-LOS}, PL'_{UMa-NLOS}) \quad (2.14)$ $\text{for } 10 \text{ m} \leq r_{Tx,Rx} \leq 5 \text{ km}$ $PL'_{UMa-NLOS} = 13.54 + 39.08 \cdot \log_{10}(r_{Tx,Rx}) + 20 \cdot \log_{10}(f) - 0.6(h_{Rx} - 1.5) \quad (2.15)$	$\sigma_{SF} = 6$	$1.5 \text{ m} \leq h_{Rx} \leq 22.5 \text{ m}$ $h_{Tx} = 25 \text{ m}$

2.3 Metasurfaces

The previous sections have underlined the need to improve communication channels in NLOS modality, high distance and frequency to high propagation losses. Here, we focus on the 6G concept of so-called metasurfaces that have the potential to completely transform the telecommunications industry as radio environments become programmable, thus yielding SREs [38]. Metasurfaces are often referred to as Reconfigurable Intelligent Surface (RIS), but for simplicity, we refer to models as IRS. Metasurfaces use cutting-edge materials and design principles to precisely control the reflection behavior of the incident EM wave, therefore allowing for optimized propagation characteristics and enabling better connectivity in terms of coverage size, throughput, etc.

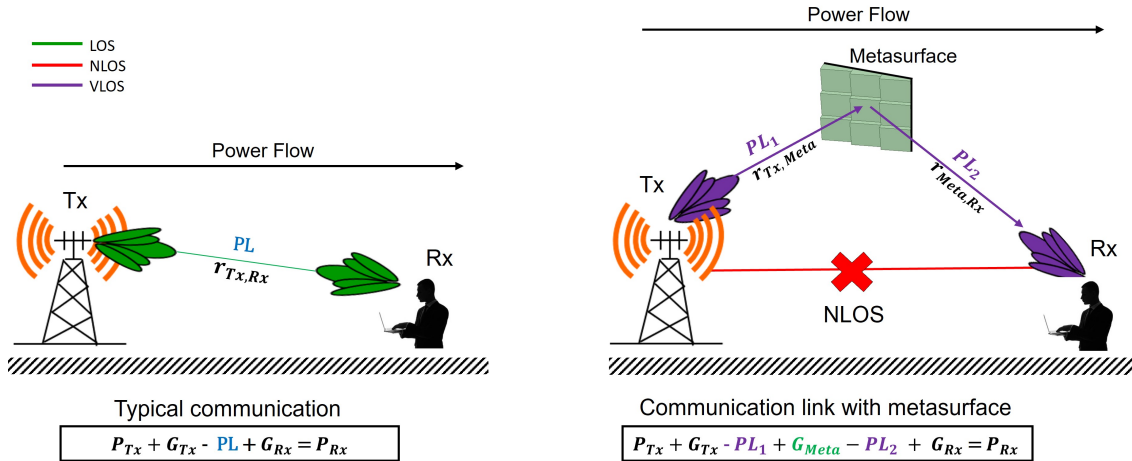


Figure 2.4: Illustration of 6G downlink transmission without (left) and with metasurface (right). In this work, we are particularly interested in deploying IRSs to enable efficient communication in NLOS regimes by using two LOS subchannels.

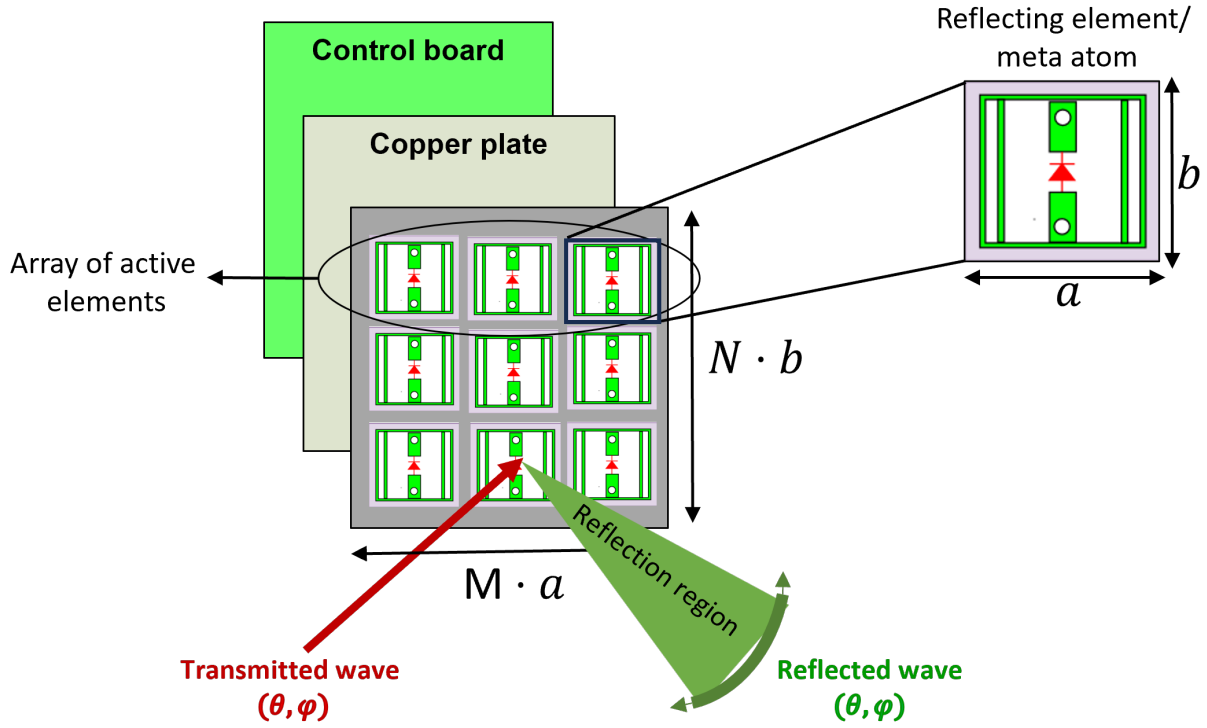


Figure 2.5: Design and architecture of IRS with an array of active elements where the transmitted wave is reflected in a controllable manner in the reflection region for the overall dimensions of $(M \times a) \cdot (N \times b)$.

Fig. 2.4 shows a comparison of the usual communication link without and with metasurface integration. The traditional communication link running from the transmitter to the receiver is depicted on the left side of the figure. The relationship established in this context is defined by classical parameters, i.e., P_{Tx} , P_{Rx} , G_{Tx} , G_{Rx} , and PL between them. On the right of Fig. 2.4, we consider metasurfaces to serve NLOS users. The communication link is established between the transmitter to metasurfaces and, to the receiver. In addition to the classical parameters, we observe two subchannels i.e., Tx-metasurface, and metasurface-Rx, and introduce path losses between them which are given by PL_1 and PL_2 , which is then compensated by the gain at the metasurfaces G_{Meta} .

Fig. 2.5 depicts the structural architecture of an IRS model. They are made up of sub-wavelength unit cells constituting a planar array of $M \times N$ active elements whose dimensions are $a \times b$, respectively. As mentioned previously, they can alter the interaction between the incident wave and the surface. We will examine two crucial of many feasible crucial metasurface features in more detail in the next sections. First, we consider IRSs in Sec. 2.3.1, which may actively direct the reflection into the target direction with the reflection pattern being configured in real-time as desired, focusing on flexibility and adaptability to enhance the coverage and signal strength. Second, we discuss passive reflectors in Sec. 2.3.2, which are entirely passive in nature, i.e., not reconfigurable, but still provide a customized reflection pattern with zero power consumption.

2.3.1 Design and Architecture of Intelligent Reflecting Surfaces

IRSs contain a variety of tiny, reconfigurable reflecting components, enabling precise shaping of the arising reflection pattern by modifying the phase and amplitude of the reflected waves. When compared to reflect-arrays, IRSs are instead placed in the far-field regions of Tx and Rx, i.e., at practical positions such as building facades [39].

The functionality of the IRS depends heavily on its design and architecture which are created to be flexible, and scalable for a variety of wireless applications as shown in Fig. 2.5. An IRS typically consists of a planar array of unit cells whose dimensions are $a \times b$. These may modify the characteristics of electromagnetic waves' phase, amplitude, and polarization [9]. The performance metrics depend on, e.g., the spacing density and number of control bits of the unit cells. These parameters, but also the IRS material affect the supported carrier frequency and bandwidth. Most important, however, is the setting of each unit cell, e.g., in terms of phase as the superposition of the individual unit cells' interactions with the incident EM wave yields the overall IRS performance. Determination of these settings is the main design factor for real-time operation [7–9].

6G use cases for IRSs are, for example, as follows: To increase signal strength and coverage inside a building, for instance, one to several IRSs can be mounted on available wall sections or the ceiling [7]. This way, fewer antenna sites are required such that costs and power consumption are reduced. An IRS can also be used to lessen interference to further enhance the quality of wireless communications. Other usage concepts envision improved security and privacy for wireless communications by, in essence, building a physical barrier that prevents signals from being intercepted or eavesdropped.

Considering the active elements, IRSs need a power line or battery for continuous operation. Additionally, the IRS needs to be controlled by the network operator via a wired link or a wireless connection to the Tx. As an IRS numerous unit cells can form reflection beams similar to an antenna array forming pencil or sector beams, these configurations shall be provided by the network operator along the control link [40]. For this purpose, however, novel signaling procedures similar to the beam management described in Sec. 2.1 is required for 6G.

2.3.2 Passive Reflectors and the HELIOS Concept

However, there are some real-world difficulties with the IRS, such as the need to deal with the complexity of hardware implementation, scalability, and rising energy consumption with size. While IRS represents an evolution for future 6G communications in wireless communication, passive reflectors present a scalable, non-reconfigurable alternative feasible in the short term. In contrast to active IRSs, passive reflectors may not amplify signals but either bundle or scatter the incident energy into a predetermined and fixed direction. Passive reflectors can be created like the meta-surfaces outlined in Sec. 2.3.1 [41, 42], but without the use of adjustable unit cells. Alternative techniques, such as HELIOS [10], are also conceivable as explained below.

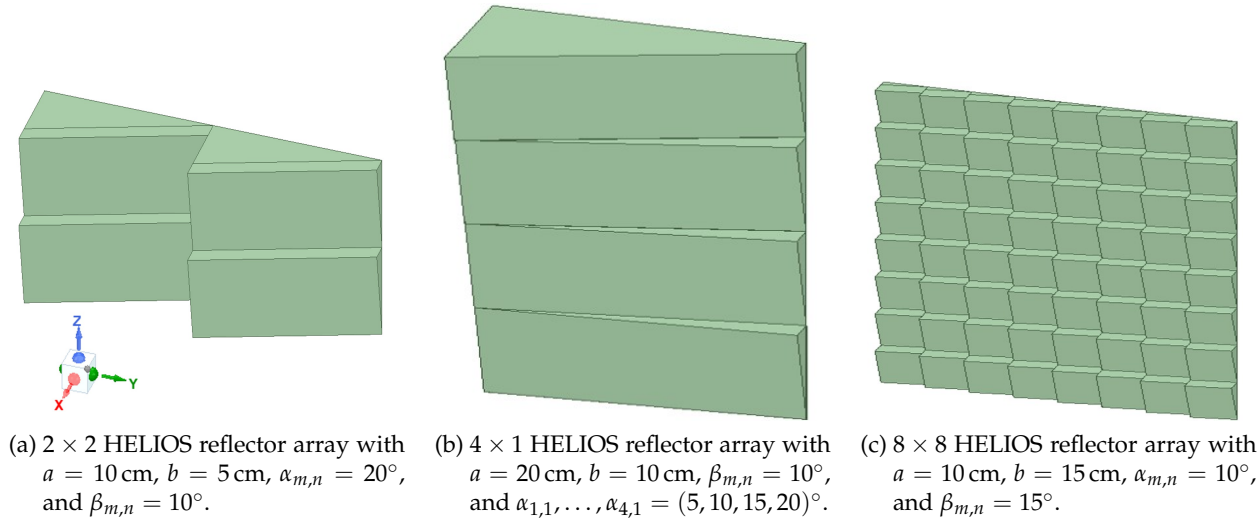


Figure 2.6: Illustration of HELIOS reflector arrays with different dimensions, sizes, and slope angles, showcasing the high degree of flexibility of the model.

Introduction of HELIOS Concept

In light of the previously discussed drawbacks of IRSs, passive reflectors have some advantages over IRS in certain situations. The majority of passive reflectors possess typically fixed structures made up of strategically placed metallic surfaces or objects [43, 44]. Their position and geometry can be deliberately exploited to realize the desired reflection behavior as needed to optimize the communication performance. Naturally, their fixed position and shape make them compatible with existing wireless communication systems as there is no need for novel control links and signaling procedures, while also removing the need for a power supply. Thus, the advantage comes in the simplicity which is expected to also reduce costs. Moreover, passive reflectors are expected to be very dependable for tough outdoor settings coming with challenges regarding temperature (hot and cold), moisture, UV radiation, and wind.

Passive reflectors, in this work represented by the HELIOS [10] concept, come with the above-described features and may quickly revolutionize the wireless network infrastructure landscape. The core approach is as follows:

- Seamless, piecewise installation that easily merges into urban settings without imposing any power supply demands.
- Sleek design and manufacturing method not only meets network operators' rigorous criteria but also improves network coverage capabilities.
- The combination of passive reflectors with cutting-edge processes such as 3D printing and precise spray painting opens up new options for customization and adaptability.

We will now delve into the authors' design and production process for their HELIOS reflectors. The first step constitutes the careful selection of a suitable geometry, i.e., one with the capacity

to successfully reflect the incident electromagnetic wave into the desired direction range. Another critical component of the geometry design is its unobtrusiveness, i.e., minimization of the exhibited protrusion for better technology acceptance [10]. Following that, the authors choose suitable materials and production processes depending on the deployment scenario under aspects of durability, resource efficiency, and costs.

The HELIOS reflector array's adaptation to various configurations, which display a range of dimensions, reflector sizes, and slope angles, is a testament to its versatility as illustrated in Fig. 2.6. The versions that are shown have different values, which highlights the amazing adaptability that the design offers. Because of its adaptation to many settings, this variability highlights the model's versatility and enables customization depending on unique requirements, making it a highly flexible model.

Construction of Geometry of HELIOS Reflector Module

The primary principle controlling the geometry selection of the reflector is the application of Snell's law of reflection [45]. When dealing with a flat reflecting plate with dimensions $a \times b$, our method involves an incident wave meeting the surface at azimuth and elevation angles, with the reflected wave preserving identical angles relative to the surface normal, cf. Fig. 2.7(a). As we move into the domain of three-dimensional passive reflectors, the problem becomes custom-tailoring these structures to precisely focus the transmitted beam towards the specified receiver direction, by the criteria of our network planning.

To accomplish this, the authors designed a saw-tooth-like structure for the reflector, with the depth of each protrusion decreasing proportionally as the number of modules grows [10]. Fig. 2.7(b), and Fig. 2.7(c) illustrate the impact of an individual module's horizontal tilt angle α on the azimuth reflection angle φ_{Rx} and, in addition, the joint case in which a vertical slope angle β further affects the elevation reflection angle θ_{Rx} . It is worth mentioning that the parametrization of the reflector

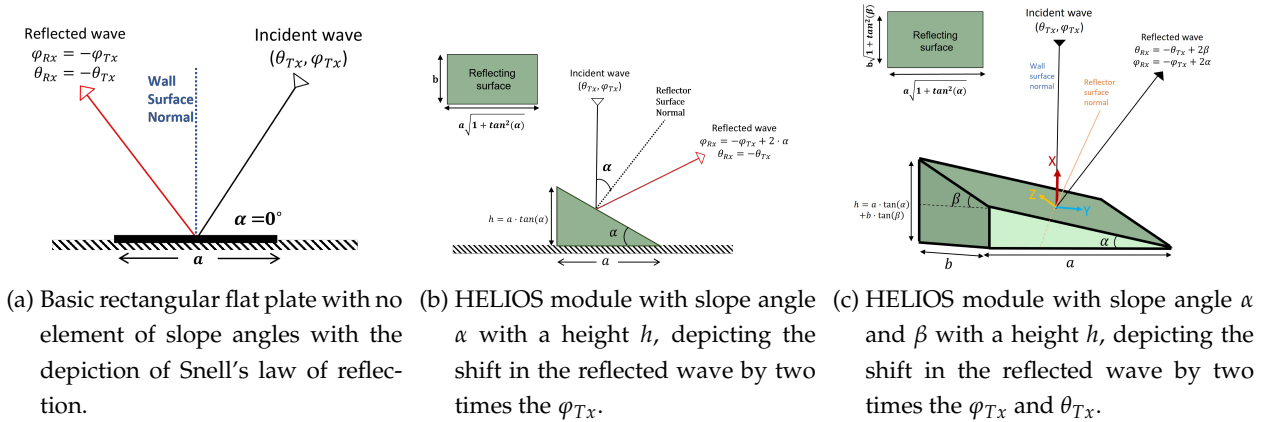


Figure 2.7: Horizontal and vertical tilting of the reflecting surface enables deliberate steering of the reflection towards the desired direction.

module, which includes variables such as vertical and horizontal slope angles namely $\alpha_{m,n}$ and $\beta_{m,n}$, reflector element base size $a \times b$, and indices $m \in 1, \dots, M$ and $n \in 1, \dots, N$ with $M \times N$ specifying the number of HELIOS modules.

Material Selection

Reflectors are often made of highly conductive materials to minimize signal loss. While traditional options such as solid metal reflectors or aluminum foil are effective, they come with high material prices [10]. Moreover, reshaping supplies of metal into the desired HELIOS form may complicate production, and thus, increase costs. The HELIOS concept addresses these issues as follows. Using 3D printing with a suitable filament, e.g., PLA for indoor deployments, arbitrary shapes may be produced. Afterward, a conductive coating is given via spray-coating.

2.3.3 Common Coordinate System and Parameters for Metasurface Characterization

The investigation of metasurfaces for mmWave communication leverages the subsequently described cartesian reference coordinate system, as illustrated in Fig. 2.8. A 3D space defined by the three perpendicular axes (x , y , and z) in this coordinate system, which enables us to precisely find and describe the position and orientation of components in wireless communication systems. For example, the reflecting surface shall be in the y - z -plane.

Let us consider a planar EM wave impinging on the reflecting surface. The direction of this wave is indicated by its wave vector \vec{k} which can be related to the direction of the normal vector \vec{n} of the surface ¹. As depicted by Eq. (2.16) vectors \vec{k} and \vec{n} can be described relative to the reflecting surface using spherical coordinates, namely azimuth angle $\varphi_k \in [-180 : 180]^\circ$ (defined in y - z -plane from y -axis in the direction of z -axis) and elevation angle $\theta_k \in [-90 : 90]^\circ$ (defined in y - z -plane towards x -axis), as well as the magnitudes $n=1$ and $k = \frac{2\pi}{\lambda}$.

$$\begin{aligned}\vec{k} &= (k, \theta_k, \varphi_k) \\ \vec{n} &= [1, 0, 0]\end{aligned}\tag{2.16}$$

Using the described parameters, we describe vector \vec{k} in Cartesian coordinates as follows:

$$\vec{k} = \begin{bmatrix} k_x \\ k_y \\ k_z \end{bmatrix} = k \begin{bmatrix} \cos(\theta_k) \cdot \cos(\varphi_k) \\ \cos(\theta_k) \cdot \sin(\varphi_k) \\ \sin(\theta_k) \end{bmatrix}\tag{2.17}$$

¹Note that vector n has a positive z -component, otherwise, the vector would point into the building or ceiling at which the reflector is mounted.

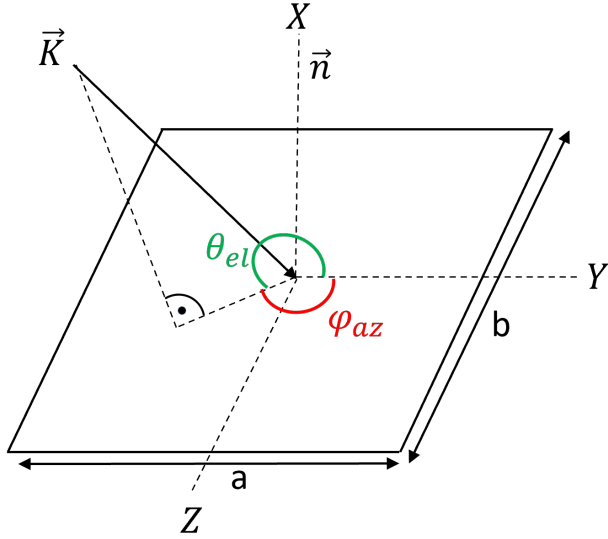


Figure 2.8: Plane wave impinges along direction \vec{k} on reflecting surface in y - z -plane with elevation angle θ_{el} and azimuth angle φ_{az} in deg.

Furthermore, we may deduce the spherical coordinate system parameters from the Cartesian description as follows:

$$\begin{aligned}\theta_k &= \arccos \frac{k_z}{|\vec{k}|} \\ \varphi_k &= \arctan \frac{k_y}{k_x}\end{aligned}\quad (2.18)$$

where $|\vec{k}|$ is the magnitude of impinging wave vector \vec{k} .

$$|\vec{k}| = k = \sqrt{k_x^2 + k_y^2 + k_z^2} \quad (2.19)$$

In the following, we will refer to the incident wave vector using \vec{K}_{Tx} , whereas the reflected wave uses \vec{K}_{Rx} . Based on the law of reflection, the angle of the incident is implicitly defined by the reflection angle, given by Eq. (2.20). So, the elevation and azimuth angles of the impinging and reflecting waves will have the same magnitude but different signs.

$$\begin{aligned}\theta_{Rx} &= -\theta_{Tx} \\ \varphi_{Rx} &= -\varphi_{Tx}\end{aligned}\quad (2.20)$$

Let us consider the Euclidean norm angles to be γ_{Tx} and γ_{Rx} at the transmitter and the receiver, respectively. As defined in Eq. (2.21), they define the overall deviation angle from the x -axis.

$$\begin{aligned}\gamma_{Tx} &= \sqrt{\theta_{Tx}^2 + \varphi_{Tx}^2} \\ \gamma_{Rx} &= \sqrt{\theta_{Rx}^2 + \varphi_{Rx}^2}\end{aligned}\quad (2.21)$$

In the following sections, the previous metasurface geometry relations will be applied. Tab. 2.4 extends these with additional parameters incorporating the above geometry into a wide communication system description including the Tx and Rx.

Table 2.4: Comprehensive standardization of parameters: Units and abbreviations for metasurface channel modeling across the entire thesis.

Abbreviation	Definition	Units
η	Characteristic impedance	Ω
f	Frequency	Hz
c	Speed of light	m/s
Γ	Reflection coefficient	Unitless
k	Wave number	m^{-1}
λ	Wavelength	m
a	y -axis dimension of the IRS	m
b	z -axis dimension of the IRS	m
M	Reflector array on the z -axis of the IRS	Unitless
N	Reflector array on the y -axis of the IRS	Unitless
A_{eff}	Effective aperture of the IRS	m^2
$E_{incident}$	Electric field strength of the incident signal	V/m
$E_{reflect}$	Electric field strength of the reflected signal	V/m
$P_{incident}$	Power of incident signal	W
$P_{captured}$	Power captured by IRS element	W
$P_{reflected}$	Power reflected by IRS element	W
P_{Rx}	Power received by the receiver	W
P_{Tx}	Transmit power	W
G_{Tx}	Gain of transmit antenna	Unitless
G_{Rx}	Gain of receiver antenna	Unitless
G_{IRS}	Gain of IRS	Unitless
$r_{Tx,Rx}$	Distance from transmitter to receiver	m
$r_{Tx,IRS}$	Distance from transmitter to IRS element	m
$r_{IRS,Rx}$	Distance from receiver to IRS element	m
θ_{Tx}	Elevation angle to the transmitter	deg
φ_{Tx}	Azimuth angle to the transmitter	deg
θ_{Rx}	Elevation angle to the receiver	deg
φ_{Rx}	Azimuth angle to the receiver	deg
θ_{dev}	Deviated elevation angle at the receiver	deg
φ_{dev}	Deviated azimuth angle at the receiver	deg
Φ_{IRS}	Phase shift by IRS unit cell	deg
γ_{Tx}	Overall IRS angle of incidence	deg
γ_{Rx}	Overall IRS angle of reflection	deg
PL	Path loss	Unitless
SNR	Signal-to-Noise ratio	Unitless
α	Elevation slope angle	deg
β	Azimuth slope angle	deg
$Gain_{RCS}$	Analytical gain at the reflector	dB
$Gain_{Sim}$	Simulated gain at the reflector	dB

Now that we have a firm grasp of the coordinate system and the variables that will direct our study, we introduce three IRS channel models from the literature and examine each individually.

Model by Özdogan *et al.* (2020) [46]

For an IRS that is set up to reflect an incoming wave from a far-field source in a beamforming like manner towards a far-field receiver in direction θ_{Rx} , the authors in [46] have used the physical optics approach to derive an end-to-end path loss expression. The model consists of a plate in the x - y -plane with dimensions $a \times b$ which is perfectly conducting. It is radiated upon with a linearly polarized EM wave at distance $r_{Tx,IRS}$ at angle θ_{Tx} between incident wave vector and \vec{e}_z , with $\theta_{Tx} \in [0, \frac{\pi}{2}]$. The whole setup can be seen in Fig. 2.9. In the following we briefly summarize the key results of the work in the form of two lemmas yielding equations that will be used in the scope of this thesis.

Due to its far-field nature, the impinging wave vector is a nearly plane wave and the distribution of the EM fields for the incident plane wave is given by Eq. (2.22) where η is the characteristic impedance of the medium.

$$\begin{aligned}\vec{E}_{incident} &= E_{incident} \cdot e^{-j \cdot k(\sin \theta_{Tx} \cdot y - \cos \theta_{Tx} \cdot z)} \vec{e}_x \\ \vec{H}_{incident} &= -\frac{E_{incident}}{\eta} (\cos \theta_{Tx} \cdot \vec{e}_y + \sin \theta_{Tx} \cdot \vec{e}_z) \cdot e^{-j \cdot k(\sin \theta_{Tx} \cdot y - \cos \theta_{Tx} \cdot z)}\end{aligned}\quad (2.22)$$

The E-field will cause the plate's electrons to move and it'll only be in the \vec{e}_x direction as they are orthogonal. A scattered wave is created as a result of the EM radiation that the moving electrons produce.

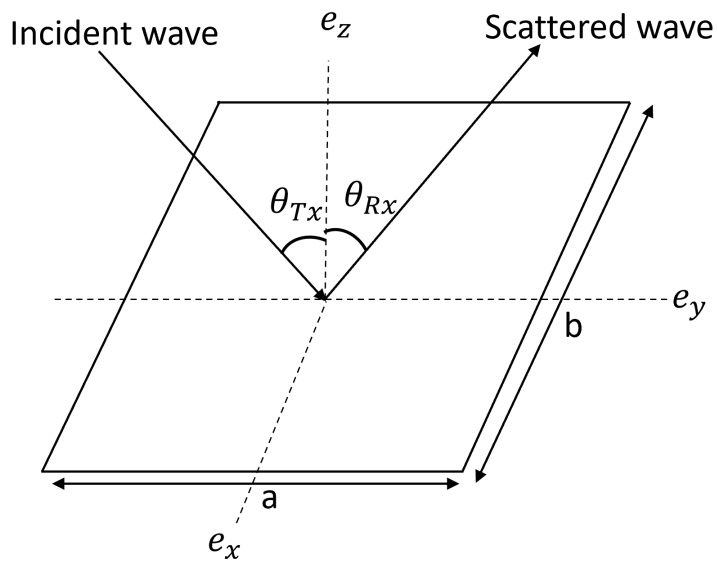


Figure 2.9: Illustrating the setup of the IRS model with the 3D angles for the transmitted and reflected wave [46].

Lemma 1: Measured against \vec{e}_z , the squared magnitude of the scattered field in the \vec{e}_y, \vec{e}_z plane, and at any observation angle $\theta_{Dev} \in [0, \frac{\pi}{2}]$ is given by Eq. (2.23).

$$S(r_{IRS,Rx}, \theta_{Dev}) = \left(\frac{a \cdot b}{\lambda} \right)^2 \frac{E_{incident}^2}{r_{IRS,Rx}^2} \cos^2 \theta_{Tx} \left[\text{sinc} \left(\frac{\pi \cdot b}{\lambda} (\sin \theta_{Dev} - \sin \theta_{Tx}) \right) \right]^2 \quad (2.23)$$

at a far-field observation distance $r_{IRS,Rx} \geq \frac{2 \cdot \max(a^2, b^2)}{\lambda}$ [46].

Eq. (2.23) has several intuitive properties. For instance, the reflected power is proportional to the squared IRS surface area, i.e., $(a \cdot b)^2$. According to Snell's law, the maximum is attained if the argument of sinc = 0°. For $\theta_{Dev} = \theta_{Tx} = 0^\circ$ the reflection power is maximized, i.e., an IRS will be most beneficial the more the incident and reflected waves are perpendicular to the surface.

The angles θ_{Tx} and θ_{Dev} from earlier represent the ideal case, but the main goal of IRS is to achieve total anomalous reflection, with its main beam pointing in the desired direction θ_{Rx} . In order to obtain the ideal field distributions $\vec{E}_{reflect}$ and $\vec{H}_{reflect}$ of the reflected or scattered wave, the surface must be created to divert the incident plane wave as given by Eq. (2.24).

$$\begin{aligned} \vec{E}_{reflect} &= E_{reflect} e^{-j \cdot k(\sin \theta_{Rx} \cdot y - \cos \theta_{Rx} \cdot z)} \vec{e}_x \\ \vec{H}_{reflect} &= -\frac{E_{reflect}}{\eta} (\cos \theta_{Rx} \cdot \vec{e}_z + \sin \theta_{Rx} \cdot \vec{e}_z') e^{-j \cdot k(\sin \theta_{Rx} \cdot y - \cos \theta_{Rx} \cdot z)} \end{aligned} \quad (2.24)$$

Lemma 2: The squared magnitude of the scattered field in Eq. (2.25) at an arbitrary observation angle $\theta_{Dev} \in [-\frac{\pi}{2}, \frac{\pi}{2}]$ is when using an IRS to reflect a signal in the desired direction θ_{Rx} .

$$S(r_{IRS,Rx}, \theta_{Dev}, E_{incident}) = \left(\frac{a \cdot b}{\lambda} \right)^2 \frac{E_{incident}^2 \cdot \cos^2(\theta_{Tx})}{r_{IRS,Rx}^2} \left[\text{sinc} \left(\frac{\pi \cdot b}{\lambda} (\sin \theta_{Dev} - \sin \theta_{Rx}) \right) \right]^2 \quad (2.25)$$

The maximum of Eq. (2.25) is achieved when $\theta_{Rx} = \theta_{Dev}$, thus confirming that the IRS's reflection is maximized in the desired direction although power is also radiated with varying intensity into other directions. Therefore, this equation includes an important description of the IRS reflection pattern. Notably, it generalizes the hull curve described in Eq. (2.23). With transmitter gain G_{Tx} and receiver gain G_{Rx} , Eq. (2.26) gives the relationship between $E_{incident}$ and transmit power P_{Tx} .

$$\frac{E_{incident}^2}{2\eta} = \frac{P_{Tx} \cdot G_{Tx}}{4 \cdot \pi \cdot r_{Tx,IRS}^2} \quad (2.26)$$

The effective area A_{eff} of the receiver antenna, also known as the aperture, can be described as follows:

$$A_{eff} = \frac{\lambda^2}{4 \cdot \pi} G_{Rx} \quad (2.27)$$

Coupling Eq. (2.25), Eq. (2.26), and Eq. (2.27), yields Eq. (2.28), and Eq. (2.29) as the description of the received power of the IRS-based propagation path.

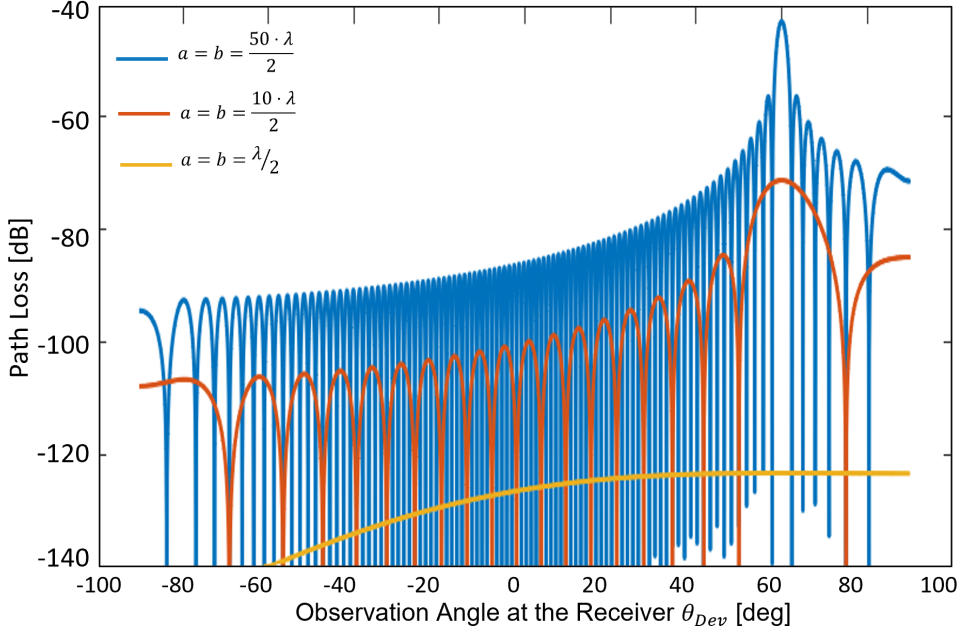


Figure 2.10: Investigation of path loss at 3 GHz for three different IRS sizes when $\theta_{Rx} = 60^\circ$. One can observe that, the larger the reflector size the better it can compensate for path loss and also realize a more narrow reflection.

$$P_{Rx}(P_{incident}, r_{Tx,IRS}, r_{IRS,Rx}, \theta_{Dev}) = \frac{1}{2 \cdot \eta} S \left(r_{IRS,Rx}, \theta_{Dev}, \frac{P_{Tx} \cdot G_{Tx} \cdot \eta}{2 \cdot \pi \cdot r_{Tx,IRS}^2} \right) A_{eff} \quad (2.28)$$

$$\begin{aligned} PL(r_{Tx,IRS}, r_{IRS,Rx}, \theta_{Rx}) &= \frac{P_{Rx}(P_{incident}, r_{Tx,IRS}, r_{IRS,Rx}, \theta_{Dev})}{P_{incident}} \\ &= \left[\frac{G_{Tx} \cdot G_{Rx}}{(4 \cdot \pi)^2} \left(\frac{a \cdot b}{r_{Tx,IRS} \cdot r_{IRS,Rx}} \right)^2 \cos^2(\theta_{Tx}) \left[\text{sinc} \left(\frac{\pi \cdot b}{\lambda} (\sin \theta_{Dev} - \sin \theta_{Rx}) \right) \right]^2 \right] \end{aligned} \quad (2.29)$$

In the ideal case when $\theta_{Rx} = \theta_{des}$, the path loss simplifies to Eq. (2.30).

$$PL(r_{Tx,IRS}, r_{IRS,Rx}, \theta_{Rx}) = \frac{G_{Tx} \cdot G_{Rx}}{(4 \cdot \pi)^2} \left(\frac{a \cdot b}{r_{Tx,IRS} \cdot r_{IRS,Rx}} \right)^2 \cos^2(\theta_{Tx}) \quad (2.30)$$

We observe that the path loss Eq. (2.30) mainly depends on the IRS's overall effective area as seen from the transmitter, i.e., $a \cdot b \cdot \cos(\theta_{Tx})$. Analog to [46], Fig. 2.10 illustrates Eq. (2.29)'s reconstructed model's path loss behavior. This investigation is carried out at the stated frequency of 3 GHz and analyzes the impact of varied sizes of the IRS on path loss. The findings are shown as a function of the density parameter λ and the observation angle θ_{Dev} , while keeping the intended angle constant $\theta_{Rx} = 60^\circ$. The graph shows that the path loss is greatest when the observation angle θ_{Dev} matches the intended angle θ_{Rx} . Furthermore, as the surface area of the IRS rises, the main beamwidth narrows, resulting in greater signal strength gains.

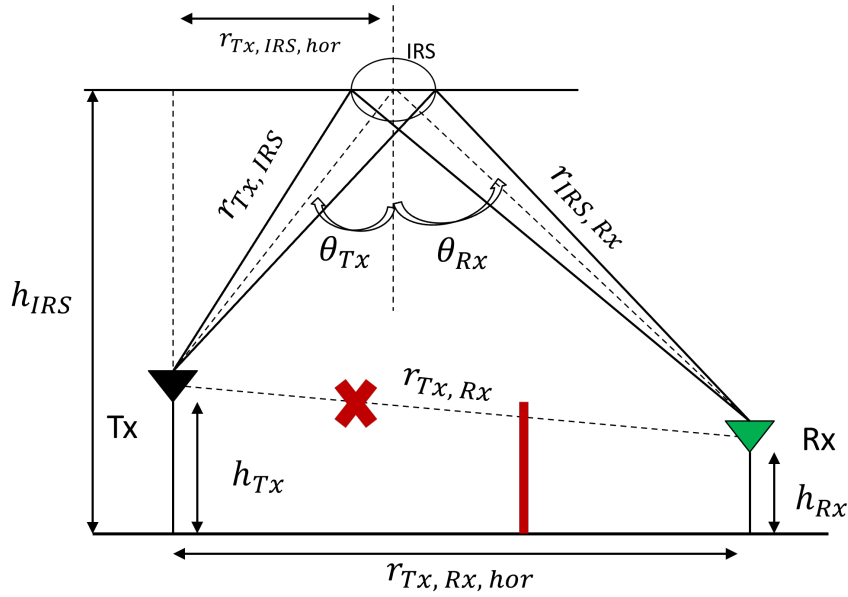


Figure 2.11: Considered setup of the IRS model with NLOS conditions between the transceivers and an IRS-based virtual LOS connectivity [47].

Model by Ntontin et al. (2021) [47]

We now focus on the second model put forth in [47]. There, the authors derive an expression for the end-to-end SNR along an IRS-based channel assuming blocked LOS conditions. Similar to the previously described model, the authors assume free-space path loss conditions between IRS and the two street-level transceivers with both having their antennas focused on the IRS with dimensions much larger than the wavelength and being mounted at high altitudes.

The authors denote the distance between the transmitter and the n -th element of the illuminated IRS by $r_{Tx, IRS, n}$. The incident plane EM wave and the incident electric wave's spatial power density on the IRS n -th element are given by Eq. (2.31), and Eq. (2.32). The setup of the model is explained in Fig. 2.11.

$$\vec{E}_{incident} = E_{incident} \cdot e^{-j\frac{2\pi}{\lambda}r_{Tx, IRS, n}} \vec{e}_x \quad (2.31)$$

Given the incident EM field described in Eq. (2.31), Eq. (2.32) follows as already seen before in model 1 with

$$\frac{E_{incident}^2}{2 \cdot \eta} = \frac{P_{Tx} \cdot G_{Tx}}{4 \cdot \pi \cdot r_{Tx, IRS, n}^2}, \quad (2.32)$$

where η is the free-space impedance. Accordingly, and analog to prior considerations in [46], Eq. (2.33) gives the power captured by the n -th element of the IRS.

$$\begin{aligned} P_{captured} &= \frac{E_{incident}^2}{2\eta} A_{eff} \\ &= \left(\frac{\lambda}{4 \cdot \pi} \right)^2 \frac{P_{Tx} \cdot G_{Tx} \cdot G(\theta_{Tx})}{r_{Tx, IRS, n}^2} \end{aligned} \quad (2.33)$$

with

$$A_{eff} = \frac{\lambda^2}{4 \cdot \pi} G(\theta_{Tx}), \quad (2.34)$$

where A_{eff} is the effective aperture of the n -th IRS element with $G(\theta_{Tx})$ being its gain. Using Snell's reflection law, the transmit and receive gains of the IRS can be written as follows.

$$G(\theta_{Tx/Rx}) = \frac{4 \cdot \pi}{\lambda^2} \cdot a \cdot b \cdot \cos(\theta_{Tx/Rx}), \quad (2.35)$$

where a and b are the size of the reflecting surface in the x and y -axis direction, respectively. The spatial power density at the receiver antenna following reflection from the n -th element is given by Eq. (2.36), where Γ is the reflection coefficient.

$$P_{spatial} = P_{captured} \cdot \frac{\Gamma^2 \cdot G(\theta_{Rx})}{4 \cdot \pi \cdot r_{IRS,Rx,n}^2}, \quad (2.36)$$

where $r_{IRS,Rx,n}$ is the distance between the center of the n -th IRS element to the receiver antenna. Using the above equations, the electric field of the impinging wave at the RX is summarized below. We note that $\phi_{IRS,n}$, describes the IRS unit cell's phase shift.

$$\vec{\mathbf{E}}_{reflect} = \sqrt{(2 \cdot \eta \cdot P_{spatial})} \cdot e^{-j\left(\phi_{IRS,n} + \frac{2 \cdot \pi \cdot (r_{Tx,IRS,n} + r_{IRS,Rx,n})}{\lambda}\right)} \vec{e}_x \quad (2.37)$$

Last,

$$P_{Rx} = \left(\frac{\lambda}{4 \cdot \pi} \right)^4 \frac{P_{Tx} \cdot \Gamma^2 \cdot G_{Tx} \cdot G_{Rx}}{r_{Tx,IRS,n}^2 \cdot r_{IRS,Rx,n}^2} \cdot \left| \sum_{n=1}^{M \cdot N} \sqrt{G(\theta_{Tx}) \cdot G(\theta_{Rx})} \times e^{-j\left(\phi_{IRS,n} + \frac{2 \cdot \pi \cdot (r_{Tx,IRS,n} + r_{IRS,Rx,n})}{\lambda}\right)} \right|^2 \quad (2.38)$$

where M and N are the numbers of IRS elements in the x and y axis, respectively. The received power is maximum when

$$\phi_{IRS,n} = -\frac{2 \cdot \pi \cdot (r_{Tx,IRS,n} + r_{IRS,Rx,n})}{\lambda} \forall n \in 1, \dots, M \cdot N. \quad (2.39)$$

The maximum power received is expressed as Eq. (2.40).

$$P_{Rx,max} \approx \frac{P_{Tx} \cdot M^2 \cdot N^2 \cdot a^2 \cdot b^2 \cdot \Gamma^2 \cdot G_{Tx} \cdot G_{Rx} \cdot \cos(\theta_{Tx}) \cdot \cos(\theta_{Rx})}{(4 \cdot \pi)^2 \cdot (r_{Tx,IRS,n} \cdot r_{IRS,Rx,n})^2} \quad (2.40)$$

Using the maximum received power and the noise power in Eq. Eq. (2.42), the author in [47] conclude their work with the maximum end-to-end SNR description as follows.

$$SNR \approx \frac{P_{Rx,max}}{N_0}, \quad (2.41)$$

where

$$N_0 = -174 + 10 \cdot \log_{10}(W) + F_{dB} \quad (2.42)$$

is the additive white Gaussian noise at the receiver signal in dBm where W is the signal bandwidth in Hz and F is the noise figure in dB.

We can also observe the SNR dependence on transmitter-IRS and IRS-receiver distances through $r_{Tx,IRS,n}$, and $r_{IRS,Rx,n}$, and also with the incident angle and departure angle. The equivalent end-to-end Signal-to-Noise Ratio (SNR) has been quantified using this model, and it shows that to maximize the SNR, the IRS should be positioned more closely to the receiver than the transmitter.

Model by Tang *et al.* (2021) [48]

The third model we consider is presented in [48]. The authors assume the normalized IRS unit cell radiation pattern as shown below with elevation angle θ and azimuth angle φ .

$$F(\theta, \varphi) = \begin{cases} \cos^3 \theta & \theta \in [0, \pi/2], \varphi \in [0, 2\pi] \\ 0 & \theta \in [\pi/2, \pi], \varphi \in [0, 2\pi] \end{cases} \quad (2.43)$$

They are placed in the x - y plane in the form of a $M \times N$ array. The size of each unit cell is given by $a \times b$ along \vec{e}_x and \vec{e}_y respectively as depicted in Fig. 2.12. $\theta_{Tx}, \theta_{Rx}, \varphi_{Tx}$, and φ_{Rx} are the elevation and azimuth angles corresponding to the transmitter and receiver from the unit cell.

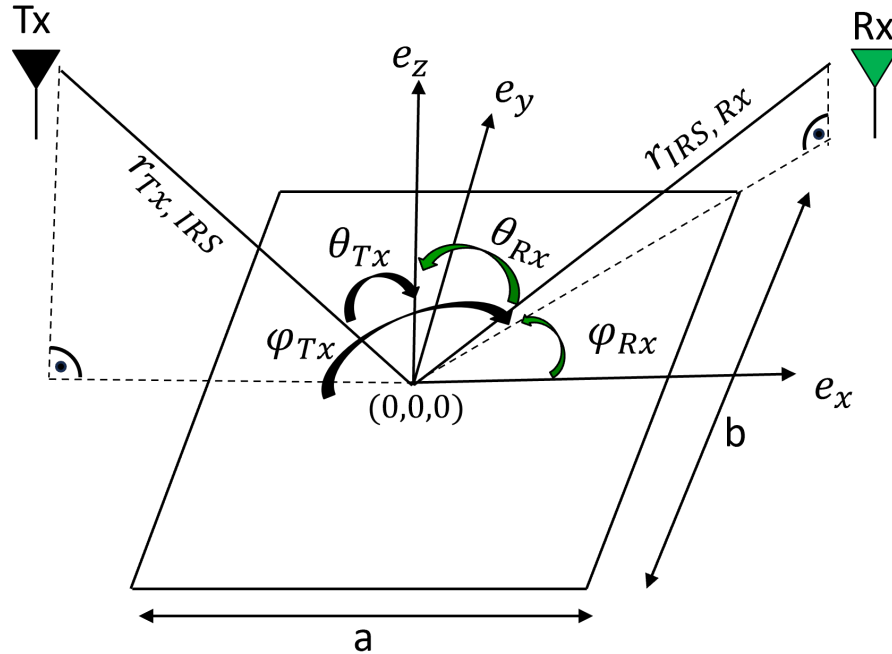


Figure 2.12: Illustration of the geometry of IRS-based channel and definitions used in the derivation of IRS channel model in [48].

The proof of this system includes the same method as the previous two models which motivates the derivation of the power received equation which begins by following the equations that give the power incident and the electric field on the unit cell.

$$P_{incident} = \frac{G_{Tx} \cdot P_{Tx} \cdot a \cdot b}{4 \cdot \pi \cdot r_{Tx,IRS}^2} F_{Tx}(\theta_{Tx}, \varphi_{Tx}) \quad (2.44)$$

$$E_{incident} = \sqrt{\frac{2 \cdot \eta \cdot P_{incident}}{a \cdot b}} e^{-j \frac{2 \cdot \pi \cdot r_{Tx,IRS}}{\lambda}}, \quad (2.45)$$

where η is the characteristic impedance of the air. According to the conservation of energy, the equation

$$P_{incident} \cdot |\Gamma|^2 = P_{reflect} \quad (2.46)$$

must hold up and the reflected signal power as received by the receiver is given as follows.

$$P_{received} = \frac{P_{reflect} \cdot A_r}{4 \cdot \pi \cdot r_{IRS,Rx}^2} F_{Rx}(\theta_{Rx}, \varphi_{Rx}) \quad (2.47)$$

By combining Eq. (2.44), Eq. (2.46), and Eq. (2.47), we can achieve the electric field of the received reflected signal from the unit cell.

$$E_{reflect} = \sqrt{\frac{2 \cdot \eta \cdot P_{received}}{A_r}} e^{-j \left(\frac{2 \cdot \pi \cdot r_{Tx,IRS}}{\lambda} + \frac{2 \cdot \pi \cdot r_{IRS,Rx}}{\lambda} - \phi_{m,n} \right)}, \quad (2.48)$$

where $-(\frac{2 \cdot \pi \cdot r_{Tx,IRS}}{\lambda} + \frac{2 \cdot \pi \cdot r_{IRS,Rx}}{\lambda} - \phi_{m,n})$ is the phase alteration due to the signal propagation and the reflection coefficient of the unit cells [48]. The power received at the receiver is given by Eq. (2.49).

$$P_{Rx} = \frac{|E_r|^2}{2 \cdot \eta} A_r \quad (2.49)$$

$$A_r = \frac{G_{Rx} \cdot \lambda^2}{4 \cdot \pi} \quad (2.50)$$

The derivation steps by the authors in [48] lead to the following steps which are similar to the previously presented models, where the following equation for the received power at the RX is given.

$$P_{Rx} = \frac{P_{Tx} \cdot G_{Tx} \cdot G_{Rx} \cdot a \cdot b \cdot \lambda^2}{64 \cdot \pi^3} \cdot \left| \sum_{m=1-M/2}^{M/2} \sum_{n=1-N/2}^{N/2} \frac{\sqrt{F_{m,n}^{combine}} \cdot \Gamma}{r_{Tx,IRS} \cdot r_{IRS,Rx}} e^{-j \frac{2 \cdot \pi (r_{Tx,IRS} + r_{IRS,Rx})}{\lambda}} \right|^2, \quad (2.51)$$

where $F_{m,n}^{combine} = F_{m,n}^{Tx} \cdot F_{m,n}^{Rx}$. Together with all these, the authors have derived Eq. (2.51). It shows the proportionality relationship between all factors similar to that of the other two models. Eq. (2.49) is considered as the general formula, which is proportional to the size of the unit cell, gains of the transmitter/receiver antennas, their normalized power radiation function, and the distances between Tx-IRS and IRS-Rx.

2.3.4 IRS Reflection Gains in Existing Channel Models

We have used path loss equations from the papers [46–48] as examples of IRS channel models from the literature. This section now focuses on isolating and highlighting the elements that uniquely relate to the reflector to make the models compatible with arbitrary channel models for the propagation losses modeling the subchannels between Tx and IRS as well as IRS and Rx.

The power received equations by the three IRS models: Eq. (2.28), Eq. (2.38), and Eq. (2.51) are given in Sec. 2.3.3. In this part, the variables that solely represent the impact of the transmitter and receiver in each of these models are defined. The other variables, which are mostly affected by the reflector, are also isolated. The results are intended to separate the individual contributions to the total power received from the transmitter, receiver, and reflector. In addition, Tab. 2.5 presents the gain formula that was obtained from the IRS models that were previously presented. Notably, this table ensures a uniform and consistent representation of angle definitions throughout the entire model by methodically replacing the angles used by the authors with definitions presented in our thesis in Sec. 2.3.3. This modification improves the coherence and clarity of the interpretation of the IRS models' output.

Building on Tab. 2.5's basis, we compare the parameters therein to do a thorough analysis for a deeper comprehension. Tab. 2.6 presents a graphical depiction of this analysis, highlighting similarities and differences across the factors. Interestingly, the square of the dimensions, the size of the reflector, and the reflection coefficient all show a direct relationship with each gain equation. Furthermore, the inverse square relationship with wavelength highlights the impact of frequency concerns.

Table 2.5: Gains at the reflector from the three IRS models [46–48] which are derived from the respective receive power equations.

Model	Receive Power Equation	Derived IRS Gain
[46]	Eq. (2.28)	$G_{IRS[Ozd20]} = \left(\frac{\Gamma \cdot a \cdot b \cdot M \cdot N}{\lambda} \right)^2 \cos^2 \left(\frac{\gamma_{Tx}}{\sqrt{2}} \right) \left(\text{sinc} \left(\frac{\pi \cdot b}{\lambda} \right) \left(\sin \left(\frac{\gamma_{Rx}}{\sqrt{2}} \right) - \sin \left(\frac{\gamma_{Dev}}{\sqrt{2}} \right) \right) \right)^2 \quad (2.52)$
[47]	Eq. (2.38)	$G_{IRS[Nton21]} = \left(\frac{\Gamma \cdot a \cdot b \cdot M \cdot N}{\lambda} \right)^2 \cdot \cos \left(\frac{\gamma_{Tx}}{\sqrt{2}} \right) \cdot \cos \left(\frac{\gamma_{Rx}}{\sqrt{2}} \right) \quad (2.53)$
[48]	Eq. (2.51)	$G_{IRS[Tang21]} = \left(\frac{\Gamma \cdot a \cdot b \cdot M \cdot N}{\lambda} \right)^2 \cdot \cos^3 \left(\frac{\gamma_{Tx}}{\sqrt{2}} \right) \cdot \cos^3 \left(\frac{\gamma_{Rx}}{\sqrt{2}} \right) \quad (2.54)$

Table 2.6: Characterization of IRS gain models [46–48] with their parameter dependencies at 28 GHz frequency. The green and red boxes depict the similarities and dissimilarities between the three IRS models, respectively.

Model	Gain at IRS	Unit-cell size	Number of unit-cells	Reflection Coefficient	Wave-length	Incident Wave	Reflected Wave	Reflection pattern support
[46]	Eq. (2.52)	$(a \cdot b)^2$	$(M \cdot N)^2$	Γ^2	$\frac{1}{\lambda^2}$	$\cos^2\left(\frac{\gamma_{Tx}}{\sqrt{2}}\right)$	Constant	Yes, via γ_{Dev}
[47]	Eq. (2.53)	$(a \cdot b)^2$	$(M \cdot N)^2$	Γ^2	$\frac{1}{\lambda^2}$	$\cos\left(\frac{\gamma_{Tx}}{\sqrt{2}}\right)$	$\cos\left(\frac{\gamma_{Rx}}{\sqrt{2}}\right)$	No
[48]	Eq. (2.54)	$(a \cdot b)^2$	$(M \cdot N)^2$	Γ^2	$\frac{1}{\lambda^2}$	$\cos^3\left(\frac{\gamma_{Tx}}{\sqrt{2}}\right)$	$\cos^3\left(\frac{\gamma_{Rx}}{\sqrt{2}}\right)$	No

A green box in the table highlights these similarities. Still, as can be seen from a red box in the table, the main differences between these elements are in the cosine exponents and the support of radiation patterns. This comparative analysis offers insightful information about the connections and differences between the analyses.

Furthermore, the model [46] varies in that it supports IRS reflection patterns by utilizing γ_{Rx} as the angles at which the IRS pattern is sampled, whilst the target reflection angles are defined by a distinct parameter γ_{Dev} . The other models in γ_{Rx} combine these two parameters so that only one gets the peak gain when the reflection direction and sample reflection angle coincide.

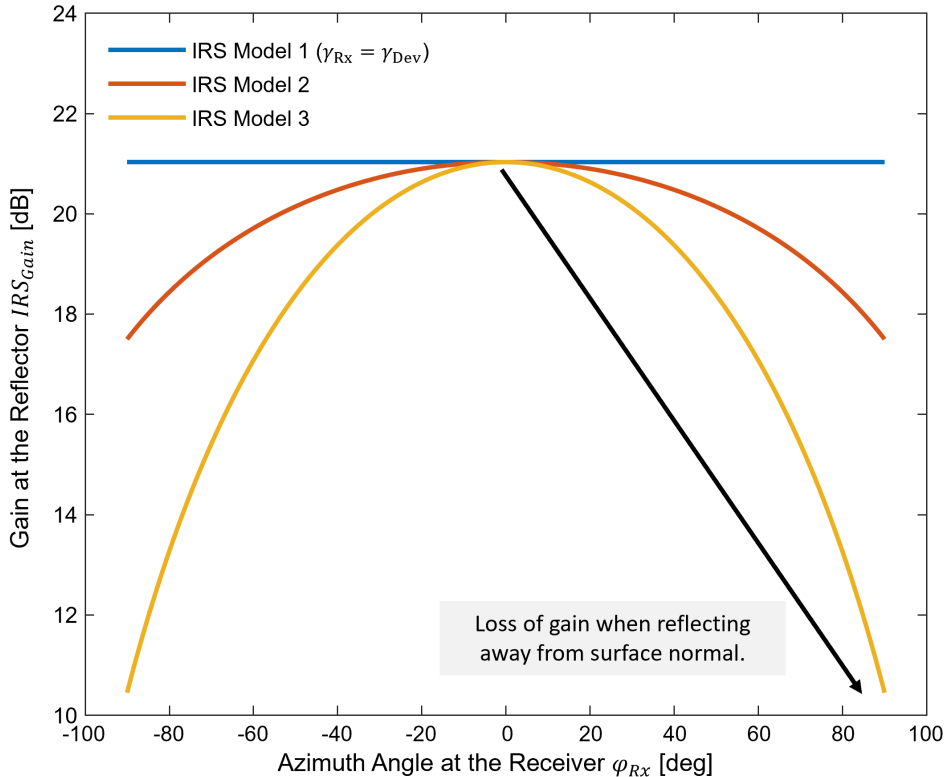


Figure 2.13: Gain at the reflector in dB depicting the comparative results of the three IRS models [46–48] at 28 GHz frequency, $a = b = 50 \cdot \lambda$, $\theta_{Tx} = \varphi_{Tx} = 0^\circ$, and $\theta_{Rx} = 0^\circ$ with sweep along φ_{Rx} .

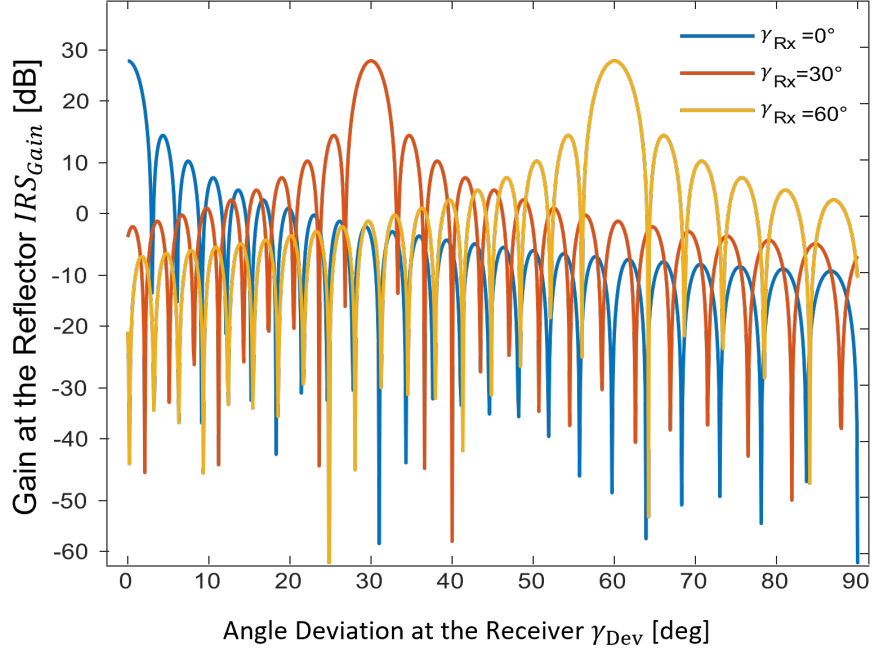


Figure 2.14: Gain at the reflector depicting the support of radiation pattern in [46] when sweeping along the receiver i.e., $\gamma_{Rx} \neq \gamma_{Dev}$ for different placement of the receiver γ_{Rx} . A notable peak is observed for each γ_{Rx} curve and the curve gradually decreases after this point. Additional parameters, $a = b = 50 \cdot \lambda$ at 28 GHz frequency and $\theta_{Tx} = \varphi_{Tx} = 0^\circ$.

The comparison of Tab. 2.6 can be seen in Fig. 2.13, where we assume the transmitter and receiver are orthogonal to the surface, operating with a frequency of 28 GHz with unit cell dimensions $a = b = 50 \cdot \lambda$, and $N = M = 50$ with $\gamma_{Dev} = 0^\circ$. The figure depicts that maximum is attained at an azimuth angle 0° and the curve slowly decreases on either side, as the loss is incurred as we move away from the surface normal. The straight line behavior in a model [46] is when the user is at an angle where IRS is pointing, i.e., $\gamma_{Rx} = \gamma_{Dev}$. Sweep from this point will support the radiation pattern as shown in Fig. 2.14. The plot of IRS gain vs receiver deviation angles shows separate peaks for different receiver positions. These peaks represent optimal points where the IRS considerably improves signal strength and quality, demonstrating the efficiency of IRS technology in beamforming and signal optimization for varied receiver positions.

All of these derivations of IRS models are based on the Radar Cross Section which we discuss later in Sec. 3.3.

2.4 Scope of Thesis

The previous sections have provided a thorough background on mmWave communications and particularly motivated the need for reflecting surfaces. Metasurfaces in the form of IRSs have risen

as a hot topic in 6G research [49–52]. Consequently, according end-to-end channel models have been developed.

As we have pointed out in this section, passive reflectors such as in the form of HELIOS reflectors are an alternative solution that comes with advantages in terms of compatibility with existing communication standards and zero-energy consumption. An analytical description for such is of utmost importance to realize HELIOS-enabled mmWave communications. Likewise, the goal of this master thesis is to derive such a description and compare it with the above IRS models. Similar to existing works, we aim to showcase the benefits of this model, particularly by using it in the context of an urban sample mmWave deployment scenario.

3 Simulation and Analytical Modeling of HELIOS Reflectors

This section develops an analytical model for the reflection behavior of HELIOS reflectors that are co-designed/validated via numerous EM simulations. First, we introduce the methodology of this in Sec. 3.1. After laying the groundwork, Sec. 3.2 studies key reflection characteristics of HELIOS reflectors using an EM simulator. Thereafter, Sec. 3.3 develops an analytical model for the reflection of individual HELIOS modules by building upon an existing radar cross-section formulae for flat plates and extending it according to the prior simulation results. Lastly, Sec. 3.4 extends the analytical model to HELIOS reflectors to make up an array of individually parameterized modules. The thesis would focus on considering the self-shadowing effects that may occur between neighboring modules.

3.1 Methodology

It is crucial to recognize that HELIOS is made up of a collection of HELIOS modules that all follow the same geometry template [10]. However, the study draws attention to the unique feature that these modules may have different α and β slopes. The corresponding paragraphs of Sec. 2.3.2 provide a more thorough explanation of this deviation from uniformity, highlighting the importance of these subtle adjustments to the overall structure and functionality of the HELIOS array. Using the author's definition in [10], we have constructed and integrated the geometry in the Ansys HFSS software which is a commercial EM simulation tool. We use the simulator as the fundamental physical prediction of the exhibited HELIOS reflection pattern which is strongly dependent on the geometry but also the angles of arrival of the incident EM wave.

The analytical modeling of the reflection behavior of arbitrarily configured HELIOS reflectors in Sec. 3.3, and Sec. 3.4 relies heavily on these simulative insights, particularly our initial detailed simulation study in Sec. 3.2. Owing to this, we now outline the simulation workflow being used to attain the results presented in the forthcoming sections. We note that other commercial EM simulation tools offer the same functionality and should therefore operate similarly.

Fig. 3.1 sketches the parametrization of the EM simulations of the HELIOS reflectors, thus providing a methodical and data-driven approach to investigate how key performance metrics, extractable from the simulation results for the specified far-field observation range, depending on the

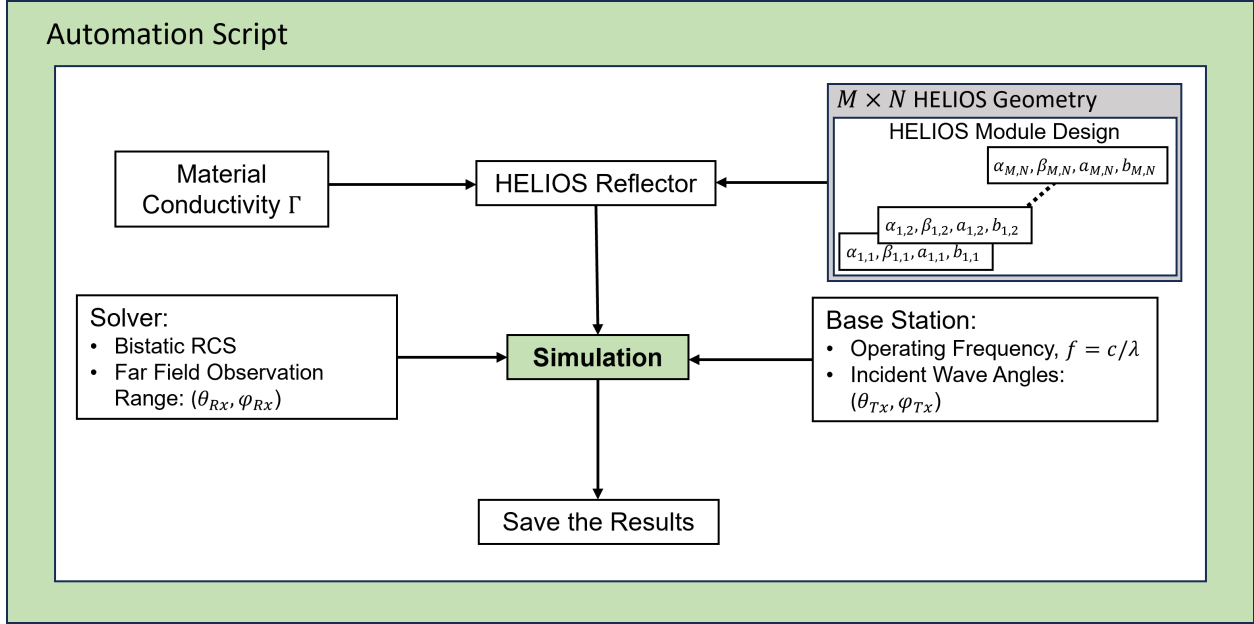


Figure 3.1: Illustration of the EM simulation workflow of the HELIOS reflectors. Simulation parameters in terms of base station configuration, far-field settings, and HELIOS reflector may be changed as desired for each simulation using an automation script.

reflector configuration. In the above figure, an external IronPython script is used to automate the simulations in this case, which provides the simulation configuration in terms of the parametrization of the HELIOS reflector configuration under test as well as the scenario in terms of the incident wave, reflection observation angle range, and operating frequency. Here, the frequency is typically 28 GHz, which lies in the 5G n257 mmWave frequency band. The saved results are then analyzed using the MathWorks MATLAB tool to draw sensible conclusions. This knowledge shall then be used during the development of the analytical model in Sec. 3.3, and Sec. 3.4.

Horizontal and vertical angles of incidence as well as of departure will all adhere to $\varphi_{Tx}, \theta_{Tx} \in [-90, 90]^\circ$ using the coordinate system defined in Sec. 2.3.3. These angles of incidence will be varied in this study to consider different deployment scenarios. The far-field observation range typically constitutes the half-sphere spanned by the above-defined range. Due to the simulation complexity, the resolution of simulation for this set of angles differs depending on, e.g., the HELIOS reflector size. For each of these points along the half-sphere, the EM simulator calculates the bistatic RCS (see Sec. 3.3).

As discussed before, each HELIOS reflector element (m, n) consists of four crucial parameters, i.e., dimensions $a_{m,n}$, and $b_{m,n}$ being the footprint sizes along y and z -axes, respectively, and slopes $\alpha_{m,n}$, and $\beta_{m,n}$ constituting the horizontal and vertical slopes, respectively. The whole HELIOS reflector consists of $M \times N$ elements with $m \in 1, \dots, M$ and $n \in 1, \dots, N$, cf. Sec. 2.3. In this work, we assume that all individual elements have the same footprints, i.e., $a = a_{m,n} \in m, n$ and $b = b_{m,n} \in m, n$. Therefore, there are $2 \cdot N \cdot M + 2$ parameters constituting a HELIOS geometry. In the scope of Sec. 3.2, the impact of selecting different common materials will be tested. In

addition, artificial materials with arbitrary conductivity will be studied. Thereafter, copper will be used as the HELIOS baseline material as in [10]. The term "Gain" refers to the RCS, as elucidated in Sec. 3.3, throughout this work. This application of the term gain is consistent with the definition given in Sec. 2.3.3, which presents a direct comparison of all three IRS models. A cohesive and seamless interpretation of the RCS behavior across different model comparisons is ensured by the study's maintenance of terminology compatibility.

3.2 Simulative Analyses of HELIOS Reflector Modules

In this section, we thoroughly assess the reflection characteristics of a single-element HELIOS reflector to shed light on how it behaves for various parameter combinations. This section is divided into three sections, each of which focuses on a different component of the evaluation. The study looks into the effects of changing slope angles in Sec. 3.2.1 to comprehend how these changes affect the system as a whole. In Sec. 3.2.2, the impacts of different reflector sizes are examined to determine how size variations affect the system's performance. In conclusion, Sec. 3.2.3 delves into the effects of altering the materials that make up the reflecting surface, thereby offering a comprehensive understanding of how distinct materials influence the overall performance and effectiveness of the reflective system.

3.2.1 Variation of Slope Angle

Using the fundamental HELIOS idea as a starting point, a significant departure from the established law of reflection i.e., $\varphi_{Rx} \neq -\varphi_{Tx}$ and $\theta_{Rx} \neq -\theta_{Tx}$ appears. Fig. 3.2 shows the design of the HELIOS reflectors with the size of the reflectors a and b as well as the slope angles α and β , which are intricately related to the dimensions of the reflecting surface. The model here assumes that have incident wave is orthogonal to the reflector module base ($\theta_{Tx} = \varphi_{Tx} = 0^\circ$). As presented by the authors in [10], this results in a noticeable change in the reflected angle by two times the slope angle, see Eq. (3.1) and Eq. (3.2) below.

$$\theta_{Rx} = -\theta_{Tx} + 2 \cdot \beta \quad (3.1)$$

$$\varphi_{Rx} = -\varphi_{Tx} + 2 \cdot \alpha \quad (3.2)$$

In our first simulative study, we focus on the variation of the horizontal slope angle α within the range of $[0 : 80]^\circ$, in our effort to comprehend the complex dynamics of our HELIOS reflector modules. This investigation is essential in figuring out how slope angles affect the behavior of the model. Let us consider a simplified scenario where vertical slope angle $\beta = 0^\circ$ is held constant to validate these intriguing results and the variation in φ_{Rx} as a function of α to best illustrate the essence of this experiment (see Fig. 3.3). Notably, within the range of α from 0° to 45° ,

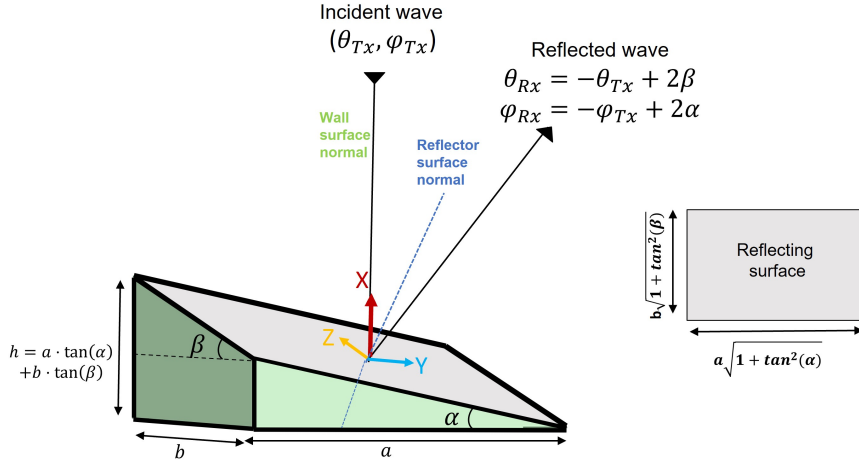


Figure 3.2: HELIOS module with the implementation of α and β slope angles with incident wave orthogonal to the reflector base i.e., $\theta_{Tx} = \varphi_{Tx} = 0^\circ$ and reflected wave validating HELIOS concept [10] with two times shift in the slope angles.

Eq. (3.1) and Eq. (3.2) accurately capture the behavior of the model. Beyond the 45° threshold of α , something different happens because the term $2 \cdot \alpha$ exceeds 90° .

This behavior as shown in Fig. 3.3, causes the beams to go beyond the limits of the considered far-field, resulting in a seeming saturation effect. The reason for this behavior is the energy being reflected behind the reflector which can be seen on the right side of the figure Fig. 3.3. As such, these results show that HELIOS modules can indeed direct the reflection into a target direction by setting $\alpha = (\varphi_{Rx} + \varphi_{Tx})/2$ and $\beta = (\theta_{Rx} + \theta_{Tx})/2$.

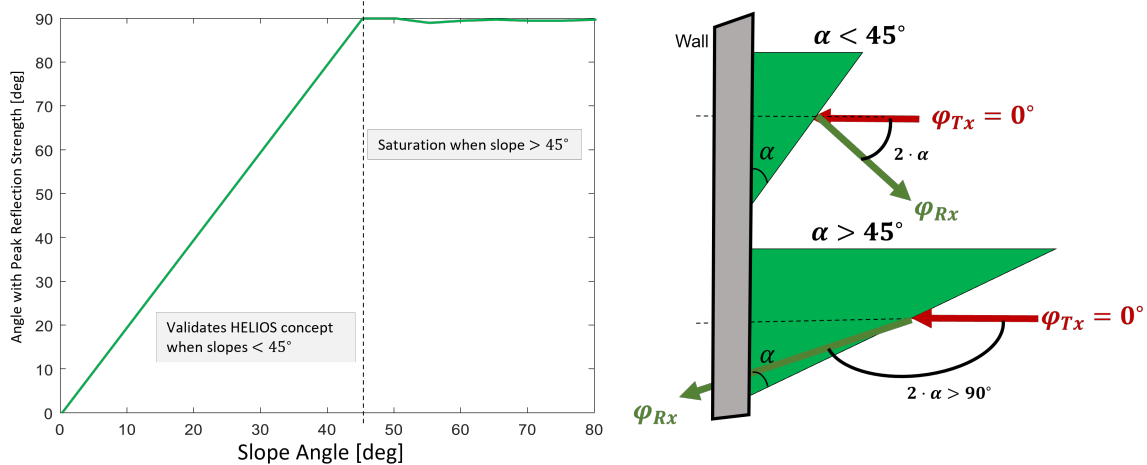
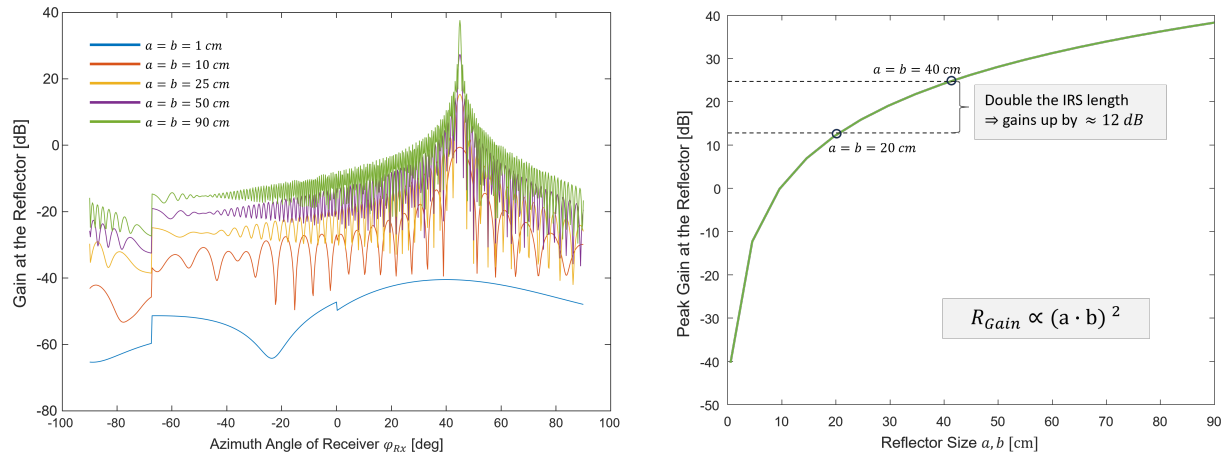


Figure 3.3: Assessment of the peak reflection angle given $\varphi_{Tx} = \theta_{Tx} = 0^\circ$ and different module slopes. We observe that reflection angle $\varphi_{Rx} = -\varphi_{Tx} + 2 \cdot \alpha$ and we note that the saturation for slopes $< 45^\circ$ is misleading as this depends on the angle of arrival of the incident wave and, in particular, is caused by the maximum reflection angle being outside the specified observation angle range for the simulation. This is because the energy is reflected behind the reflector as sketched on the right side.



(a) Azimuth angle variation at the reflector for various reflector sizes, plotted against gain in dB at 28 GHz frequency with slope angle $\alpha = 22.5^\circ$ with $\theta_{Rx} = 0^\circ$. Notably, the beams become narrower as the reflector size increases.

(b) Behavior of HELIOS module for varying reflector size a and b when plotted against peak gain in dB. A notable increase in gain by 12 dB is observed when the reflector size is doubled.

Figure 3.4: Illustration of the impact of the variations in reflector sizes of HELIOS module on the beam pattern and peak gain at the reflector as the size increases.

3.2.2 Effect of Different Reflector Sizes

We now make a complementary investigation of the impact of the HELIOS element footprint dimensions a and b with $a = b$ in the range from 1 to 90 cm.

The simulation results in Fig. 3.4(a) illustrate that larger reflecting surfaces produce a higher gain. Moreover, with increasing size, the main lobe also becomes more narrow such that energy is reflected in a more concentrated fashion. The results in Fig. 3.4(b) match the analytical modeling carried out in Sec. 2.3.3 in regards to the maximal gain which scales with $(a \cdot b)^2$, cf. gain increase by 40 dB when increasing the surface area by a 100 from $a = b = 1 \text{ cm}$ to $a = b = 50 \text{ cm}$. As observed from the same figure, as we double the size of the reflector from $a = b = 20 \text{ cm}$ to $a = b = 40 \text{ cm}$, the peak gain increases by almost 12 dB. This result confirms that reflector size is a key metric to be tuned to attain the necessary power gains for mmWave beyond LOS connectivity.

3.2.3 Impact of Reflecting Surface Material

Lastly, we study the impact of material properties on the reflection behavior. In the first part, we consider seven different real materials. Thereafter, we consider the impact of the material conductivity directly. First, we consider the maximum gain by HELIOS modules based on the seven materials given in Tab. 3.1. The maximum gains observed in Fig. 3.5(a) underline that high material conductivity results in stronger reflections. As a result, high gains can only be realized by using large reflecting surfaces (cf. Sec. 3.2.2) and correct slope angles (cf. Sec. 3.2.1) in

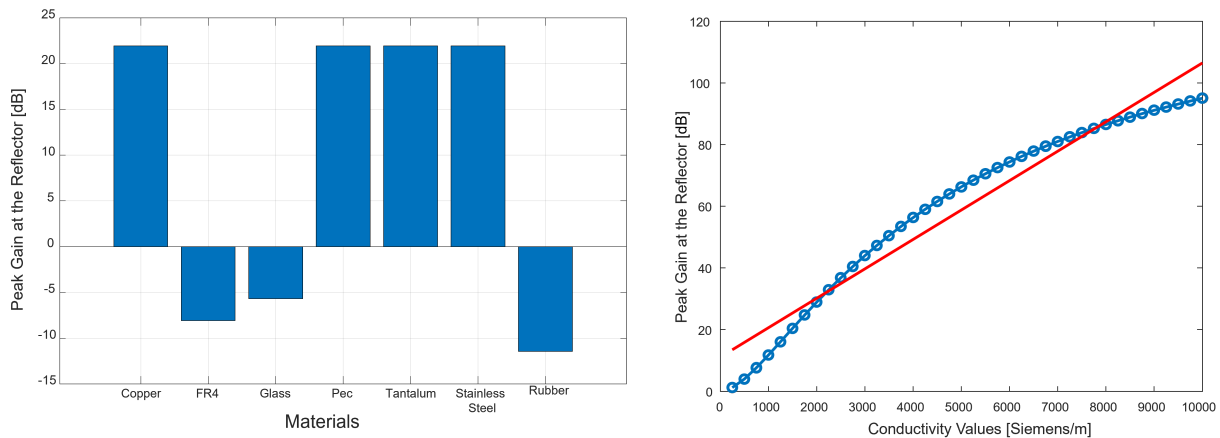
Table 3.1: Properties of different materials in terms of conductivity and relative permittivity.

Materials	Conductivity (S/m)	Relative Permittivity
Copper	58,000,000	1
FR4	0	4.4
Glass	0	5.5
Perfect Electric Conductor	1e+30	1
Tantalum	6,300,000	1
Stainless Steel	1,100,000	1
Rubber	0	3.0

combination with a suitable reflecting surface material such as copper. Since the four materials yielding high gains have very similar peak gains, we now do a sensitivity analysis for a wide range of conductivity values using an artificial material, copper, and only alter the conductivity parameter as needed.

The sweep range is between 0 to 10,000 S/m and thus exceeds the conductivity of glass, FR4, and rubber by far. However, the value is much smaller than that of, e.g., copper. The findings, as shown in Fig. 3.5(b), underline that the reflection gain does indeed depend nearly linearly on the material conductivity, as underlined by the linear regression curve (red). This behavior matches the IRS model dependence on parameter Γ in Sec. 2.3.3.

The potential to use these materials to improve the performance of our HELIOS reflector modules in practical applications is highlighted by the intriguing consistency between the behavior of high conductivity materials and the IRS models. We are better able to design and deploy our modules for practical and efficient use if we are aware of these subtle interactions between materials and their conductivity values.



(a) Effect of different materials on HELIOS module when plotted against the gain in dB. Parameters: $\alpha = 22.5^\circ$, $\beta = 0^\circ$, $a = b = 50 \cdot \lambda$ with incident wave $\varphi_{Tx} = \theta_{Tx} = 0^\circ$ at 28 GHz frequency.

(b) Peak reflection gains from simulations utilizing copper with modified conductivity as the base material of a HELIOS reflector module (blue). Linear regression curve (red) underlines roughly linear dependence on conductivity in the considered range.

Figure 3.5: The influence of a reflecting surface on gain for various materials based on their conductivity and relative permittivity.

3.3 Analytical Modeling of HELIOS Modules

This section makes the crucial first step in developing the analytical model for the reflection characteristics of HELIOS reflectors by first considering only an individual HELIOS module. This is in coordination with the simulation results in Sec. 3.2 and the analytical models for IRSs in Sec. 2.3.3. For this purpose, we introduce the notion of the radar cross section in Sec. 3.3.1 which was already previously set to be the solution type of the EM wave simulator, cf. Sec. 3.1. In Sec. 3.3.3, we will discuss how RCS can be analytically adapted to HELIOS reflectors by also doing assessments with the EM simulation results in Sec. 3.3.4.

3.3.1 Bistatic Radar Cross Section

The RCS concept is a crucial tool in this thesis. It allows us to characterize how objects, in this case, our HELIOS model, interact with electromagnetic waves. RCS is a fundamental concept in radar engineering and electromagnetic scattering [11, 12]. When an object is illuminated by electromagnetic waves, usually carrying radar signals, the RCS describes the scattered power per unit solid angle from the object. It offers information about how "visible" an object is to radar systems. By describing the RCS of HELIOS reflectors in this thesis, our model may be used to estimate how it will appear to wireless systems such as 5G/6G.

The radar equation below shows how the RCS σ_{Meta} can be considered in a channel model [53]. But first, it needs to be determined as follows. The formula in Eq. (3.3) gives the common definition of the RCS, which is written as the limit of the distance r to infinity.

$$\sigma_{Meta} = \lim_{r \rightarrow \infty} 4\pi r^2 \frac{|E_{Rx}|^2}{|E_{Tx}|^2}, \quad (3.3)$$

where σ_{Meta} ¹² is the RCS for the metasurface, and E_{Rx} and E_{Tx} are the far-field reflected and incident electric field intensities, respectively. As such, it is the ratio of incident and reflected wave in the infinite far-field. Fixing the direction of the incident wave and varying the considered reflection angle, the RCS becomes a multivariate reflection pattern similar to an antenna pattern [54, 55]. Tab. 3.2 below provides the standard RCS values that are usually encountered in the communication link. A non-zero σ_{Meta} becomes relevant to account for real-world situations, including the existence of obstructions like a car within the communication channel. On the other side of the coin, a car typically comes with an RCS of 20 dBsm, which is larger than the 0 dBsm of a person, according to Tab. 3.2.

The application of bistatic RCS analysis necessitates a thorough comprehension of important variables, especially the angles of the incidence and departure which are crucial for evaluating randomly shaped scattering objects, in literature also referred to as radar targets [11, 58].

¹ σ_{Meta} has an additional unit of m² and for simplicity, we mention dB instead of dBsm.

²The term "Gain" refers to the RCS, as elucidated in Sec. 3.3, throughout this work.

Table 3.2: Standard RCS values which are commonly observed [56, 57].

Object	σ_{Meta} [dBm]
Man	0
Small bird	-20
Car	20
Large commercial airplane	20
Small fighter plane	3

The main reflection angle and magnitude of the scattered signal are strongly dependent on the angle of the incident and the shape of the object. To fully understand bistatic RCS one must first study the monostatic RCS, which is concerned with calculating the power reflected to the transmitting node [59]. When the transmitter and receiver are in the same place, monostatic RCS measures the amount of power that a scatterer reflects to the transmitting node, hence indicating the visibility of an object. Conversely, bistatic RCS measures reflected power when the transmitter and receiver are at different sites. This latter case is thus more relevant for 5G/6G mmWave communications, although the monostatic RCS can be of interest for future 6G joint communication and sensing (JCAS) use cases.

3.3.2 Analytical Model for the Reflection of Planar Surfaces

In literature, one may find a formula for the bistatic RCS of a rectangular plate. It depends on the following parameters:

- Plate dimensions and materials
- Carrier frequency
- Angles of incident and reflected wave

Taking into account the above-mentioned parameters, RCS formulas have been derived in literature [10–12] as follows:

$$\sigma_{plate} = 4 \cdot \pi \cdot \left(\frac{a \cdot b}{\lambda} \right)^2 \cdot \cos^2(\theta_{Rx}) \cdot \text{sinc}^2 \left(\frac{\pi \cdot b \cdot (\sin(\theta_{Rx}) \cdot \sin(\varphi_{Rx}) \pm \sin(\theta_{Tx}))}{\lambda} \right) \begin{cases} +, & \varphi_{Rx} = \frac{3\pi}{2} \\ -, & \varphi_{Rx} = \frac{\pi}{2} \end{cases} \quad (3.4)$$

Eq. (3.4) gives the RCS equation for a flat plate reflecting surface with dimensions a and b that operate at wavelength λ . This equation includes three critical supported angles: the incident elevation angle θ_{Tx} , the reflected elevation angle θ_{Rx} , and the azimuth angle of the receiving radar system φ_{Rx} . Notably, in the context of the reference used in our study [11], a specific assumption is made about the value of the incident azimuth angle φ_{Tx} , which is retained constant to 0° . In Eq. (3.4), the flatplate's orientation concerning the radar system is indicated by the different \pm symbols for $\sin(\theta_{Rx})$, $\sin(\varphi_{Rx})$, and $\sin(\theta_{Tx})$. In particular, the minus symbol indicates

the flatplate's front side, indicating that the side facing the radar transmitter and receiver is where incident radar waves interact. Whereas, the side opposite the incident radar waves is represented by the plus symbol, where the radar waves interact with the flatplate's hidden or obscured side. We concentrate on the front side of the plate for this thesis since it is oriented in a way that directly interacts with the radar system and offers important information about the RCS properties of the flatplate in our analytical framework.

3.3.3 Modeling of HELIOS Module Reflection

Having provided the fundamental RCS equation for a flat plate reflector in Eq. (3.4), we now need to modify the equation for use in the context of wireless communications and to match it to the HELIOS concept, as illustrated by Eq. (3.5), and Eq. (3.6). In this section, we will delve into the complexities of these modifications, illuminating the changes and adjustments made to attain the appropriate alignment.

$$\sigma_{Plate}(a, b, \lambda, \theta_{Tx}, \theta_{Rx}, \varphi_{Rx}) \quad (3.5)$$

$$\sigma_{Module}(a, b, \alpha, \beta, \lambda, \theta_{Tx}, \varphi_{Tx}, \theta_{Rx}, \varphi_{Rx}) \quad (3.6)$$

While the basic equation for a flat rectangular plate reflector provides a solid foundation, the unique characteristics of the HELIOS model need the inclusion of further parameter dependencies, i.e., φ_{Tx} , α , and β , cf. Eq. (3.6).

Tab. 3.3 emphasizes the important changes made to develop the improved HELIOS equation. The dimensions of a flat plate are $a \times b$, which is basically with slope angles $\alpha = \beta = 0^\circ$, HELIOS introduces a more complex geometry with dimensions that vary dynamically with a, b, α , and β values, as can be seen in Fig. 3.6. Another notable modification is the addition of the supported angle φ_{Tx} . Unlike the flat plate, we do not assume that $\varphi_{Tx} = 0^\circ$.

Table 3.3: Comparing the existing equation for flat plate, cf. Eq. (3.5) which is used for the adaptation of our RCS equation for the HELIOS analytical module, cf. Eq. (3.6), focusing on the changes implemented.

Aspects	Equation for flat plate, cf. Eq. (3.5)	Equation for the HELIOS module, cf. Eq. (3.6)
Reflecting surface size	$a \cdot b$	$a \cdot \sqrt{1 + \tan^2(\alpha)} \cdot b \cdot \sqrt{1 + \tan^2(\beta)}$
Supported angles	$\theta_{Tx}, \theta_{Rx}, \varphi_{Rx}$	$\theta_{Tx}, \theta_{Rx}, \varphi_{Tx}, \varphi_{Rx}$
Rotation of reflecting surface	none, fixed to y - z -plane	Substitute angles by: $\theta_{Tx} \leftarrow (\theta_{Tx} - \beta)$ $\theta_{Rx} \leftarrow (\theta_{Rx} - \beta)$ $\varphi_{Tx} \leftarrow (\varphi_{Tx} - \alpha)$ $\varphi_{Rx} \leftarrow (\varphi_{Rx} - \alpha)$
Beamwidth correction factor in sinc argument	1	$\frac{1}{2}$

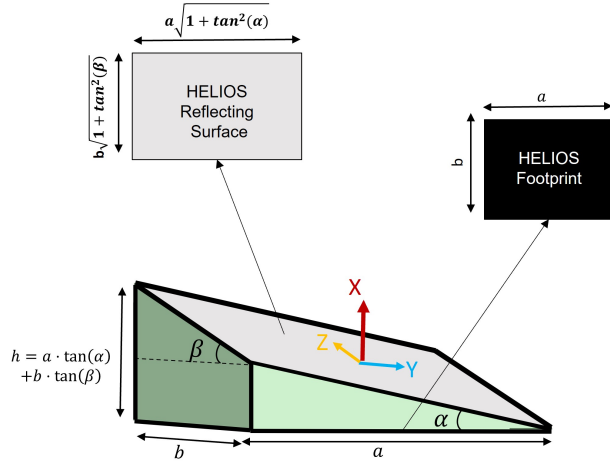


Figure 3.6: Geometric relation between HELIOS footprint size given by $(a \cdot b)$, and reflecting surface size given by $(a \cdot \sqrt{1 + \tan^2(\alpha)} \cdot b \cdot \sqrt{1 + \tan^2(\beta)})$, where a and b are the length and width of the module.

In the above figure, HELIOS footprint with size $a \times b$ is the flatplate dimensions, whereas the HELIOS reflecting surface's dimension is $(a \cdot \sqrt{1 + \tan^2(\alpha)} \times b \cdot \sqrt{1 + \tan^2(\beta)})$.

Furthermore, the slope angles α , and β of the HELIOS module affect the main lobe reflection angles θ_{Rx} and φ_{Rx} as summarized by Eq. (3.1) and Eq. (3.2). As the Snell's law still holds along the shifted surface's normal vector, this rotation aspects is implemented by a coordinate transformation shifting by α , and β . As a result, the angles of incidence θ_{Tx} and φ_{Tx} in the equation are replaced by $\theta_{Tx} - \beta$ and $\varphi_{Tx} - \alpha$. The same holds for the angles of departure. To ensure that the beamwidth matches the simulated values, the literature already includes a scaling factor $\frac{1}{2}$ by default, allowing for a more precise match of the theoretical model with a HELIOS module's real-world behavior.

Based on all of the above changes, an individual HELIOS module exhibits the following bistatic RCS holding for θ_{Tx} , φ_{Tx} , θ_{Rx} , and $\varphi_{Rx} \in [-90, 90]^\circ$:

$$\sigma_{module} = 4 \cdot \pi \cdot \Gamma \cdot \left(\frac{(a \cdot \sqrt{1 + \tan^2(\alpha)}) \cdot (b \cdot \sqrt{1 + \tan^2(\beta)})}{\lambda} \right)^2 (\cos^2(\theta_{Tx} - \beta) \cdot \cos^2(\theta_{Rx} - \beta) \cdot \cos^2(\varphi_{Rx} - \alpha)) \\ \left(\text{sinc}\left(\frac{1}{2} \cdot k \cdot b \cdot \sqrt{1 + \tan^2(\beta)} \cdot (\sin(\theta_{Rx} - \beta) \cdot \cos(\varphi_{Rx} - \alpha) - \sin(\theta_{Tx} - \beta) \cdot \cos(\varphi_{Tx} - \alpha))\right) \right)^2 \\ \left(\text{sinc}\left(\frac{1}{2} \cdot k \cdot a \cdot \sqrt{1 + \tan^2(\alpha)} \cdot (\cos(\theta_{Rx} - \beta) \cdot \sin(\varphi_{Rx} - \alpha) - \cos(\theta_{Tx} - \beta) \cdot \sin(\varphi_{Tx} - \alpha))\right) \right)^2 \quad (3.7)$$

Two sinc functions are presented in the equation, each of which individually affects the surface size's reflection properties for length and width. For the target's radar cross-section to be adequately represented, this separation is necessary. The diffraction phenomenon's sinc functions explain the reflecting surface's spatial extent along its dimensions, providing a thorough repre-

sentation of the target's scattering characteristics. The equation provides a more accurate and complete model for radar analysis by accounting for the distinct impacts of width and length on the reflected signal.

The insertion of the adjustments mentioned in the Tab. 3.3 into the fundamental Eq. (3.4) for a flat plate reflector leads to Eq. (3.7), constituting our analytical model for the bistatic RCS of an individual HELIOS module.

3.3.4 Assessment of Differences between Simulations and Analytical Model

In this section, we will conduct a detailed comparison of EM simulations and our previously provided analytical model to check matching properties and, in particular, to determine the extent to which there are discrepancies.

Fig. 3.7 shows the link between peak gain, defined as $\max(\sigma_{Module}(\varphi_{Rx}, \theta_{Rx}))$, attained and reflector width b in cm. The upper curves show the quadratic case in which $a = b$ in the range from 1 to 100 cm, whereas the lower curves show the rectangular case in which a is fixed to 10 cm and b again varies between 1 to 100 cm. These curves are based on our study in Sec. 3.2 and related work in Sec. 2.3.3, show a steady increase in gain as the reflector size increases. Notably, one observes a strong match between simulations and our analytical model. Both the curves from the analytical model and EM simulation results meet when $a = b = 10$ cm.

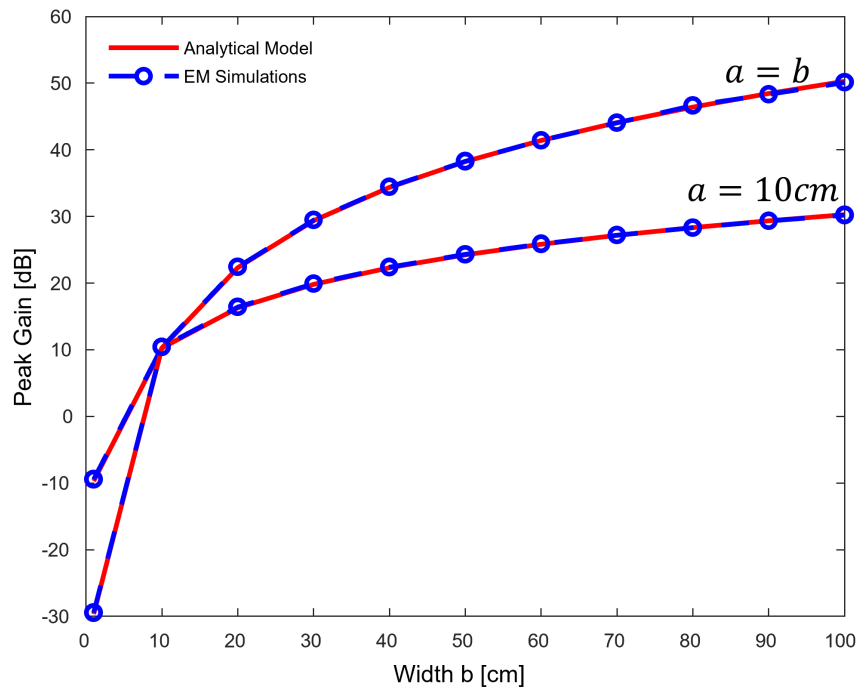
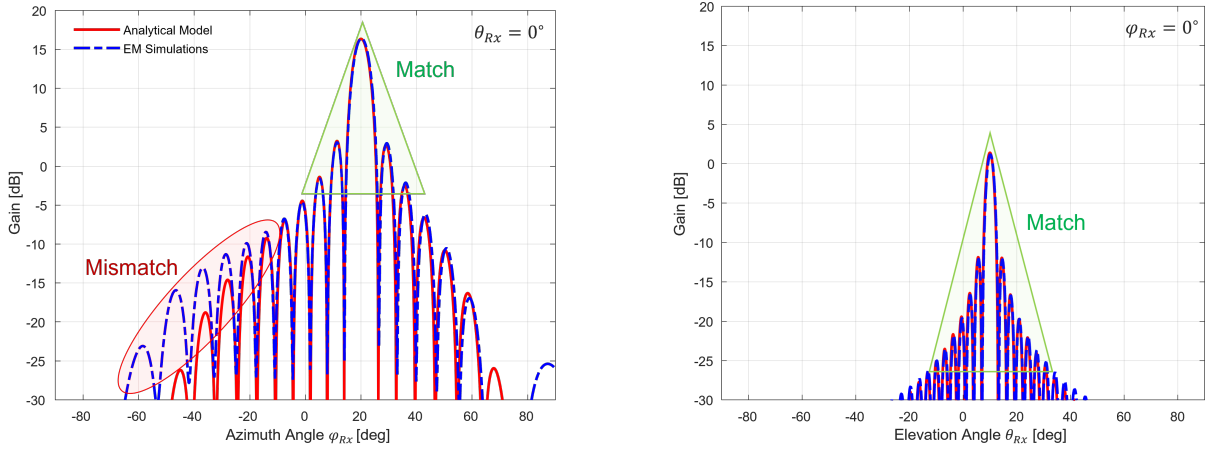


Figure 3.7: Comparison of peak RCS value yielded by simulation and analytical model for rectangular ($10\text{ cm} \times b$) and quadratic ($b \times b$) HELIOS module footprints, where we observe a matching behavior. Further parameters: $\varphi_{Tx} = \theta_{Tx} = 0^\circ$ and, $\alpha_{m,n} = \beta_{m,n} = 10^\circ$.



(a) Azimuth angle φ_{Rx} variation for a HELIOS module when $\theta_{Rx} = 0^\circ$ highlighting a match near the main lobe (green color) and a mismatch occurs further away (red color).

(b) Elevation angle θ_{Rx} variation for a HELIOS module when $\varphi_{Rx} = 0^\circ$ highlighting a match (green color) overall.

Figure 3.8: Validating the HELIOS concept along azimuth and elevation angle at the receiver and highlighting the similarities and differences between simulated and analytical models for a HELIOS module when $a = 10\text{ cm}$, $b = 20\text{ cm}$, $\alpha = 10^\circ$, and $\beta = 5^\circ$, and both $\varphi_{Tx} = \theta_{Tx} = 0^\circ$. A notable match in the peak gain is observed between the simulation results and the analytical model.

Fig. 3.8 depicts the horizontal (left) and vertical (right) slices of the bistatic RCS patterns from both the simulations and analytical model, respectively, for HELIOS reflector modules configured with $a = 10\text{ cm}$, $b = 20\text{ cm}$, $\alpha = 10^\circ$, and $\beta = 5^\circ$, and given a 28 GHz incident wave from direction $\varphi_{Tx} = \theta_{Tx} = 0^\circ$. In the horizontal pattern slice on Fig. 3.8(a), we observe the RCS peaks at $\varphi_{Rx} = 20^\circ = -\varphi_{Tx} + 2 \cdot \alpha$, thus confirming Eq. (3.2). Similarly, the vertical RCS pattern slices in Fig. 3.8(b) confirm that the RCS peaks of simulation and analytical model are indeed at $\theta_{Rx} = 10^\circ = -\theta_{Tx} + 2 \cdot \beta$, cf. Eq. (3.1). The beamwidth along φ_{Rx} depends on reflector dimension a , whereas θ_{Rx} depends on b . In Fig. 3.8, as the dimensions $b > a$, the vertical beamwidth (right) is narrower than the horizontal (left).

The interesting part in both these figures is that the simulated values closely match the analytical values, displaying exceptional behavior in the properties of their main and the first-order, N -th-order side lobes. But farther from the main lobes we see the mismatch along the azimuth angle, as depicted in Fig. 3.8(a) (red-colored). Our main region of interest shows a lot of similarities to that of simulated results (green-colored). Furthermore, a closer examination of these figures reveals the importance of beamwidth in the behavior of these systems which depends on the size of the reflector.

Fig. 3.9 shows the bistatic RCS heatmaps along reflection angles φ_{Rx} and θ_{Rx} with the gain being color coded. This allows for a qualitative visual comparison of the behavior attained by simulations and via the analytical model. The following parameters are used by the figure below: $a = b = 10\text{ cm}$ and $\alpha = \beta = 10^\circ$ with $\varphi_{Tx} = \theta_{Tx} = 0^\circ$. Notably, the reflected angle at which the maximum

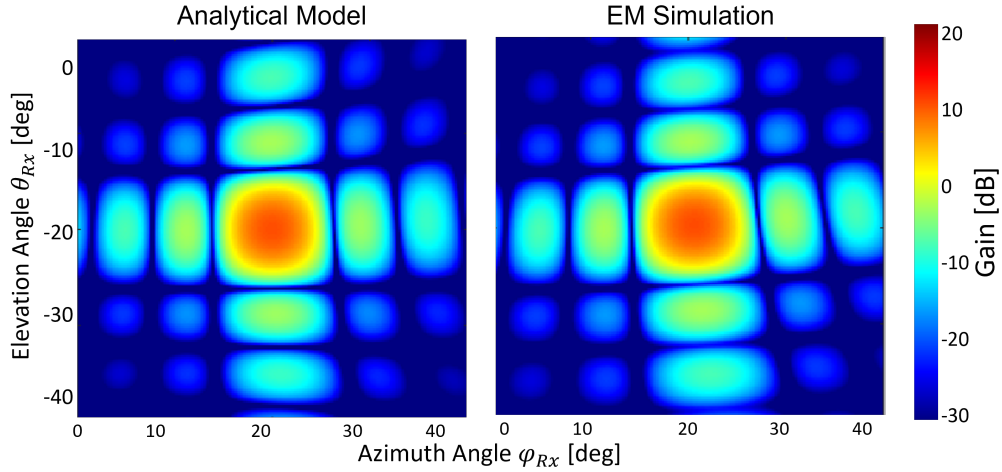


Figure 3.9: Sample RCS pattern of individual HELIOS module (1×1): (left) analytical model, (right) EM simulations for parameters $a = b = 10$ cm and $\alpha = \beta = 10^\circ$ at 28 GHz frequency with peak gain of 10.4 dB.

peak is attained validates the HELIOS concept. A closer look at the RCS heatmap behavior in the figure shows that the main lobe and the side lobes in both the analytical model and EM simulations match.

Further adaptation of the HELIOS reflector module at 38 GHz frequency is seen in Fig. 3.10. The peak gain by the analytical model and EM simulation results at 28 GHz frequency is around 10.4 dB, whereas at 38 GHz frequency is 13.0 dB. Because of their shorter wavelengths, reflectors typically show better gain characteristics at higher frequencies, such as 38 GHz, allowing for more directed and focused signal propagation. This variant highlights how carrier frequencies and reflector performance interact intricately in 5G mmWave scenarios, impacting the network's overall signal propagation and coverage properties.

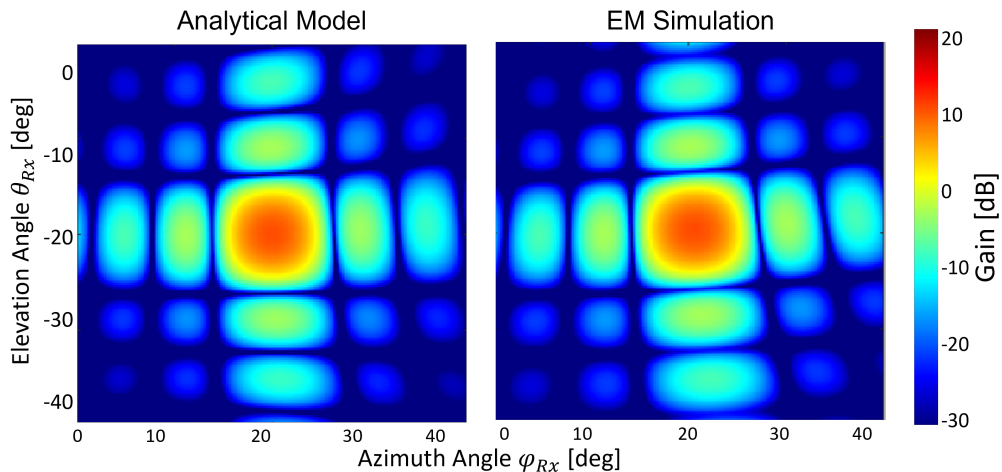


Figure 3.10: Sample RCS pattern of individual HELIOS module (1×1): (left) analytical model, (right) EM simulations for parameters $a = b = 10$ cm and $\alpha = \beta = 10^\circ$ at 38 GHz frequency with peak gain of 13.0 dB.

3.4 Analytical Model for Multi-Module HELIOS Reflectors

In this section, we now focus on HELIOS reflectors in the form of an array of HELIOS modules. Owing to this, our model from Sec. 3.3 is extended and subsequently reevaluated. An initial extension is carried out in Sec. 3.4.1, after which the accuracy model is thoroughly assessed by looking at three case studies. The discussion of self-shadowing issues that could surface between certain selected modules of a reflector's modules is then covered in Sec. 3.4.2, depending on how it is configured. This concentrated examination seeks to improve the accuracy of the analytical model that is introduced in this thesis, guaranteeing a thorough comprehension and improvement of its functions.

3.4.1 Independent Superposition of Overall Reflection Characteristics

The independent composition of overall reflection properties entails combining many separate HELIOS modules to realize fully-fledged reflectors or arbitrary characteristics. Thus, depending on a single, monolithic reflector, which has limitations, this modular approach provides a great degree of flexibility and adaptability. The established formula shown in Eq. (3.8) allows for the superposition of the individual RCS patterns of the HELIOS module, thereby providing a formula for the overall HELIOS reflector array. Whereas one could use the bistatic RCS pattern from Sec. 3.3, cf. Eq. (3.7), we propose a minor variation in the form of factors $M/2$ and $N/2$ (inside the sinc function) considering the overall number of modules along y - and z -axes, see Eq. (3.9).

The below equations describe the HELIOS reflector array as a whole, and it provides a baseline for comparing different configured models' RCS behavior. Notably, the beamwidth factor is influenced by the factors $M/2$ and $N/2$ in the equation. This parameter was successfully applied to a single HELIOS module with factors of $1/2$ each, see Eq. (3.7).

$$\sigma_{Array} = \left(\sum_{n=1}^N \sum_{m=1}^M \sqrt{\sigma_{module}(a_{m,n}, b_{m,n}, \alpha_{m,n}, \beta_{m,n})} \right)^2, \quad (3.8)$$

with

$$\begin{aligned} \sigma_{module} = & 4 \cdot \pi \cdot \Gamma \cdot \left(\frac{\left(a_{m,n} \sqrt{1 + \tan^2(\alpha_{m,n})} \right) \cdot \left(b_{m,n} \sqrt{1 + \tan^2(\beta_{m,n})} \right)}{\lambda} \right)^2 \\ & \left(\cos^2(\theta_{Tx} - \beta_{m,n}) \cdot \cos^2(\theta_{Rx} - \beta_{m,n}) \cdot \cos^2(\varphi_{Rx} - \alpha_{m,n}) \right) \\ & \left(\text{sinc}\left(\frac{M}{2} \cdot k \cdot b_{m,n} \sqrt{1 + \tan^2(\beta_{m,n})} \cdot (\sin(\theta_{Rx} - \beta_{m,n}) \cdot \cos(\varphi_{Rx} - \alpha_{m,n}) - \sin(\theta_{Tx} - \beta_{m,n}) \cdot \cos(\varphi_{Tx} - \alpha_{m,n}))\right)\right)^2 \\ & \left(\text{sinc}\left(\frac{N}{2} \cdot k \cdot a_{m,n} \sqrt{1 + \tan^2(\alpha_{m,n})} \cdot (\cos(\theta_{Rx} - \beta_{m,n}) \cdot \sin(\varphi_{Rx} - \alpha_{m,n}) - \cos(\theta_{Tx} - \beta_{m,n}) \cdot \sin(\varphi_{Tx} - \alpha_{m,n}))\right)\right)^2 \end{aligned} \quad (3.9)$$

Three in-depth case studies are conducted to validate this equation. In the first investigation, RCS patterns from various setups are compared. An ECDF comparison between the analytical model and EM simulation results of the HELIOS reflector array is carried out in the second study. The third study provides a comprehensive analysis of the equation's performance in various settings by examining various configurations and sensible beamwidth factors. Together, these case studies advance our understanding of the RCS behavior and the versatility of the equation in various reflector array configurations.

Case Study 1: RCS Pattern Comparison for Different HELIOS Configurations

For validation of Eq. (3.9), we study the peak RCS gains of different dimensions of HELIOS arrays in Fig. 3.11. In particular, we examined arrays with dimensions of $1 \times N$ and $M \times N$, where M and N are integers between 1 and 8. Whereas, there is already a noteworthy degree of consistency, there are nonetheless differences against the simulation results. For example, for the 1×8 array depicted on the left side, there is a difference of about 0.4 dB between the EM simulation results and our analytical model. If we consider the 8×8 array on the right side, the difference increases to a more noticeable 1.2 dB. As we show in Sec. 3.4.2, this is due to self-shadowing between the individual HELIOS modules.

A thorough bistatic RCS heatmap comparison for 2×2 , 4×4 , and 8×8 HELIOS reflectors arrays is carried out to analyze the various analytical and simulation findings, where we observe a match in the behavior, as shown in Fig. 3.12. Interestingly, a pattern emerges from the observations: both the simulative and analytical model beams show a notable narrowing effect with increasing gains as the reflector footprint grows.

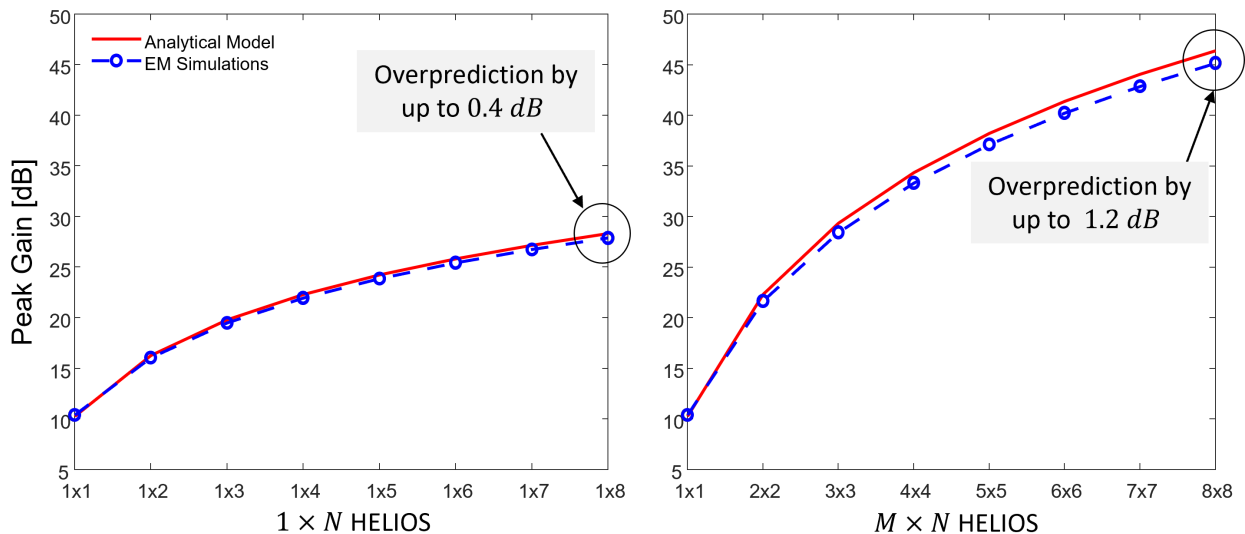


Figure 3.11: Plot against HELIOS array and maximum gain between simulated and analytical model highlighting the difference in gain in dB for the case when $\alpha_{m,n} = \beta_{m,n} = 10^\circ$ and $a_{m,n} = b_{m,n} = 10$ cm for $M = N \in [1 : 8]$ at 28 GHz frequency.

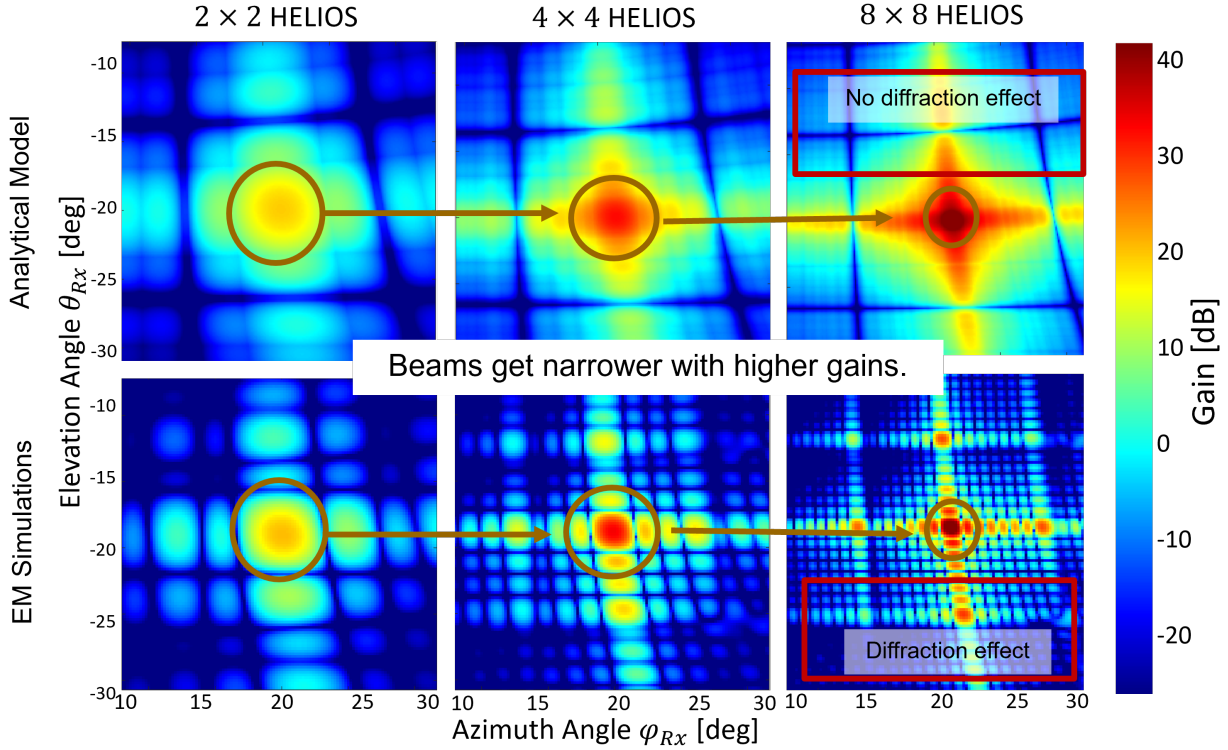


Figure 3.12: RCS pattern behavior of HELIOS reflectors with different number of modules for simulation and analytical model highlighting the similarities in gains and beam patterns without the consideration of diffraction effect for $\alpha_{m,n} = \beta_{m,n} = 10^\circ$ and $a_{m,n} = b_{m,n} = 10\text{ cm}$.

Extending our analysis beyond the main lobe, we observe a limitation of our analytical model: diffraction effects are not included in the analytical model by default, as we are so far considering the models independently. This aspect can be addressed by future work. In the later part of this section, we refer to Sec. 3.4.2 illustrates a similar fine-tuning of our model by considering inter-module shadowing effects.

Case Study 2: ECDF Comparison of Analytical Model and EM Simulation Results for HELIOS Reflector Array.

With an emphasis on both 2×2 and 8×8 HELIOS array configurations with $a_{m,n} = b_{m,n} = 10\text{ cm}$, Fig. 3.13 depicts the ECDFs along the realized RCS gains which focuses on the performance differences between analytical and simulated values. As annotated in the plot, the more to the right the overall distribution curve is, the better the performance in terms of exhibited reflection power for the whole range of φ_{Rx} and θ_{Rx} angles. The slope angles $\alpha_{m,n} = \beta_{m,n} = 10^\circ$ with incident angles $\theta_{Tx} = \varphi_{Tx} = 0^\circ$ at 28 GHz frequency.

Notably, for both types of HELIOS configurations, the simulation findings consistently show better performance than the analytical counterparts. Along the mean at 2×2 and 8×8 HELIOS array,

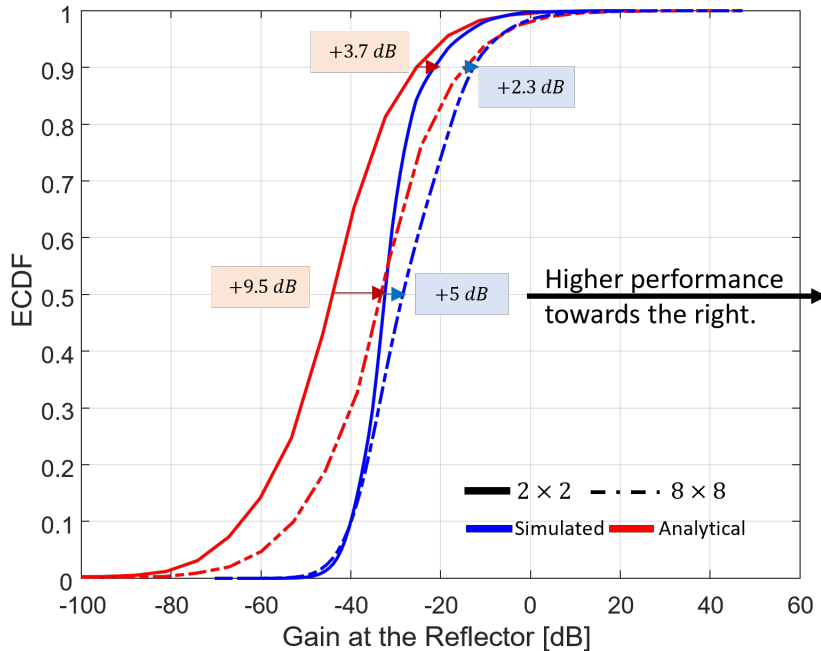


Figure 3.13: Gain vs ECDF plot for 2×2 and 8×8 HELIOS array with $a_{m,n} = b_{m,n} = 10$ cm for simulated and analytical results with a notable difference in gain between both the models when slope angles $\alpha_{m,n} = \beta_{m,n} = 10^\circ$ with incident angles $\theta_{Tx} = \varphi_{Tx} = 0^\circ$.

the simulated results are better than the analytical model by 9.5 dB and 5 dB than the analytical model, whereas along the 90% quartile, the simulated results are better by 3.7 dB and 2.3 dB, respectively. The fact that the gain values are constantly lower shows that the analytical model avoids over-prediction. This discrepancy between the analytical and simulation results indicates a cautious approach because it suggests a conservative estimate in the analytical model. In practical applications, this careful prediction ensures that the actual performance of the system is less likely to deviate from the expected values, hence improving the analytical model's robustness and reliability. Network planning will now rather use too many reflectors or larger ones compared to not meeting the required target received signal strengths.

Case Study 3: RCS Pattern Comparison for Different HELIOS Configurations and Beamwidth Factors

The scalability needed by larger HELIOS reflectors is not met by applying Eq. (3.7) in the 1×1 HELIOS module. To find an ideal solution for the bigger reflector designs, we investigate and evaluate various beamwidth correction factors in order to overcome this constraint. One important finding from our analysis of the beamwidth correction factor for a HELIOS module is seen in Eq. (3.7) and Tab. 3.3, where the correction factor is found to be $(\frac{1}{2}, \frac{1}{2})$ for a HELIOS module. But when you move to an array configuration, you see a significant difference. To investigate this, we carried out a thorough analysis comprising multiple parameters, as shown in Fig. 3.14 for a 4×4 array as well as a HELIOS module.

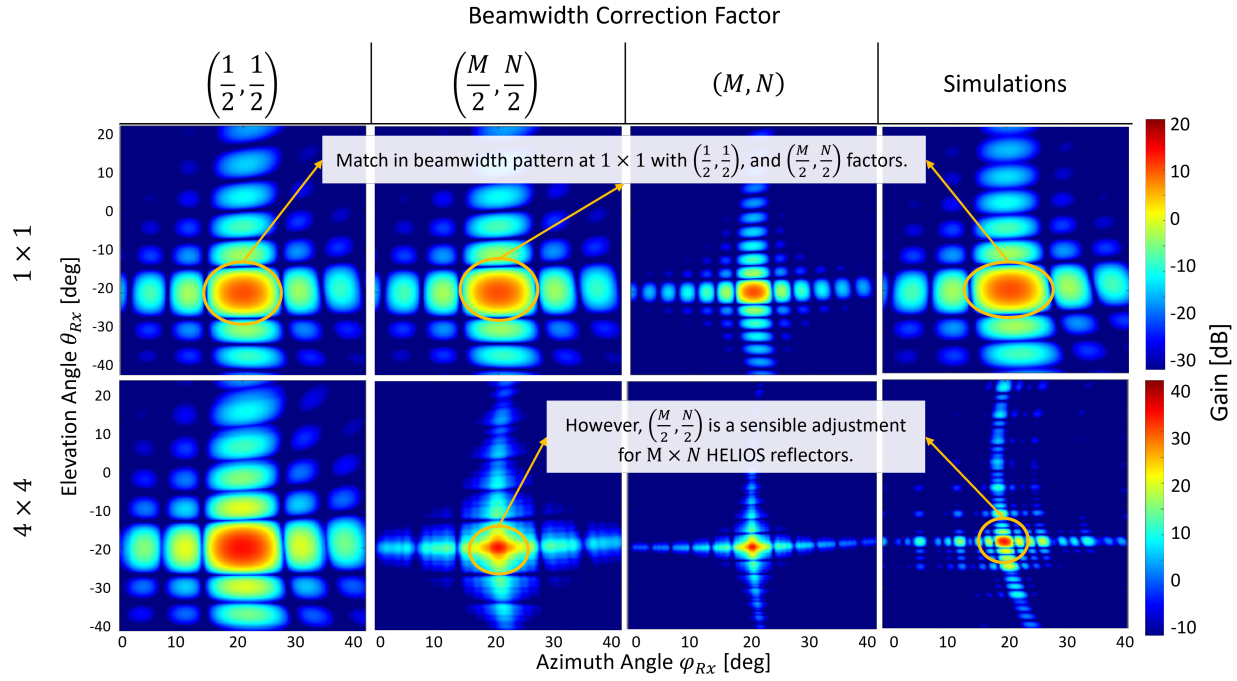


Figure 3.14: Illustrating the RCS behavior of a HELIOS module and HELIOS array for different beamwidth correction factors in comparison with the simulated results when $\alpha_{m,n} = \beta_{m,n} = 10^\circ$ and $a_{m,n} = b_{m,n} = 10$ cm for $M = N \in [1, 4]$.

Referring to Eq. (3.9), which is our final independent analytical model for the HELIOS reflector array, we vary $M/2$ and $N/2$ in both the sinc functions to change their beamwidth factor. These components include $(\frac{M}{2}, \frac{N}{2})$, (M, N) , in addition to the previously mentioned $(\frac{1}{2}, \frac{1}{2})$. For the 1×1 and 4×4 HELIOS reflector array with $\alpha_{m,n} = \beta_{m,n} = 10^\circ$, $a_{m,n} = b_{m,n} = 10$ cm, and $\theta_{Tx} = \varphi_{Tx} = 0^\circ$, we notice the RCS behavior in the form of heatmap in Fig. 3.14. The notable match is observed at $(\frac{M}{2}, \frac{N}{2})$ and $(\frac{1}{2}, \frac{1}{2})$ in the RCS heatmaps, but observing the behavior at 4×4 HELIOS reflector array, there's a sensible match at $(\frac{M}{2}, \frac{N}{2})$. We observe a better match in the results for larger arrays using $(\frac{M}{2}, \frac{N}{2})$ as the beamwidth correction factor.

In addition, we study a flat plate of fixed overall size by setting $\alpha_{m,n} = \beta_{m,n} = 0^\circ$ with the incident wave impinging from $\theta_{Tx} = \varphi_{Tx} = 0^\circ$. Like in the previous paragraph, we use the beamwidth correction factors of $(\frac{M}{2}, \frac{N}{2})$, (M, N) , in addition to the previously mentioned $(\frac{1}{2}, \frac{1}{2})$ from Eq. (3.7). This is because we consider the same flatplate in the form of two different representations: First, as a large 1×1 HELIOS reflector with dimensions $a = 40$ cm, and $b = 10$ cm. Second, the overall plate shall be represented by four modules in the form of a 1×4 HELIOS with individual modules having the dimensions of $a_{m,n} = b_{m,n} = 10$ cm. We compare the resulting overall bistatic RCS heatmaps in Fig. 3.15.

In the figure below, for 1×1 large flat plate, we observe the match in the RCS heatmap behavior with beamwidth factor $(\frac{1}{2}, \frac{1}{2})$, and $(\frac{M}{2}, \frac{N}{2})$, whereas, for 1×4 small flat plates, the match can be observed only with beamwidth factor $(\frac{M}{2}, \frac{N}{2})$. The same results were seen in Fig. 3.14, with $(\frac{M}{2}, \frac{N}{2})$ as the sensible adjustment of beamwidth factor for HELIOS reflector array.

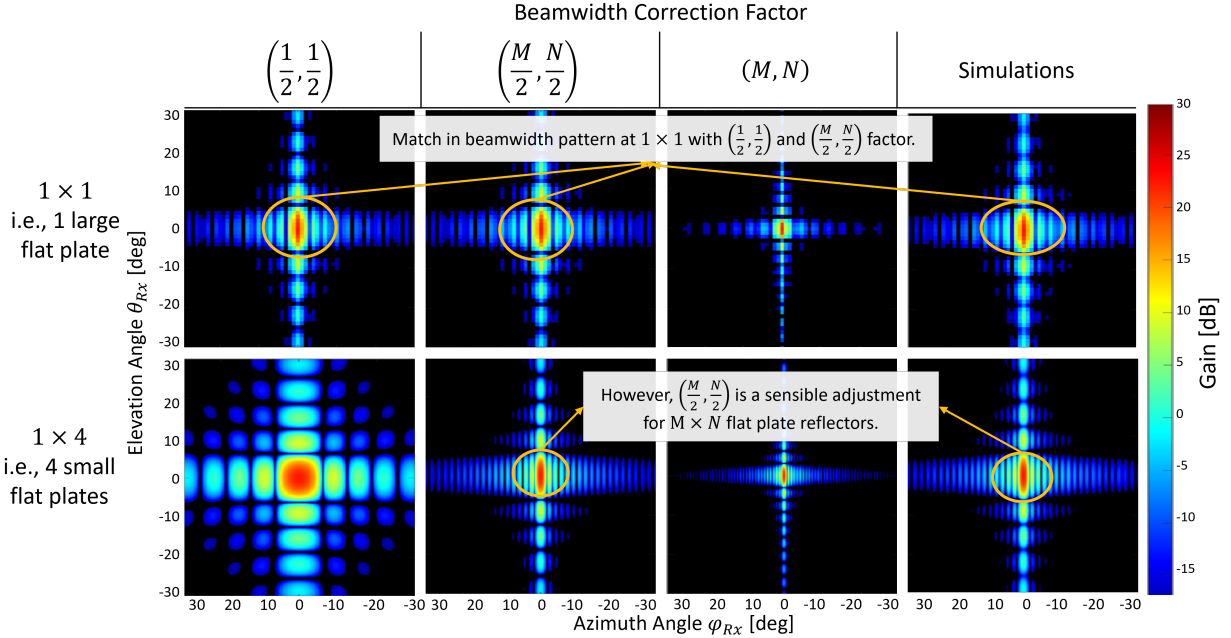


Figure 3.15: Illustrating the impact of different beamwidth correction factors in comparison with the simulations when $\alpha_{m,n} = \beta_{m,n} = 0^\circ$ for a single big flat plate with $a_{m,n} = 40$ cm, and $b_{m,n} = 10$ cm and multiple small flat plates with $a_{m,n} = b_{m,n} = 10$ cm, where both the cases 1×1 and 1×4 represent the same physical plate. Notably, with beamwidth factor of $(\frac{1}{2}, \frac{1}{2})$, and $(\frac{M}{2}, \frac{N}{2})$, there's a match with the simulations at 1×1 , but at 1×4 HELIOS reflectors, the match is observed with beamwidth factor $(\frac{M}{2}, \frac{N}{2})$.

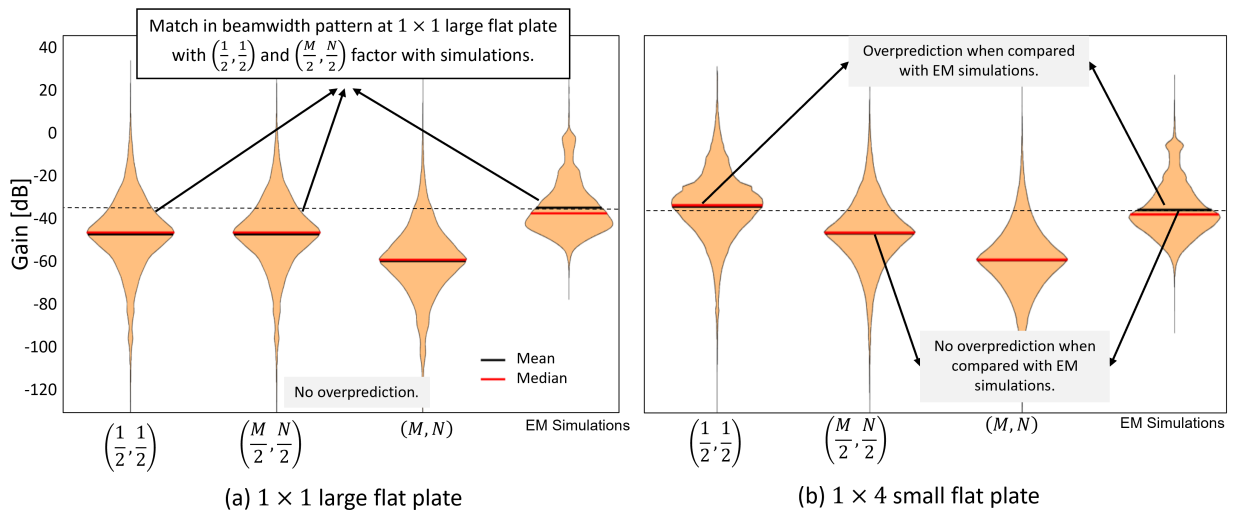


Figure 3.16: Violin plot comparison for a flat plate scenario for different beamwidth correction factors. (a) A single big flat plate with $a_{m,n} = 40$ cm, and $b_{m,n} = 10$ cm, and a notable match with EM simulations with beamwidth factor of $(\frac{1}{2}, \frac{1}{2})$, and $(\frac{M}{2}, \frac{N}{2})$ with no overpredictions. (b) 4 small flat plates with $a_{m,n} = b_{m,n} = 10$ cm and a match with the simulations with beamwidth factor $(\frac{M}{2}, \frac{N}{2})$ with no overpredictions. Both the cases 1×1 and 1×4 represent the same physical plate.

We also consider the above discussed RCS heatmaps in the form of violin plots, see Fig. 3.16. Notably, our analytical model regularly predicts slightly lower values, as evidenced by the mean and median values for beamwidth correction factors $(\frac{M}{2}, \frac{N}{2})$, and (M, N) falling below the corresponding simulation findings with both 1×1 large flat plate and 1×4 small flat plate. But when using the $(\frac{1}{2}, \frac{1}{2})$ correction factor, this disparity is not seen in 1×4 small flat plate, as the model overpredicts when compared with EM simulations. Significantly, this actual data supports the analytical model and points to one of its positive features: it predicts values that are slightly lower than those obtained from simulations with beamwidth factor $(\frac{M}{2}, \frac{N}{2})$, which is in line with our intended results as argued previously.

The focus of this extended study is now to compare our analytical model with the EM simulations for a 1×32 HELIOS reflector using different beamwidth correction factors. It is assumed that incidence angles are orthogonal to the backplane of the reflector, i.e., $\varphi_{Tx} = \theta_{Tx} = 0^\circ$ with slope angles $\alpha_1 = \dots \alpha_{32} = 27.6^\circ$ and $\beta_{m,n} = 0^\circ$. The overall size of the reflector shall be tuned by factor K affecting the size along y -axis and z -axis, respectively, as follows: $a_{m,n} = K \cdot \frac{3}{32}$ and $b_{m,n} = K \cdot 3$ with $K = (0.1, 0.3, 0.5, 0.7)$, where $a_{m,n}$ and $b_{m,n}$ are in m.

Fig. 3.17 provides a violin plots of $\Delta Gain$ (in dB) defined by $RCS_{Sim} - RCS_{Anal}$ in order to study the influence of reflector size and beamwidth correction factor on the accuracy of the model against the EM simulations. Notably, the analytical data produce mean and median values for beamwidth

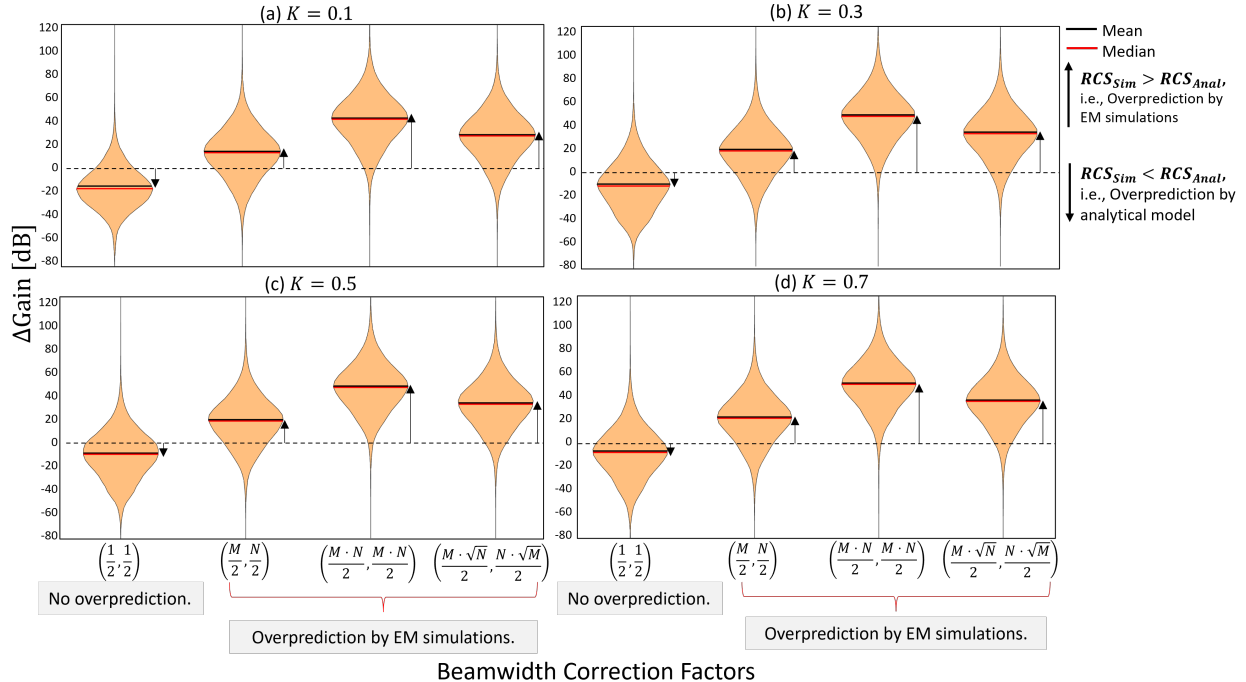


Figure 3.17: Violin plots illustrating the $\Delta Gain = RCS_{Sim} - RCS_{Anal}$ in dB for different beamwidth correction factors along the x -axis and varying HELIOS size scaling factors K along the four subfigures. Here, $\varphi_{Tx} = \theta_{Tx} = 0^\circ$, $\beta_1 = \dots = \beta_{32} = 0^\circ$, and $\alpha_1 = \dots \alpha_{32} = 27.6^\circ$.

factors $(\frac{1}{2}, \frac{1}{2})$ that are lower than those achieved from simulations, suggesting an overestimation as the mean values in all the four plots are less than zero. Whereas, our analytical model attains mean and median $\Delta Gain > 0$ dB values when using beamwidth correction factors of $(\frac{M}{2}, \frac{N}{2})$, and $(\frac{M-N}{2}, \frac{M+N}{2})$, thus suggesting little overprediction.

Assessing this along increasing K , we observe a gradual increase of the mean $\Delta Gain$ values, e.g., for $(\frac{1}{2}, \frac{1}{2})$ they are -18.3 dB, -14.6 dB, -11.2 dB and -7.4 dB. This shows that overprediction by the analytical model in the case with beamwidth factor $(\frac{1}{2}, \frac{1}{2})$ is reduced with increasing HELIOS size. The mean and median values with beamwidth factor $(\frac{M}{2}, \frac{N}{2})$ has values $\Delta Gain > 0$ dB, but less than that of other factors. Thus suggesting this beamwidth factor to be a sensible use for the HELIOS reflector array.

Additional Study: Comparative Results for Varying Reflector Size

We continue the above case study, however, now K is in range from $[0.1 : 3]$ m and we change our consideration to the one of a plat plate with $\alpha_{m,n} = \beta_{m,n} = 0^\circ$ for all $n \in 1, \dots, 32 = N$ ($m = 1$ due to linear array setup). We further explore the urban setting that was previously studied in this extended version, with particular emphasis on factors and assumptions pertaining to reflector properties. The underlying assumptions include an incident wave orthogonal to the reflector base $\varphi_{Tx} = \theta_{Tx} = 0^\circ$ and the prevalent usage of flat plate reflectors i.e., when $\alpha_{m,n} = \beta_{m,n} = 0^\circ$. A scaling factor K to determine the reflector size: $a_{m,n} = K \cdot \frac{3}{32}$, and $b_{m,n} = K$, where $K \forall [0.1 : 3]$ m. It is important to note that the total dimensions of the 32 reflectors preserve the equivalence $a_{m,n} = b_{m,n}$ for all K values.

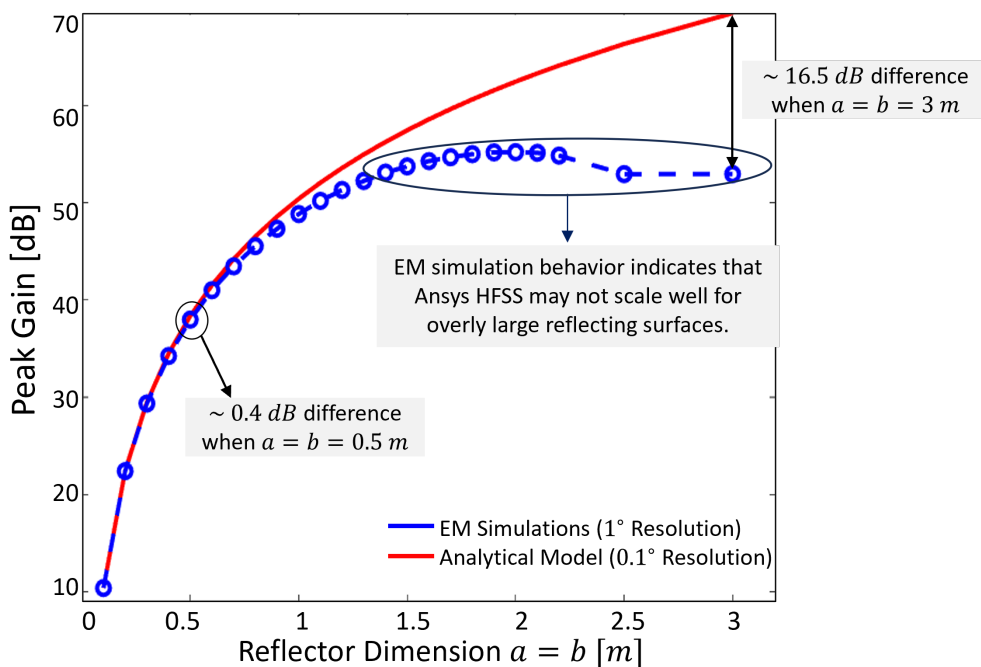


Figure 3.18: Comparing peak RCS value for $\varphi_{Rx}, \theta_{Rx} \in [-90, 90]^\circ$ range between analytical model and EM simulations along different reflecting surface size. Parameters: $\varphi_{Tx} = \theta_{Tx} = 0^\circ$, 1×32 HELIOS with $\alpha_{m,n} = \beta_{m,n} = 0^\circ \forall n \in 1, \dots, N$.

Fig. 3.18 shows the peak reflection gain of EM simulations and the analytical model for different reflector sizes. The simulations were carried out with 1° angular resolution, whereas our analytical model with 0.1° , thus, highlighting the speed and accuracy of our model. As expected, on one hand, we find that the peak gain grows with the reflector size, cf. Eq. (3.7). On the other hand, we observe a breakpoint in this behavior for the simulation-based result curve starting for $a_{m,n}, b_{m,n} > 0.5$ m, after which the peak gain reduces. But this is not the case with our analytical model, as the model scales with the increasing reflector size directly, see Eq. (3.7). Past this point, the models typically under estimate the rise in peak gain. For the reflector size $a_{m,n} = b_{m,n} = 0.5$ m, a notable difference of about 0.4 dB is observed between simulation results and our analytical model, whereas this difference increases to 16.5 dB for the reflector size $a_{m,n} = b_{m,n} = 3$ m.

Possible reasons for this discrepancy in the above figure by EM simulations might be reflector mismatches in their properties or a propensity for the simulation to overpredict when using bigger reflectors. It is important to recognize that situations involving huge reflector sizes may not be best handled by this particular Ansys HFSS simulation tool. In conclusion, this extended case study highlights that the findings underscore the need for examination of simulation accuracy, particularly when dealing with larger reflectors, and call for a nuanced understanding of the simulation tool's limitations in certain scenarios.

3.4.2 Improved Model Using Inter-module Relations

Lastly, we improve our analytical model that has been constructed successfully with the beamwidth correction factors of $(\frac{M}{2}, \frac{N}{2})$ in the arguments of the respective sinc functions, cf. Eq. (3.7) and Eq. (3.9). In the previous section, we identified that our analytical model does not yet address self-shadowing effects that may occur depending on the HELIOS configuration and the angles of arrival of the incident EM wave. To address this, we consider neighboring HELIOS modules in pairs, e.g., there are $N - 1$ pairs given N HELIOS modules along the y -axis. For each pair, we then assess whether the neighboring module particularly obstruct the incident wave such that the effective reflection area becomes smaller than accounted for so far. This way, we aim to address the overprediction of the RCS peak values against the EM simulation results, as obtained in Fig. 3.11.

First, we identify the shadowed fraction of the reflecting surface area along the reflector's edge based on incidence angles θ_{Tx} and φ_{Tx} . We split our consideration of this into two parts: one where the angles $\theta_{Tx} > 0^\circ$ and $\varphi_{Tx} > 0^\circ$, and the other where $\theta_{Tx} \leq 0^\circ$ and $\varphi_{Tx} \leq 0^\circ$. We first compute the extent of the shadowed zone along the y -axis by taking into account the module pairs' slope angles $\alpha_{m,n}, \alpha_{m,n+1}$, and φ_{Tx} , as illustrated in Fig. 3.19 for a 2×2 HELIOS reflector array. Likewise, we take into account $\beta_{m,n}, \beta_{m+1,n}$, and θ_{Tx} to determine the area that is shaded along the z -axis. As a result, η_a , and η_b summarizes the shadowing along the horizontal and vertical edges of module (m, n) from modules $(m, n + 1)$ and $(m + 1, n)$. For simplicity, we first consider the case of varying $\alpha_{m,n}$ values but with fixed $\beta_{m,n} = 0^\circ$ slopes.

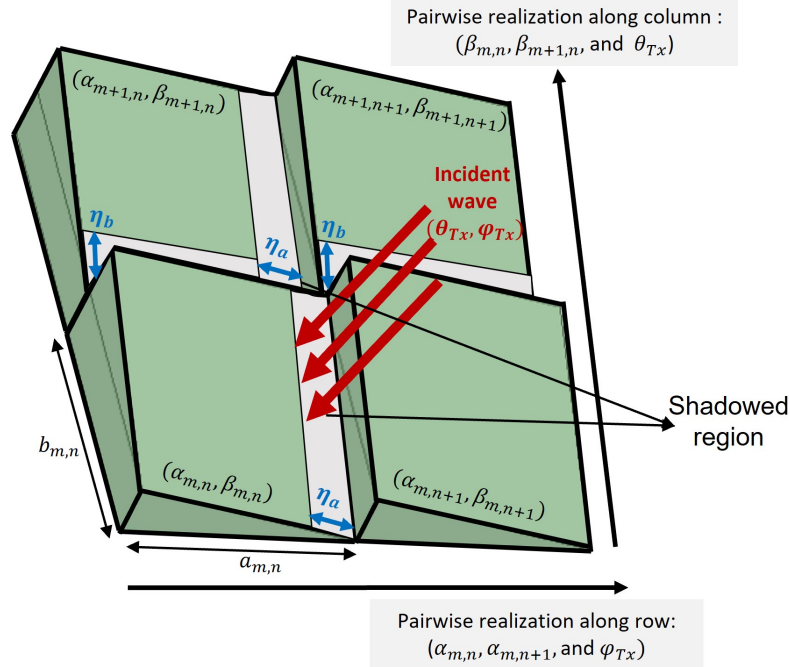


Figure 3.19: Pairwise realization of shadowing region η_a, η_b along y and z axis for incident wave $(\theta_{Tx}, \varphi_{Tx})$ along the edge for a sample HELIOS array of 2×2 along row and column.

As thus, four separate scenarios arise, as depicted in Fig. 3.20: In (a) Both the current and neighboring slope angles values are positive i.e., $\alpha_{m,n} > 0^\circ$ and $\alpha_{m,n+1} > 0^\circ$. (b) Both the current and neighboring slope angles values are negative i.e., $\alpha_{m,n} < 0^\circ$ and $\alpha_{m,n+1} < 0^\circ$. (c) The current slope angle $\alpha_{m,n} > 0^\circ$, and neighboring slope angles $\alpha_{m,n+1} < 0^\circ$. (d) The current slope angle $\alpha_{m,n} < 0^\circ$, and neighboring slope angles $\alpha_{m,n+1} > 0^\circ$.

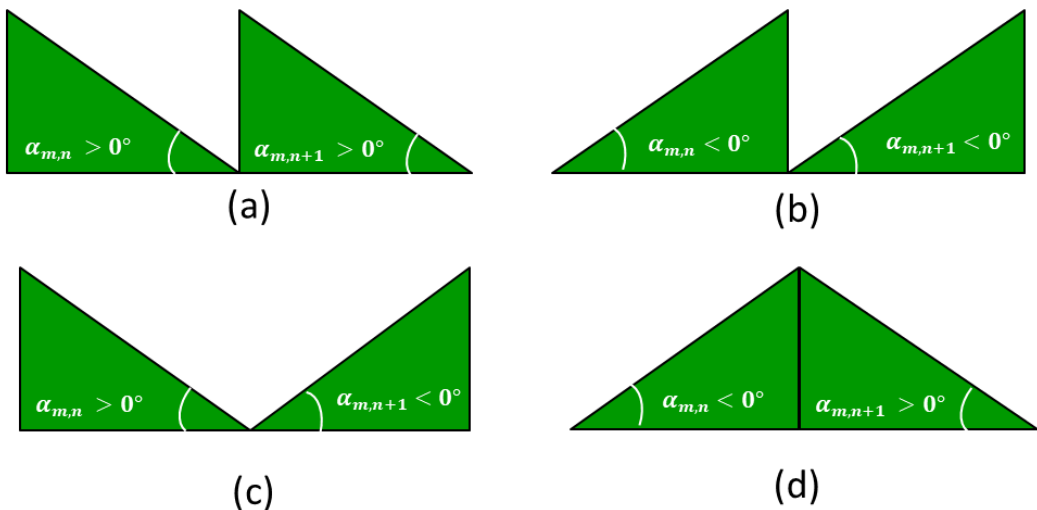


Figure 3.20: Different cases of pairwise realization for simple cases with current and neighboring slope angles $\alpha_{m,n}$, and $\alpha_{m,n+1}$. (a) Both positive slope angles (b) Both negative slope angles (c) Positive-negative slope angles (d) Negative-positive slope angles.

This thorough investigation establishes the foundation for deciphering the complex interaction of factors. The calculations of shadowing factors $\eta_{a_{m,n}}$, and $\eta_{b_{m,n}}$ take into account different incident angles cases, i.e., $\theta_{Tx} > 0^\circ$ and $\varphi_{Tx} > 0^\circ$ and also the case when $\theta_{Tx} \leq 0^\circ$ and $\varphi_{Tx} \leq 0^\circ$. To fully comprehend the behavior of the model under various settings, these varied scenarios, see Fig. 3.20 must be included. In particular, because of the way we approached pairwise realization, our tables in Tab. 3.4 and Tab. 3.5 include formulas for both reflectors, i.e., $\alpha_{m,n}, \alpha_{m,n+1}$ along the row and $\beta_{m,n}, \beta_{m+1,n}$ along the column. Fig. 3.21 considers the case for the incident angles $\theta_{Tx} = 0^\circ$, and $\varphi_{Tx} > 0^\circ$ and the slope angles $\alpha_{m,n}$, and $\alpha_{m,n+1}$ are positive with $a_{m,n}$ and $a_{m,n+1}$ being the dimension of current and neighboring model. The figure helps in the derivation of the shadowing factor $\eta_{a_{m,n}}$ for this particular case.

The shadowing factor $\eta_{a_{m,n}}$ from the figure can be derived using the law of sine in the blue shaded triangle. For this particular case, the equation follows as such:

$$\frac{\sin(\varphi_{Rx})}{\eta_{a_{m,n}}} = \frac{\sin(90^\circ - \varphi_{Rx} + \alpha_{m,n})}{h_{m,n+1}}, \quad (3.10)$$

where $h_{m,n+1}$ is the height of the neighboring reflector given by

$$h_{m,n+1} = a_{m,n+1} \cdot \tan(\alpha_{m,n+1}). \quad (3.11)$$

The shadowing factor $\eta_{a_{m,n}}$ can be extracted from Eq. (3.10) as

$$\eta_{a_{m,n}} = h_{m,n+1} \cdot \frac{\sin(\varphi_{Rx})}{\sin(90^\circ - \varphi_{Rx} + \alpha_{m,n})}. \quad (3.12)$$

Similarly, the derivation is considered for different cases in Fig. 3.20 and different incident angles. The derivation of shadow factor $\eta_{b_{m,n}}$ is carried out considering $\theta_{Tx}, \beta_{m,n}, \beta_{m+1,n}, b_{m,n}$, and $b_{m,n+1}$ when $\varphi_{Tx} = 0^\circ$.

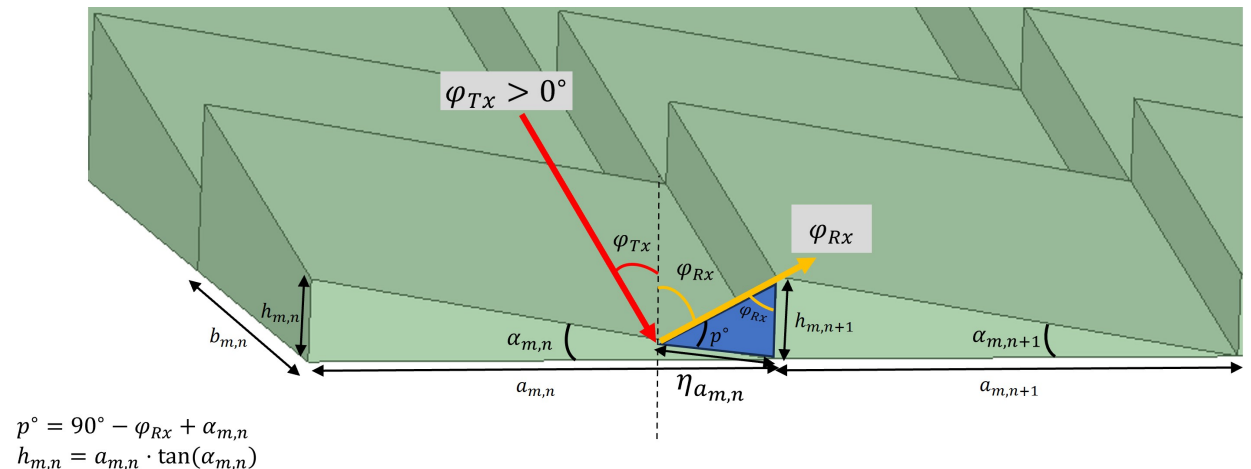


Figure 3.21: Depiction of the shadowing factor $\eta_{a_{m,n}}$ for the case when the incident angles $\theta_{Tx} = 0^\circ$, $\varphi_{Tx} > 0^\circ$ and the slope angles $\alpha_{m,n}$, and $\alpha_{m,n+1}$ are positive with $a_{m,n}$ and $a_{m,n+1}$. Here, $h_{m,n}$ and $h_{m,n+1}$ are the heights of the current and neighboring reflectors.

Using the shadowing factors $\eta_{a_{m,n}}$, and $\eta_{b_{m,n}}$ for the current and neighboring reflector with m and n indices, the Tab. 3.4 and Tab. 3.5 provides a detailed presentation of the obtained derived formulas for the shadowed region along the rows and columns, respectively.

We determine the effective reflecting surface size $a_{m,n}^* \times b_{m,n}^*$ as shown in Eq. (3.13) and Eq. (3.14).

$$a_{m,n}^* = (1 - \eta_{a_{m,n}}) \cdot a_{m,n} \quad (3.13)$$

$$b_{m,n}^* = (1 - \eta_{b_{m,n}}) \cdot b_{m,n} \quad (3.14)$$

Here, $\eta_{a_{m,n}}$ is for pairwise realization of model along the row, whereas $\eta_{b_{m,n}}$ is along the column.

Table 3.4: Shadowed region for the first reflector along the row and column for cases in Fig. 3.20.

Slope Angle	Incident	Shadowing Factor Formulae at the First Reflector
$\alpha_{m,n} > 0^\circ$ $\alpha_{m,n+1} > 0^\circ$ $\beta_{m,n} > 0^\circ$ $\beta_{m+1,n} > 0^\circ$	$\varphi_{Tx} > 0^\circ$ $\theta_{Tx} > 0^\circ$	$\eta_{a_{m,n}} = \frac{a_{m,n+1}}{a_{m,n}} \cdot \tan(\alpha_{m,n+1}) \cdot \frac{\sin(\varphi_{Tx})}{\cos(-\varphi_{Tx} + \alpha_{m,n})}, \varphi_{Tx} > 0^\circ$ $\eta_{b_{m,n}} = 0, \theta_{Tx} > 0^\circ$
	$\varphi_{Tx} \leq 0^\circ$ $\theta_{Tx} \leq 0^\circ$	$\eta_{a_{m,n}} = \begin{cases} \frac{a_{m,n+1}}{a_{m,n}} \cdot \tan(\alpha_{m,n+1}) \cdot \frac{\sin(-\varphi_{Tx} + 2 \cdot \alpha_{m,n+1})}{\cos(-\varphi_{Tx} + \alpha_{m,n} - 2 \cdot \alpha_{m,n+1})}, & \varphi_{Tx} > -90^\circ + \alpha_{m,n} \\ 1, & \varphi_{Tx} \leq -90^\circ + \alpha_{m,n} \end{cases}$ $\eta_{b_{m,n}} = \begin{cases} 0, & \theta_{Tx} > -90^\circ + \beta_{m+1,n} \\ 1, & \theta_{Tx} < -90^\circ + \beta_{m+1,n} \end{cases}$
	$\alpha_{m,n} < 0^\circ$ $\alpha_{m,n+1} < 0^\circ$ $\beta_{m,n} < 0^\circ$ $\beta_{m+1,n} < 0^\circ$	$\eta_{a_{m,n}} = \begin{cases} 0, & \varphi_{Tx} < 90^\circ + \alpha_{m,n} \\ 1, & \varphi_{Tx} > 90^\circ + \alpha_{m,n} \end{cases}$ $\eta_{b_{m,n}} = \begin{cases} \frac{b_{m+1,n}}{b_{m,n}} \cdot \tan(\beta_{m+1,n}) \cdot \frac{\sin(-\theta_{Tx} + 2 \cdot \beta_{m,n})}{\cos(-\theta_{Tx} - 2 \cdot \beta_{m,n} + \beta_{m+1,n})}, & \theta_{Tx} < 90^\circ + \beta_{m,n} \\ 1, & \theta_{Tx} > 90^\circ + \beta_{m,n} \end{cases}$
	$\varphi_{Tx} \leq 0^\circ$ $\theta_{Tx} \leq 0^\circ$	$\eta_{a_{m,n}} = 0, \varphi_{Tx} < 0^\circ$ $\eta_{b_{m,n}} = \frac{b_{m+1,n}}{b_{m,n}} \cdot \tan(\beta_{m+1,n}) \cdot \frac{\sin(\theta_{Tx})}{\cos(-\theta_{Tx} + \beta_{m,n})}, \theta_{Tx} < 0^\circ$
$\alpha_{m,n} > 0^\circ$ $\alpha_{m,n+1} < 0^\circ$ $\beta_{m,n} > 0^\circ$ $\beta_{m+1,n} < 0^\circ$	$\varphi_{Tx} > 0^\circ$ $\theta_{Tx} > 0^\circ$	$\eta_{a_{m,n}} = \begin{cases} 0, & \varphi_{Tx} < 90^\circ + \alpha_{m,n+1} \\ \frac{a_{m,n+1}}{a_{m,n}} \sqrt{1 + \tan^2(\alpha_{m,n+1})} \frac{\sin(\varphi_{Tx} + \alpha_{m,n+1} - 90^\circ)}{\cos(-\varphi_{Tx} + \alpha_{m,n})}, & \varphi_{Tx} > 90^\circ + \alpha_{m,n+1} \end{cases}$ $\eta_{b_{m,n}} = \begin{cases} 0, & \theta_{Tx} < 90^\circ + \beta_{m,n} \\ 1, & \theta_{Tx} > 90^\circ + \beta_{m,n} \end{cases}$
	$\varphi_{Tx} \leq 0^\circ$ $\theta_{Tx} \leq 0^\circ$	$\eta_{a_{m,n}} = \begin{cases} 0, & \varphi_{Tx} > -90^\circ + \alpha_{m,n} \\ 1, & \varphi_{Tx} < -90^\circ + \alpha_{m,n} \end{cases}$ $\eta_{b_{m,n}} = \begin{cases} 0, & \theta_{Tx} > -90^\circ + \beta_{m+1,n} \\ \frac{b_{m+1,n}}{b_{m,n}} \sqrt{1 + \tan^2(\beta_{m+1,n})} \frac{\sin(\theta_{Tx} + \beta_{m+1,n} - 90^\circ)}{\cos(-\theta_{Tx} + \beta_{m,n})}, & \theta_{Tx} < -90^\circ + \beta_{m+1,n} \end{cases}$
	$\alpha_{m,n} < 0^\circ$ $\alpha_{m,n+1} > 0^\circ$ $\beta_{m,n} < 0^\circ$ $\beta_{m+1,n} > 0^\circ$	$\eta_{a_{m,n}} = \begin{cases} 0, & \varphi_{Tx} < 90^\circ - \alpha_{m,n+1} \\ 1, & \varphi_{Tx} > 90^\circ - \alpha_{m,n+1} \end{cases}$ $\eta_{b_{m,n}} = 0, \theta_{Tx} > 0^\circ$
	$\varphi_{Tx} \leq 0^\circ$ $\theta_{Tx} \leq 0^\circ$	$\eta_{a_{m,n}} = 0, \varphi_{Tx} > 0^\circ$ $\eta_{b_{m,n}} = \begin{cases} 0, & \theta_{Tx} > -90^\circ + \beta_{m+1,n} \\ 1, & \theta_{Tx} < -90^\circ + \beta_{m+1,n} \end{cases}$

Table 3.5: Shadowed region for the second reflector along the row and column for cases in Fig. 3.20.

Slope Angle	Incident	Shadowing Factor Formulae at the Second Reflector
$\alpha_{m,n} > 0^\circ$ $\alpha_{m,n+1} > 0^\circ$ $\beta_{m,n} > 0^\circ$ $\beta_{m+1,n} > 0^\circ$	$\varphi_{Tx} > 0^\circ$ $\theta_{Tx} > 0^\circ$	$\eta_{a_{m,n+1}} = 0, \varphi_{Tx} > 0^\circ$ $\eta_{b_{m+1,n}} = \frac{b_{m,n}}{b_{m+1,n}} \cdot \tan(\beta_{m,n}) \cdot \frac{\sin(\theta_{Tx})}{\cos(-\theta_{Tx} + \beta_{m+1,n})}, \theta_{Tx} > 0^\circ$
	$\varphi_{Tx} \leq 0^\circ$ $\theta_{Tx} \leq 0^\circ$	$\eta_{a_{m,n+1}} = \begin{cases} \frac{a_{m,n}}{a_{m,n+1}} \cdot \tan(\alpha_{m,n}) \cdot \frac{\sin(-\varphi_{Tx} + 2 \cdot \alpha_{m,n})}{\cos(-\varphi_{Tx} - 2 \cdot \alpha_{m,n} + \alpha_{m,n+1})}, & \varphi_{Tx} < 90^\circ + \alpha_{m,n} \\ 1, & \varphi_{Tx} > 90^\circ + \alpha_{m,n} \end{cases}$ $\eta_{b_{m+1,n}} = \begin{cases} 0, & \theta_{Tx} < 90^\circ + \beta_{m+1,n} \\ 1, & \theta_{Tx} > 90^\circ + \beta_{m+1,n} \end{cases}$
	$\varphi_{Tx} > 0^\circ$ $\theta_{Tx} > 0^\circ$	$\eta_{a_{m,n+1}} = \frac{a_{m,n}}{a_{m,n+1}} \cdot \tan(\alpha_{m,n}) \cdot \frac{\sin(\varphi_{Tx})}{\cos(-\varphi_{Tx} + \alpha_{m,n+1})}, \varphi_{Tx} < 0^\circ$ $\eta_{b_{m+1,n}} = 0, \theta_{Tx} < 0^\circ$
	$\varphi_{Tx} \leq 0^\circ$ $\theta_{Tx} \leq 0^\circ$	$\eta_{a_{m,n+1}} = \begin{cases} 0, & \varphi_{Tx} < 90^\circ + \alpha_{m,n+1} \\ 1, & \varphi_{Tx} > 90^\circ + \alpha_{m,n+1} \end{cases}$ $\eta_{b_{m+1,n}} = \begin{cases} 0, & \theta_{Tx} < 90^\circ + \beta_{m,n} \\ \frac{b_{m,n}}{b_{m+1,n}} \cdot \sqrt{1 + \tan^2(\beta_{m,n})} \cdot \frac{\sin(\theta_{Tx} + \beta_{m,n} - 90^\circ)}{\cos(-\theta_{Tx} + \beta_{m+1,n})}, & \theta_{Tx} > 90^\circ + \beta_{m,n} \end{cases}$
$\alpha_{m,n} < 0^\circ$ $\alpha_{m,n+1} < 0^\circ$ $\beta_{m,n} < 0^\circ$ $\beta_{m+1,n} < 0^\circ$	$\varphi_{Tx} > 0^\circ$ $\theta_{Tx} > 0^\circ$	$\eta_{a_{m,n+1}} = \begin{cases} 0, & \varphi_{Tx} > -90^\circ + \alpha_{m,n} \\ 1, & \varphi_{Tx} < -90^\circ + \alpha_{m,n} \end{cases}$ $\eta_{b_{m+1,n}} = \begin{cases} \frac{b_{m,n}}{b_{m+1,n}} \cdot \tan(\beta_{m,n}) \cdot \frac{\sin(-\theta_{Tx} + 2 \cdot \beta_{m,n})}{\cos(-\theta_{Tx} + \beta_{m,n} - 2 \cdot \beta_{m+1,n})}, & \theta_{Tx} > -90^\circ + \beta_{m+1,n} \\ 1, & \theta_{Tx} < -90^\circ + \beta_{m+1,n} \end{cases}$
	$\varphi_{Tx} \leq 0^\circ$ $\theta_{Tx} \leq 0^\circ$	$\eta_{a_{m,n+1}} = \begin{cases} 0, & \varphi_{Tx} > -90^\circ + \alpha_{m,n} \\ \frac{a_{m,n}}{a_{m,n+1}} \cdot \sqrt{1 + \tan^2(\alpha_{m,n})} \cdot \frac{\sin(\varphi_{Tx} + \alpha_{m,n} - 90^\circ)}{\cos(-\varphi_{Tx} + \alpha_{m,n+1})}, & \varphi_{Tx} < -90^\circ + \alpha_{m,n} \end{cases}$ $\eta_{b_{m+1,n}} = \begin{cases} 0, & \theta_{Tx} > -90^\circ + \beta_{m+1,n} \\ 1, & \theta_{Tx} < -90^\circ + \beta_{m+1,n} \end{cases}$
	$\varphi_{Tx} > 0^\circ$ $\theta_{Tx} > 0^\circ$	$\eta_{a_{m,n+1}} = 0, \varphi_{Tx} > 0^\circ$ $\eta_{b_{m+1,n}} = \begin{cases} 0, & \theta_{Tx} < 90^\circ - \beta_{m,n} \\ 1, & \theta_{Tx} > 90^\circ - \beta_{m,n} \end{cases}$
	$\varphi_{Tx} \leq 0^\circ$ $\theta_{Tx} \leq 0^\circ$	$\eta_{a_{m,n+1}} = \begin{cases} 0, & \varphi_{Tx} > -90^\circ + \alpha_{m,n+1} \\ 1, & \varphi_{Tx} < -90^\circ + \alpha_{m,n+1} \end{cases}$ $\eta_{b_{m+1,n}} = 0, \theta_{Tx} > 0^\circ$

Our new methodology reveals an improved analytical model that exemplifies a clear dependency as described in Eq. (3.15).

$$\sigma_{Array} = \left(\sum_{n=1}^N \sum_{m=1}^M \sqrt{\sigma_{module}(a_{m,n}^*, b_{m,n}^*, \alpha_{m,n}, \beta_{m,n})} \right)^2 \quad (3.15)$$

To further explore the nuances of these scenarios, Fig. 3.22 depicts the shadowed region behavior of the two reflectors for incident azimuth angles $\varphi_{Tx} \in [-90 : 90]^\circ$ for the first case with positive slope angles of current and neighboring reflectors i.e., $\alpha_{m,n} = \alpha_{m,n+1} = 10^\circ$, where $a_{m,n} = b_{m,n} = 10\text{ cm}$, while $\beta_{m,n} = 0^\circ$, and $\theta_{Tx} = 0^\circ$, see Fig. 3.20.

When one looks at the peak gain plot in Fig. 3.23, the transformational impact of this integration is evident when compared to the peak gain plot in Fig. 3.11. After applying our modified model with the consideration of shadowed region $\eta_{a_{m,n}}$ and $\eta_{b_{m,n}}$, we achieved a significant improvement in the

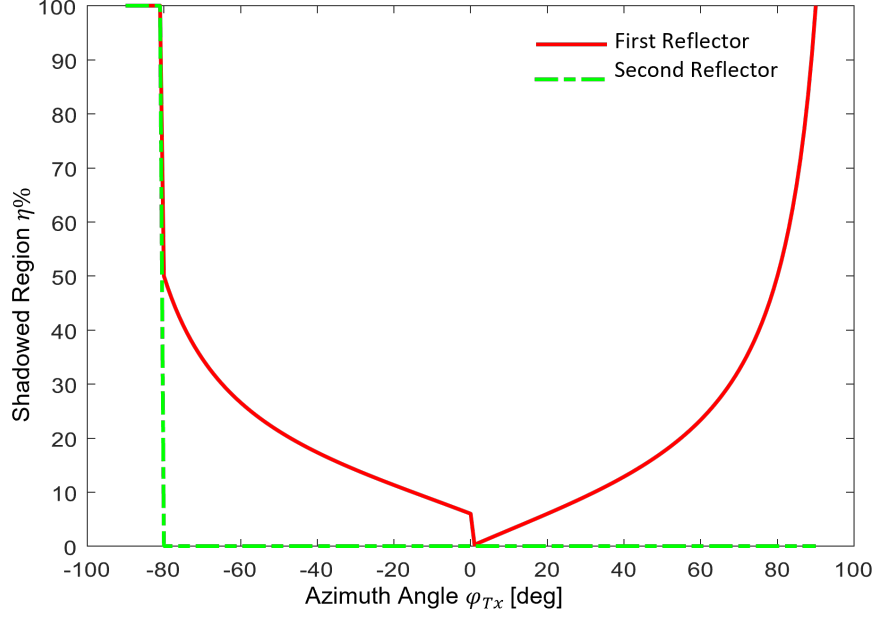


Figure 3.22: Plot depicting the amount of region shadowed for different incident azimuth angles $\varphi_{Tx} \in [-90 : 90]^\circ$ for simple case with $\alpha_{m,n} = \alpha_{m,n+1} = 10^\circ$ and $a_{m,n} = b_{m,n} = 10\text{ cm}$ while $\beta_{m,n} = 0^\circ$, and $\theta_{Tx} = 0^\circ$.

difference in peak gain between analytical and simulation models.

A noticeable difference of 0.02 dB is observed between analytical model and EM simulation results at 1×8 HELIOS reflector array when compared to the results in Fig. 3.11 with 0.4 dB. In similar manner, the difference of about 0.2 dB at 8×8 HELIOS reflector array is observed instead of 1.2 dB in Fig. 3.11. This shows how accurate our analytical model is by now.

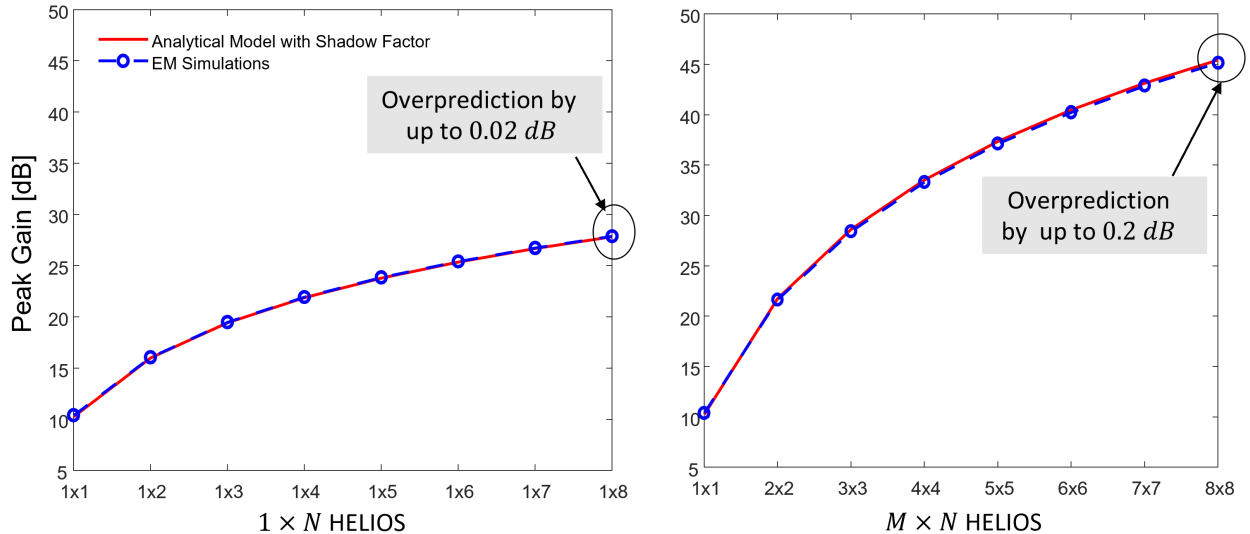


Figure 3.23: Plot against HELIOS array and maximum gain between simulated and analytical model after the elimination of the shadowed region, highlighting the difference in maximum gain in dB for the case when $a_{m,n} = b_{m,n} = 10\text{ cm}$ and $\alpha_{m,n} = \beta_{m,n} = 10^\circ$.

3.5 Summary

A brief overview of the prior section of Sec. 3.4 is given in this section. The basic formulas that make up our analytical model are contained in Eq. (3.7) for an individual HELIOS module and by Eq. (3.9) for an array of HELIOS reflectors. Sec. 3.4.2 improves our analytical model such that self-shadowing effects are accurately addressed. Important features are described, including the appearance of peak main lobe angles as determined by Eq. (3.1), and Eq. (3.2) and the beamwidth dependence of the module on dimensions M and N along the y and z axes, respectively. Sec. 3.3.4 showcases the reflection behavior along different frequencies showing that the gain at higher frequencies is higher, but due to a more narrow reflection one needs to take more measures if one still wants to fairly distribute the reflection along a wider range of angles. Our comprehension is further enhanced by a brief comparison with the equations governing in Sec. 2.3.3 showing the match between IRS and our analytical model.

The provided analytical model is actively used in Chapter 4 to forecast different communication channel features in various scenarios.

4 Performance Evaluation and Case Study

The main focus of this section is to assess our analytical model compared to simulations as well as against IRS models. We first examine computing time in detail in Sec. 4.1, in which we compare the analytical model with EM simulation results. An urban case study similar to the recent work [10] is presented in Sec. 4.2. Here, we first assess the baseline performance using the FSPL channel model before moving on to channel models that integrate three IRS models (cf. Sec. 2.3.3), and HELIOS (cf. Sec. 3.3). At last, we also produce few case studies to strengthen our study on the HELIOS analytical model.

4.1 Computing Time Analysis

The main goal of this section is to evaluate the computing efficiency between EM simulations using Ansys HFSS, see Sec. 3.1, and our analytical model using Mathworks MATLAB [10]. We note that the former is considered twice, one using 4, and the other with 128 CPU cores, respectively. When it comes to computing time, analytical models typically do better than simulations, which motivated the work. Naturally, the performance of the analytical model does depend on the programming language and implementation. Regardless, because simulations require large amounts of processing power and intricate algorithms, their execution times may be longer.

Fig. 4.1 provides a visual picture of our methodology and the ensuing data analysis. It shows the complete process, from HELIOS reflector parameterization, bistatic RCS calculation with different resolutions, computation, and computing time comparison. Based on this setup, we can assess the impact of this work's model against EM simulations. However, we note that other EM tools exist and could potentially provide the results with less computing time. Using more CPU cores or other models could also decrease the computing time. Similarly, the analytical model could in future be implemented in C/C++ for increase the computing time, too.

We use a Iron Python script that runs simulations with different $\alpha_{m,n}$, $\beta_{m,n}$, θ_{Tx} , and φ_{Tx} parameters to carry out our experiment, where we use the computing time generated, with the help of tic and toc functions, to compare with the EM simulations of different simulation cores and our analytical model. The measured computing times are saved and then evaluated in MATLAB. There, we executed and measured the computing time of the analytical model for the HELIOS reflector with the identical set of parameters of the EM simulations.

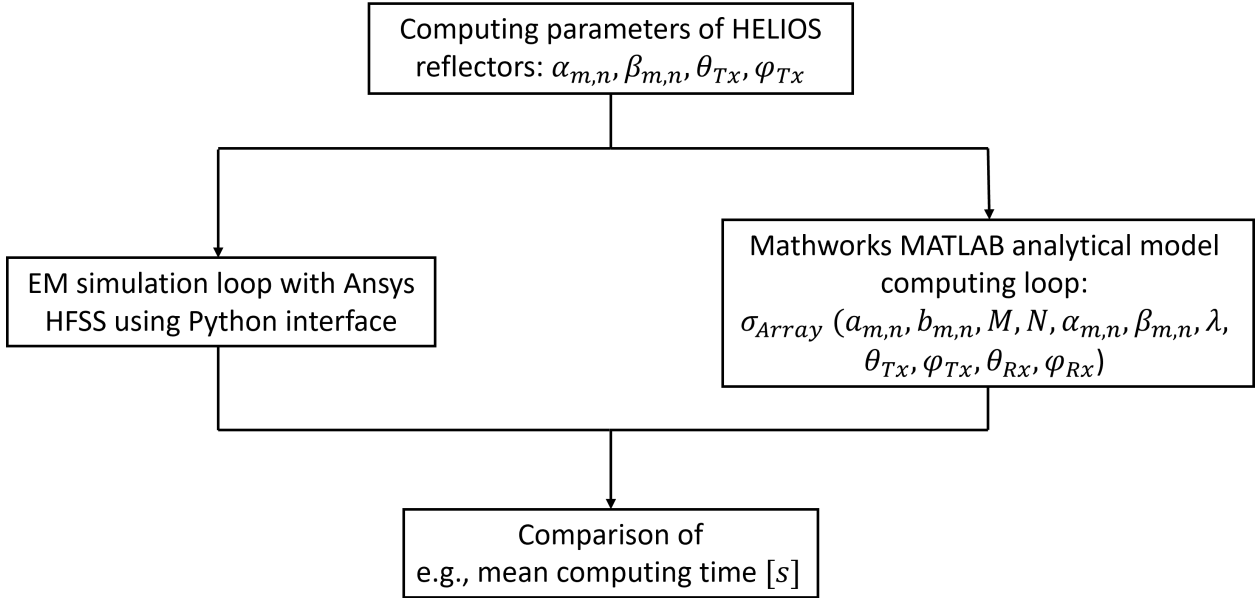


Figure 4.1: Methodological flowchart of this section's HELIOS computing time assessment comparing EM simulations and our analytical model for $m \in 1, \dots, M$, $n \in 1, \dots, N$.

Tab. 4.1 contains the mean computing time for a HELIOS module with $a_{m,n} = b_{m,n} = 10\text{ cm}$ and for two hundreds of these different combinations for the values in $\alpha_{m,n} \in [2 : 10]^\circ$, $\beta_{m,n} \in [2 : 10]^\circ$, $\theta_{Tx} \in [0 : 90]^\circ$, and $\varphi_{Tx} \in [0 : 90]^\circ$ in simulations. The values in the table is calculated for different angular resolutions. The bar graph representation of the same is given below in Fig. 4.2, where the x -axis consists of different angular resolutions for different processors as color coded in the figure and the y axis consists of mean computing time in s. We make use of the speed-up factor X , to measure the performance gain from multi-core processors. It is the ratio of execution times between various processor configurations.

Notable speed-up factors are revealed in Fig. 4.2, which offers insightful information, especially at a very high RCS resolution of 0.5° for which the mean computing time of simulations takes several hundred seconds. The measured speed-up factors of the analytical model to EM simulation of 128 core, analytical model to EM simulation of 4 core , and 128 to 4 core EM simulations are roughly 8,740, 14,681, and 2.2, respectively. This highlights the huge speed up of EM simulations by employing many CPU cores, on the one hand. On the other hand, however, simply switching to the analytical model massively outperforms this by reducing the computing time to just a fraction of a second, see Tab. 4.1.

Table 4.1: Mean computing time for a HELIOS module (1×1) with different angular resolutions of the bistatic RCS.

Angular Resolution	Analytical Model	EM Simulations (128 Core)	EM Simulations (4 Core)
2.0°	2.2 ms	14.9 s	32.3 s
1.0°	6.1 ms	34.8 s	106.3 s
0.5°	15.6 ms	117.45 s	400.4 s

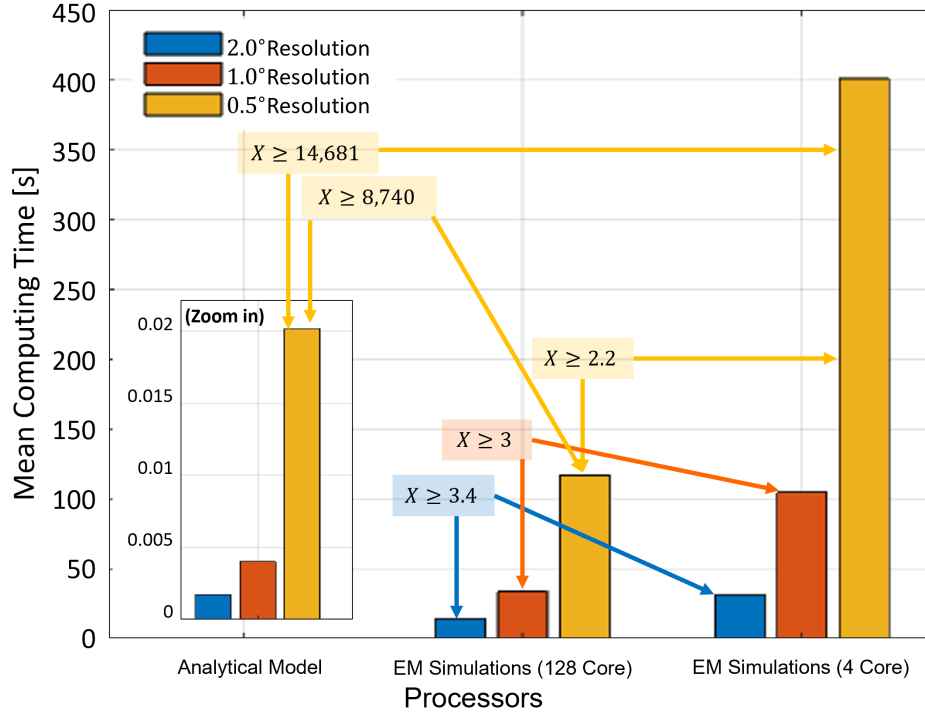


Figure 4.2: Mean computing time for a HELIOS module with different angular resolutions focusing on the speed-up factor X between different processors. Here, we find that the analytical model implementation is up to ca. 14,600 times faster than the EM simulations with 4 core and ca. 8,740 times faster than 128 core at 0.5° angular resolution.

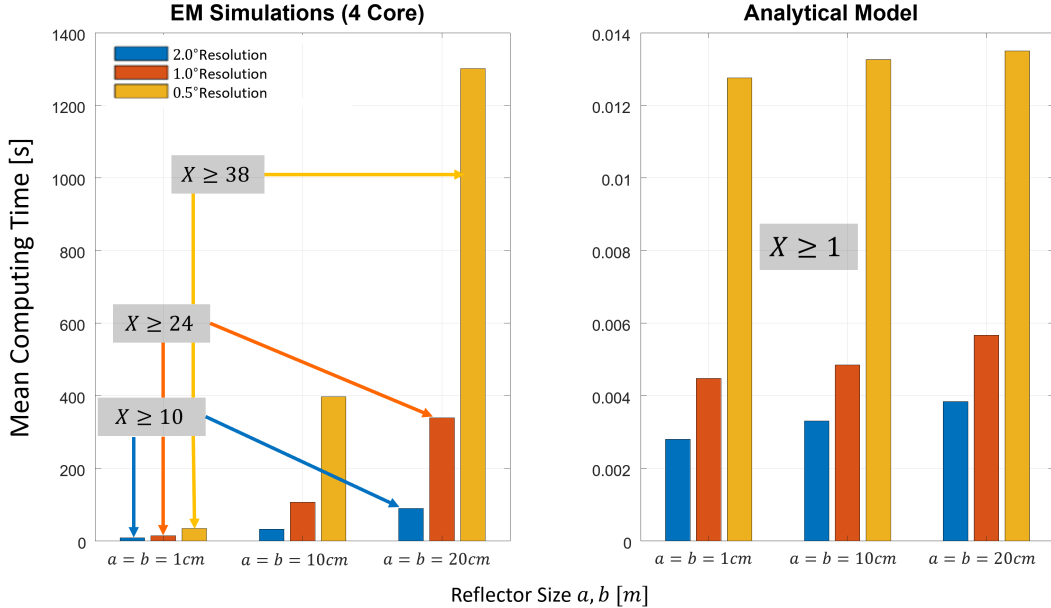


Figure 4.3: Mean computing time analysis for a HELIOS module (1×1) with varying angular resolutions highlighting the speed-up factors X between varying reflector sizes. Notably, as the reflector size increases, the mean computing time also increases in EM simulations with 4 core, but analytical model shows very little impact for varying sizes.

Table 4.2: Mean computing time for different angular resolutions depicting variations for varying reflector sizes for a HELIOS module. We observe that the analytical model's computing time is independent to the reflector dimensions whereas the EM simulations scale poorly, thus demonstrating infeasibility for large reflecting surfaces size as expected for 6G, cf. case study in Sec. 4.2.

HELIOS Module Dimensions	Angular Resolution	Analytical Model	EM Simulations (4 Core)
$a = b = 1 \text{ cm}$	2.0°	2.9 ms	8.4 s
	1.0°	4.5 ms	13.9 s
	0.5°	12.9 ms	33.8 s
$a = b = 10 \text{ cm}$	2.0°	3.4 ms	31.7 s
	1.0°	4.9 ms	106.3 s
	0.5°	13.3 ms	398.1 s
$a = b = 20 \text{ cm}$	2.0°	3.9 ms	89.6 s
	1.0°	5.8 ms	338.9 s
	0.5°	13.5 ms	1,309.3 s

As can be noted, the results in Tab. 4.1 corresponds to $a = b = 10 \text{ cm}$. Having considered the impact of the selected angular resolution of the RCS pattern, we move on to studying the impact of the reflector element size from $a = b = 1 \text{ cm}$ to $a = b = 20 \text{ cm}$ on the runtime. Similar to the previous paragraph, the results are provided below in Fig. 4.3 and Tab. 4.2 for different HELIOS module dimensions (1×1).

A clear pattern can be observed underlining that the computing time of the EM simulations increased in tandem with reflector size. A significant speedup factor is seen in the bar graph of the 4-core simulation as the reflector size increases from $a = b = 1 \text{ cm}$ to 20 cm . In particular, there is a speedup factor of about 38, 24, and 10 for 0.5° , 1° , and 2° resolutions, respectively. In contrast, we observe none of this for the analytical model, i.e., there is barely an impact on the computing time. Noticing from Tab. 4.2's mean computing time values for the analytical model, where very little effect regarding reflector size is observed, whereas, on the other hand, the values rise to $1,309.3 \text{ s}$ at 0.5° angular resolution with $a = b = 20 \text{ cm}$. These results highlight the efficiency benefits made possible by the analytical model in a variety of scenarios, highlighting its superiority when it comes to managing bigger reflector sizes when compared to the simulation method.

Table 4.3: Mean computing time for various HELIOS reflector array sizes (1×1 , 2×2 , and 4×4) with different angular resolutions. A notable performance of our analytical model in ms for an increase in reflector array demonstrates the advantage of the model to assess large-scale HELIOS configurations as compared to the simulation models. Parameters: $a_{m,n} = b_{m,n} = 10 \text{ cm}$.

HELIOS Reflector Array	Angular Resolution	Analytical Model	EM Simulations (128 Core)	EM Simulations (4 Core)
1×1	2.0°	1.6 ms	14.9 s	31.7 s
	1.0°	3.9 ms	33.5 s	106.4 s
2×2	2.0°	2.8 ms	20.6 s	77.9 s
	1.0°	11.2 ms	49.8 s	282.8 s
4×4	2.0°	9.9 ms	66.4 s	503.9 s
	1.0°	28.6 ms	197.7 s	1,574.6 s

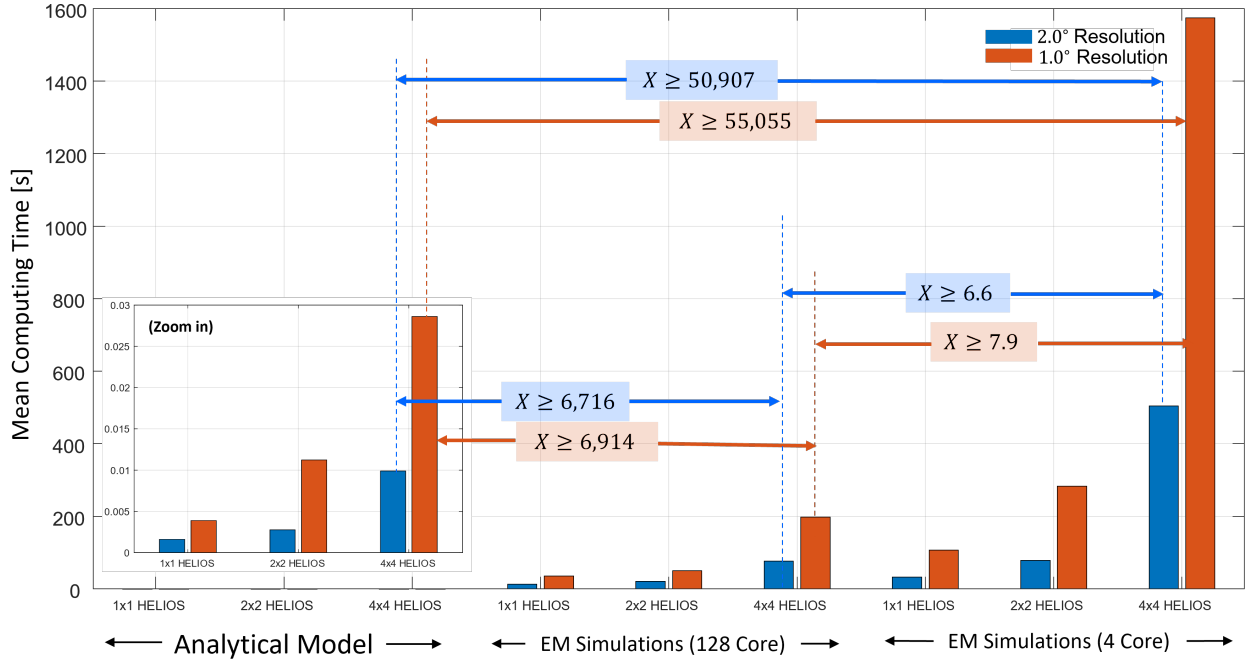


Figure 4.4: Mean computing time analysis for various HELIOS reflector array sizes ($1 \times 1, 2 \times 2$, and 4×4) highlighting the speed-up factor X between different angular resolutions. A notable faster performance by the analytical model is observed for the large-scale array configurations as compared to that of the simulation model.

Moving on, we now investigate the computing time dynamics for various array sizes (1×1 , 2×2 , and 4×4) using an analytical model and EM simulation of 4 core and 128 core configurations in our extended study. The mean calculation times for angular resolutions of RCS with 1° and 2° are given in Fig. 4.4, and Tab. 4.3.

Again, a similar pattern shows up for EM simulation architectures, indicating that computing time increases with array size. The measured speed-up factors at 1° resolution show that the transitions from analytical model to 128 core EM simulations, analytical model core to 4 core EM simulations, and 128 core to 4 core EM simulations appear as 6,914, 55,055, and 7.9, respectively. It is interesting to note that this trend becomes stronger with decreasing angular resolution, leading to higher speedup factors. As a result, our analytical model performs substantially faster than simulation models, especially when there are a lot of array models available. This divergence highlights the efficiency boost for engineers using our proposed analytical model instead of EM simulations to assess large-scale HELIOS configurations.

4.2 Urban Case Study

This section focuses on developing a deep comprehension of the urban scenario in Sec. 4.2.1 and forecasting various communication channel models in Sec. 4.2.2. By combining the analytical

model from Sec. 3.3 into practice in an urban setting, Sec. 4.2.4 and Sec. 4.2.5 we optimize the configurations and assess the performance gains over the results with the original configurations in Sec. 4.2.3. The incorporation of this refined model into the IRS models explained in Sec. 2.3.3 constitutes a fundamental component of our research, as seen in Sec. 4.2.6, where we also discuss two cases: beamformed to every possible position vs. one model which supports this fixed configuration similar to a passive reflector. A comparison study is carried out along with several case studies to thoroughly assess these models. Our investigation of the analytical model's effectiveness in actual urban communication situations is strengthened and expanded by these case studies. Lastly, in Sec. 4.2.8 we extend our study to explore different channel models and analyze the performance gain.

4.2.1 Urban Scenario Implementation

With this case study, we show how our HELIOS analytical model might be used in practice, for example in an urban environment, as shown in Fig. 4.5. The figure illustrates the location of the base station and clearly shows the distinction between Line-of-Sight (green-colored) and Non-Line-of-Sight (red-colored) zones. The two zones will be evaluated in Sec. 4.2.2. The judicious installation of a reflector on a nearby wall appears to be a good method to improve signal propagation and overcome potential obstructions in NLOS environments, as studied in Sec. 4.2.3 and Sec. 4.2.4.

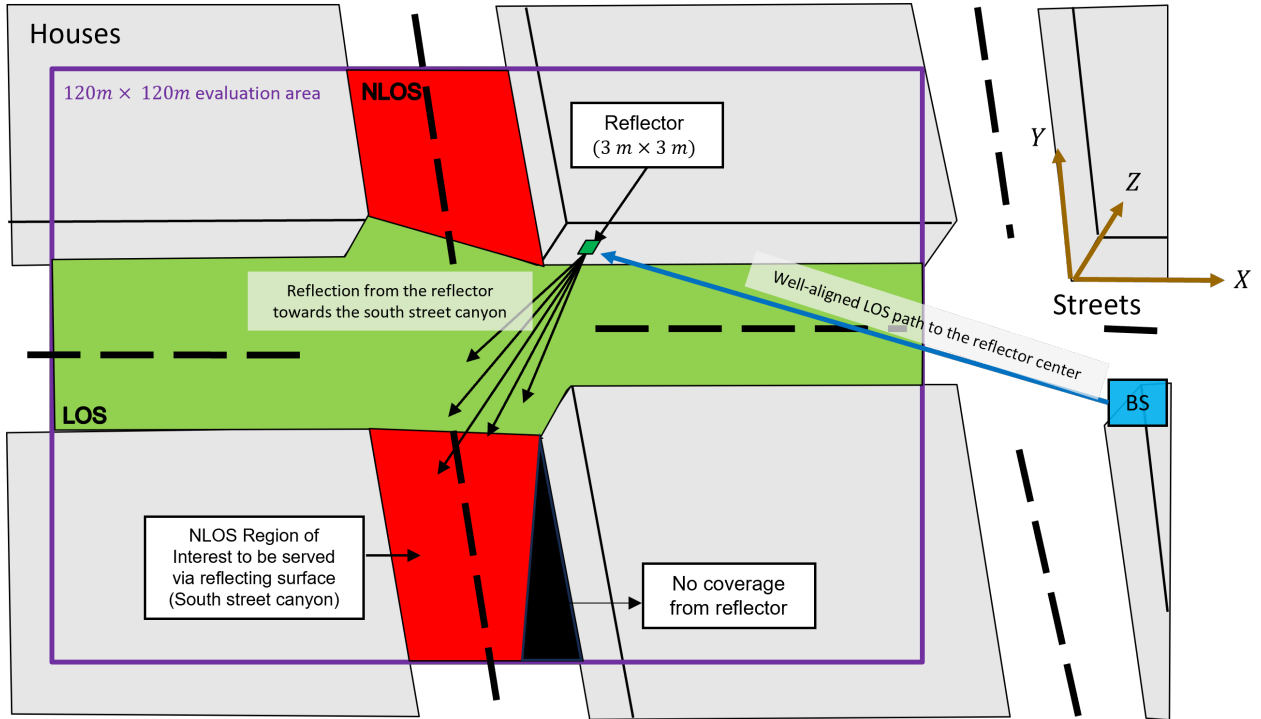


Figure 4.5: Illustration of urban scenario [10] with a well-aligned LOS path from the base station to the reflector center. The scenario highlights the reflections from the 3 m × 3 m reflector mounted on the building to serve the NLOS south street canyon region, as depicted.

Table 4.4: Key parameters and their values at transmitter, receiver, and the reflector applicable to the urban street corner scenario at 28 GHz frequency.

	Parameter	Values
P_{Tx}	Power transmitted	20.3 dBm
	G_{Tx}	19.7 dBi
	Position (x, y, z)	(309.9 m, 170.1 m, 10.0 m)
	$r_{Tx,Ref}$	115.0 m
	Beam orientations $(\varphi_{BS}, \theta_{BS})$	$(80.17^\circ, -2.46^\circ)$
Receiver	Antenna Gain	19.7 dBi
	Position grid center (x, y, z)	(309.9 m, 170.1 m, 10.0 m)
	Grid size x - z -plane	120.0 m \times 120.0 m
	Grid density	1.0 m
	$r_{Ref,Rx}$ range	[3.5: 102.6] m
	Receiver Sensitivity S_{Rx}	-83.5 dBm
	Angle Ranges towards street crossing/Reflector $(\varphi_{UE}, \theta_{UE})$	$\varphi_{Rx} : [-85.6^\circ : 87.3^\circ]$ and $\theta_{Rx} : [-87.1^\circ : 86.0^\circ]$
Reflector	Footprint size x - z -plane	3.0 m \times 3.0 m
	Reflector Array Configuration	1 \times 32
	Midpoint of Reflector Backplane (x, y, z)	(195.0 m, 170.0 m, 5.0 m)

By rerouting signals into our area of interest, i.e., south street canyon region, this reflective surface maximizes communication potential. Tab. 4.4 provides a detailed description of the scenario's particulars, which are identical to [10]. The base station, which uses 100 MHz of bandwidth and operates at a frequency of 28 GHz, is mounted on the corner of a large 100 m \times 100 m \times 20 m building complex at a height of 10 m. According to Tab. 4.4, the parameters φ_{BS} and θ_{BS} guide the orientation of the base station to precisely target the center of a designated 3 m \times 3 m mounting area for different reflectors under test, always mounted at a height of 5 m above ground. The scenario takes place at a street crossing, where the transmitted signal from the base station is in a well-aligned LOS path to the reflector center. In a grid with 1 m spacing, the receiver grid is uniformly positioned at a height of 1.5 m and stretches up to 60 m from the crossing point. Most notably, this simulation includes channels between the transmitter and thousands of potential receiver positions, offering a thorough grasp of the model's functionality in an actual metropolitan setting. One thing to notice in the example is that there is a black area that is not expected to be covered via the reflector. A case study in Sec. 4.2.5 will assess the impact of moving away from the reflector mounting position used in the paper [10].

After an initial assessment of the mmWave connectivity around the street crossing in Sec. 4.2, the connectivity gains of two HELIOS reflector deployments are considered in this section. Like in the original paper, a "narrow beam" HELIOS configuration with slope angles being constant, constitutes the first reflector deployment option. In contrast, the "broad beam" HELIOS configuration results from our exploration of a wider range of slope angles throughout the array. Both options are depicted in Fig. 4.6. The two cases are described as such:

- **Narrow beam HELIOS:** Slope $\alpha_1 = \dots = \alpha_{32} = 27.6^\circ$, and $\beta_1 = \dots = \beta_{32} = 0^\circ$.

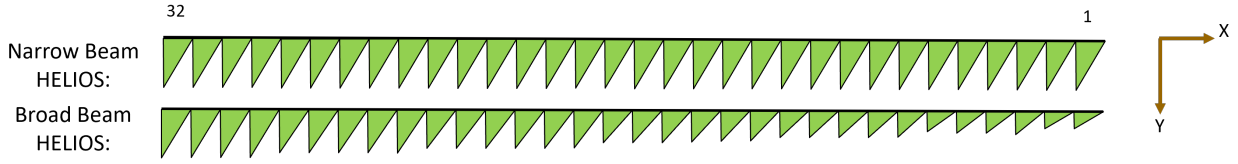


Figure 4.6: Top view illustration of original "narrow beam" and "broad beam" configuration for 1×32 HELIOS. We note that due to the symmetry of the original work, we adopt the flipped indices order.

- **Broad beam HELIOS:** Slope angle variation in steps of 2.5° with $\alpha_1, \dots, \alpha_{32} \in [17.6^\circ : 32.6^\circ]$, $\alpha_2, \alpha_1 = 17.6^\circ$, $\alpha_6, \dots, \alpha_3 = 20.1^\circ$, $\alpha_{11}, \dots, \alpha_7 = 22.6^\circ$, $\alpha_{17}, \dots, \alpha_{12} = 25.1^\circ$, $\alpha_{23}, \dots, \alpha_{18} = 27.6^\circ$, $\alpha_{28}, \dots, \alpha_{24} = 30.1^\circ$, and $\alpha_{32}, \dots, \alpha_{29} = 32.6^\circ$.
Similar to narrow beam reflector configuration $\beta_1 = \dots = \beta_{32} = 0^\circ$.

The visual summary of our methodology is presented in Fig. 4.7, which provides a top-view portrayal of the scenario that we are studying. The outage region, or regions where the reflectors are unable to provide coverage, is depicted in Fig. 4.7. As in Fig. 4.5, the buildings are represented by gray areas. Our main goal in this illustration is to cover the area such that the received power is greater than the designated receiver sensitivity threshold, i.e., as many potential UE positions in the south street canyon shall be able to connect to the network despite being in NLOS.

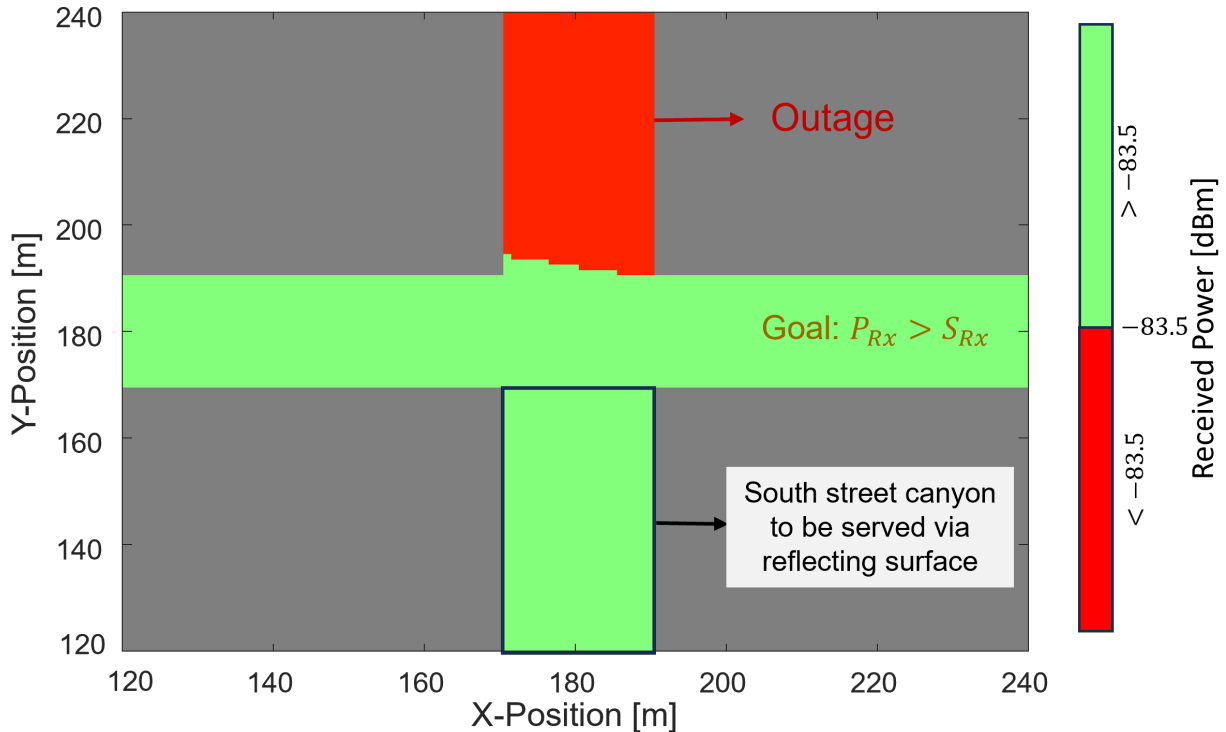


Figure 4.7: Sample illustration of received power analysis in the urban scenario to highlight the region of interest, i.e., south street canyon, where received power is greater than receiver sensitivity and the outage region.

4.2.2 Baseline Connectivity Using LOS Channel Models

Here we apply the FSPL model from Sec. 2.2.2 to estimate the received signal strength in the LOS regions of the selected scenario. We note that the NLOS regions will be assumed to have infinite path loss. After mounting of a reflecting surface, e.g., HELIOS or IRS, we also use the radar equation Eq. (3.9) to predict the receive power level at all UE positions, i.e., NLOS and LOS positions.

Eq. (4.2), which represents the excess path loss components that are then removed from the comprehensive path loss equation, explains the difference between the chained path loss equations, i.e., $PL_{Tx,Ref} \circ PL_{Ref,Rx}$ (see Eq. (4.1)). This equation provides a clear and concise illustration of the virtual LOS situation by directly representing the radar path.

$$PL_{FSPL_{Radar}}(r_{Tx,Ref}, r_{Ref,Rx}, f, \sigma_{Meta}, G_{Tx}, G_{Rx}) = PL_{FSPL}(G_{Tx}, r_{Tx,Ref}, f) + PL_{FSPL}(G_{Rx}, r_{Ref,Rx}, f) + \sigma_{Meta} - \Delta D_{ChainedFSPL}, \quad (4.1)$$

where

$$\Delta D_{ChainedFSPL} = 10 \cdot \log_{10}(4 \cdot \pi) - 20 \cdot \log_{10}(c) + 20 \cdot \log_{10}(f) \quad (4.2)$$

Eq. (4.2) is already incorporated in Eq. (2.5). Using this equation, we refer the reader to Fig. 4.8 for a brief comparison between the power level prediction for an arbitrary scenario assuming $\sigma_{Meta} = 0$ dB and the reflector location to be $r_{Tx,Ref} = 50$ m (see Sec. 3.3.1).

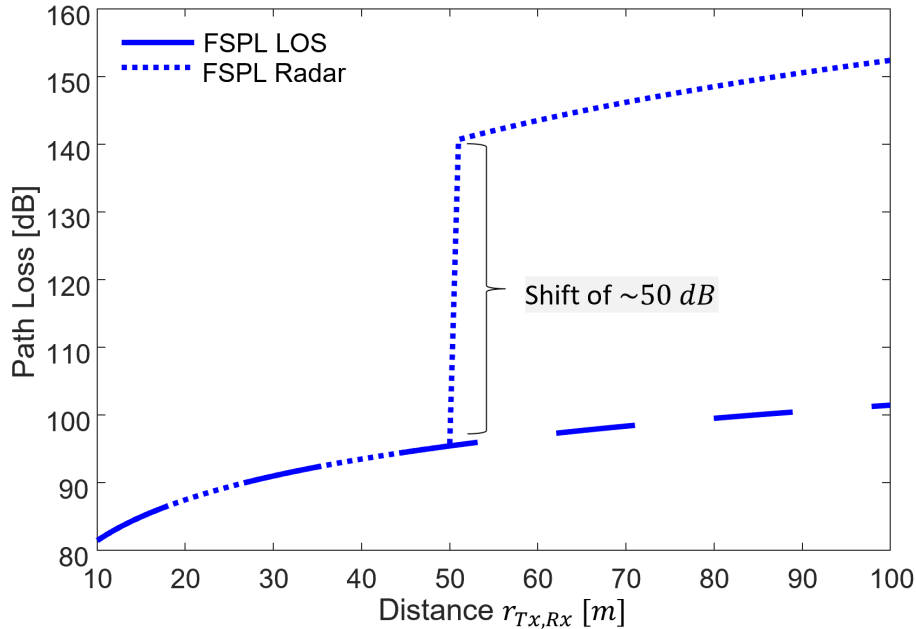


Figure 4.8: Comparison between predicted path loss of FSPL and radar equations over the total distance between Tx and Rx. For the radar equation curve, we assume LOS connectivity for the first 50 m. Thereafter, it holds $\sigma_{Meta} = 0$ dB, $r_{Tx,Ref} = 50$ m and $r_{Ref,Rx} = r_{Tx,Rx}$.

A notable shift of about 50 dB is observed at the reflector location $r_{Tx,Ref} = 50$ m. Referring back to Tab. 3.2, a car normally provides a σ_{Meta} value of about 20 dB. The observed shift at the reflector position is further reduced to about 30 dB when considered. Using geometries explicitly tailored to achieve high RCS, such as reflecting surfaces, particularly by scaling the reflecting surface area, such scenarios as considered in the context of Fig. 4.8 can be overcome such that a reflector path can provide virtual LOS connectivity.

4.2.3 Analyzing Connectivity Enhancement by HELIOS Reflectors

We now move on and assess the performance after mounting the narrow beam and broad beam HELIOS reflectors, respectively. For this purpose, we now put the radar equation to use, cf. Eq. (3.9). For σ_{Meta} , we either substitute our analytical model or the simulation results, see Fig. 4.9.

Initially, we verify the behavior of our analytical model through a comparison with simulation-based RCS patterns taken from [10]. Our results are illustrated visually in Fig. 4.9, which includes heatmaps for both narrow and broad beams. The heatmaps, in particular, highlight that the coordinates $(\theta_{Rx}, \varphi_{Rx}) = (-2.5^\circ, -25.75^\circ)$ are where the highest peak occurs and are in match.

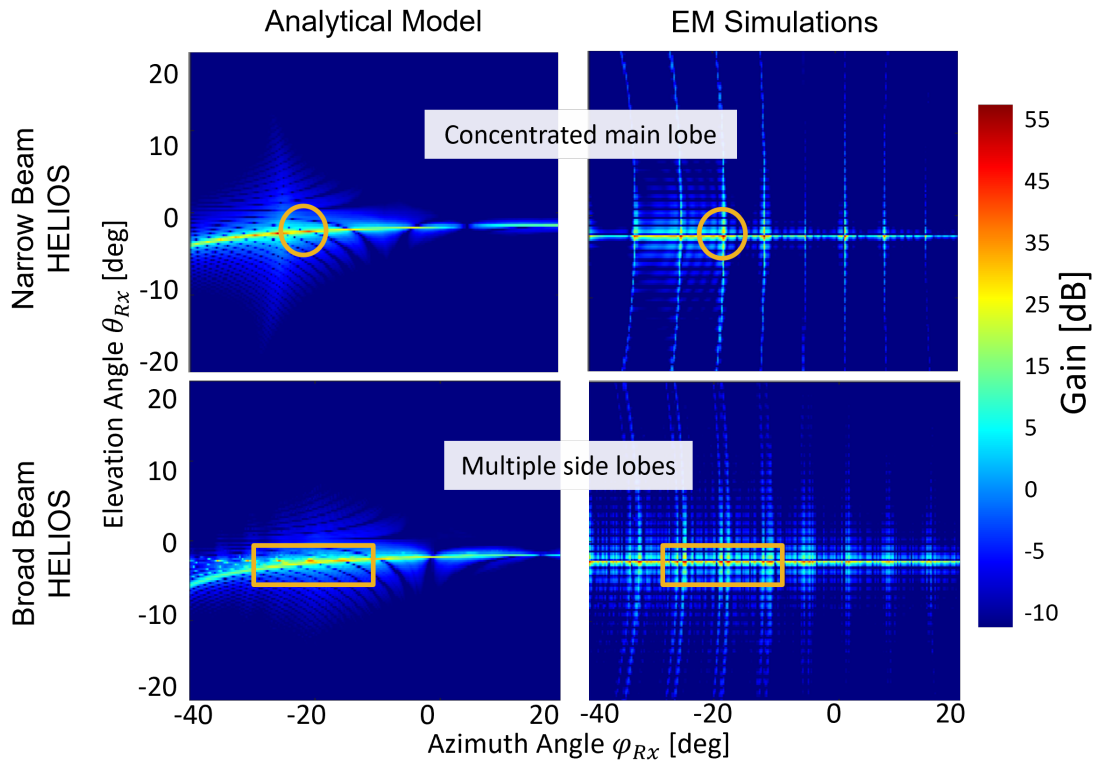


Figure 4.9: RCS comparison heatmaps between the HELIOS analytical model and EM simulation results in urban scenarios highlighting the gain behavior for both narrow and broad beams. Notably, a concentrated single lobe appears in narrow beam HELIOS, as the beams are focused in one direction at $(\theta_{Rx}, \varphi_{Rx}) = (-2.5^\circ, -25.75^\circ)$, whereas with broad beam HELIOS, we observe multiple side lobes.

The narrow beam HELIOS yields a peak gain of 54.6 dB with EM simulations, whereas 52.9 dB with the analytical model. Since it closely matches the simulated results, this consistency highlights the precision and dependability of our analytical method. As with broad beam HELIOS, our analytical model records a peak gain of 40.7 dB, whereas the simulation model records a little higher value of 48.7 dB. The overall trend shows an agreement between our analytical predictions and the simulated results, despite subtle differences in the magnitudes at the above-discussed angles. Since it faithfully reflects the simulation's observations of the larger beams' performance characteristics, this parallelism adds even more support to the validity of our analytical model.

Complementing the previous paragraph, we take a look at Fig. 4.10 depicting the ECDFs of the previously discussed RCS heatmaps. They underline that there is a fundamental match, e.g., in terms of mean value: For the narrow beam configuration, the mean gain difference is 2.8 dB with the analytical model predicting less reflection power than the EM simulations. This difference increases up to 9.7 dB for the broad beam HELIOS. Whereas this suffices that the analytical model does not overpredict, we note that the ECDFs are not always weaker than the ones of the simulations. However, this shows that overprediction is rare. Like our investigation in Sec. 3.3, this suggests that our analytical model provides a conservative estimate, even when scaling the reflecting surface to such large dimensions which potentially pushes analytical models and EM simulation tools to the limit.

In this section, we assess the impact on the received power for UEs located in the far-field region of the reflector under test. To make this transparent in our result figure, we highlight the near-field zone [60, 61], as defined by Eq. (4.3) below, as a white color coding.

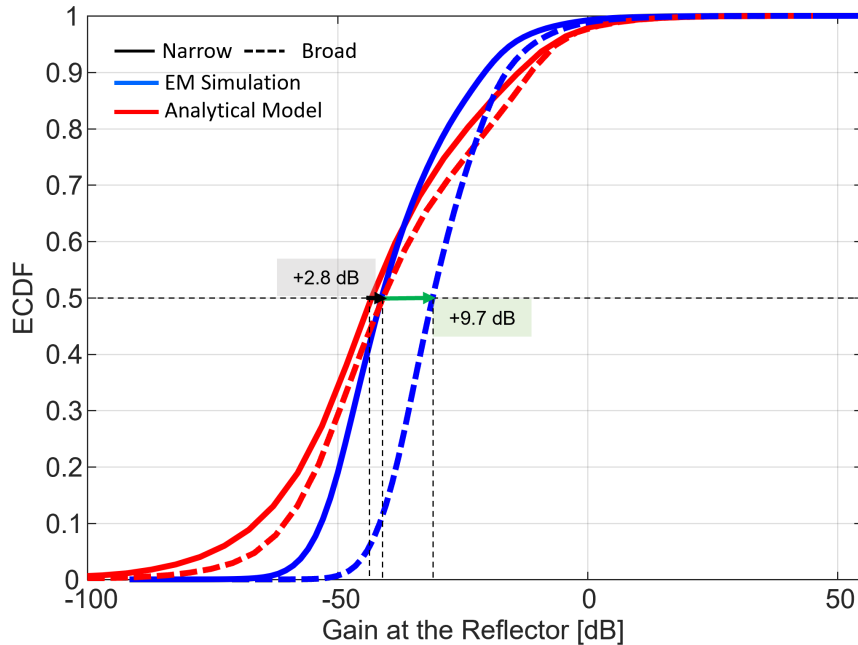


Figure 4.10: ECDF vs gain at the reflector plot for narrow and broad beam HELIOS highlighting the difference along the mean between simulated results and analytical model in dB. The parameters are considered from Tab. 4.4 at 28 GHz frequency.

Given $M \cdot a = N \cdot b = 3 \text{ m}$, the near-field region extends up to 8.4 m in this case study.

$$r_{Ref,Rx} \leq \frac{\max((M \cdot a)^2, (N \cdot b)^2)}{\lambda} \quad (4.3)$$

By integrating the HELIOS analytical model into our urban environment, we can predict the RCS towards each potential UE position and therefore also determine the expected receive power level. These heatmaps in Fig. 4.11 show the maximum power received which is expressed in dBm and the RCS gain which is measured in dB from the reflector into the receiver grid. The method for calculation of maximum power received is given by $P_{Rx_{Max}} = \max(P_{Rx_{LOS}}, P_{Rx_{Radar}})$, where the maximum power received with LOS and radar channel modeling is considered.

From the figure below, narrow beam HELIOS gives a peak gain of about 15.4 dB, whereas 11.2 dB with broad beam HELIOS. It appears from the figure that power is radiating in the direction of the south street canyon. It is interesting to note, nevertheless, that radiation in the LOS area seems to have very little effect. This observation is ascribed to the shortcomings of the maximum Received Signal Strength (RSS) statistic alone, as well as the complexities of the HELIOS design.

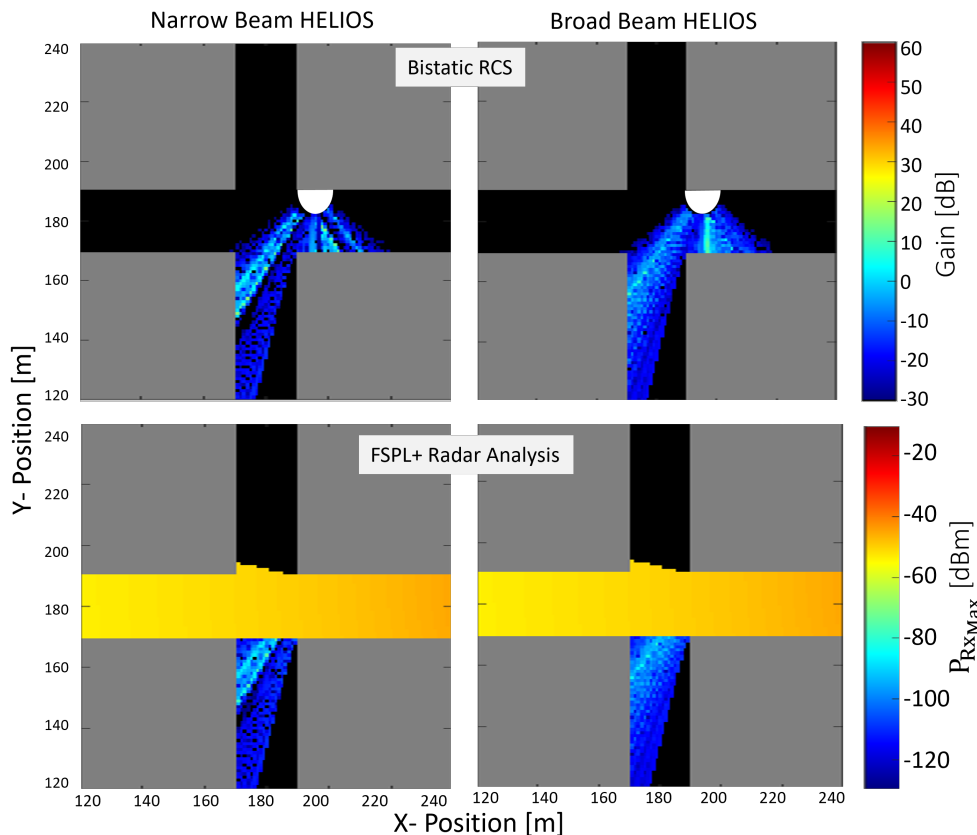


Figure 4.11: RCS comparison of narrow beam HELIOS (left column) and broad beams HELIOS (right column) in an urban scenario depicting the gain in dB (top row) and maximum power received in dBm (bottom row). The parameters are considered from Tab. 4.4 at 28 GHz frequency. Notably, the power is radiating in the direction of south street canyon with a peak gain of 15.4 dB with narrow beam and 11.2 dB with broad beam.

Even if the LOS zones appear to be unaffected, Fig. 4.7 confirms that the reflector, which has a minimum power $> -83.5 \text{ dBm}$, introduces unique propagation characteristics in the LOS region. Observing the behavior in the south street canyon, there is a significant difference in coverage regions between narrow and broad beams HELIOS. The heatmap's visual depiction of signal coverage fluctuations shows how tight beams have concentrated, localized effects while broad beam HELIOS has a broader range of influence. This finding highlights the tactical benefit of using a HELIOS configuration aiming for a broader distribution of the reflection. However, the overall coverage in south street canyon is noted to be around 1% with both narrow and broad beam HELIOS. A closer look at the RCS heatmaps at the bottom shows where the maximum power received is distributed. They are mainly in the LOS region and not in the region of interest, thus motivating a revision of the HELIOS configurations being considered in the next sections.

4.2.4 Optimizing Connectivity by Improving upon HELIOS Geometry

We used previously determined slope angle values from the literature [10] in our earlier analysis. Now, we use our analytical model systematically to identify a suitable HELIOS configuration so that our connectivity goals are met. Whereas such an optimization topic is out of the scope of this work, we show here how our analytical model can be put to use there due to the short computing times, see Sec. 4.1. We note that this would not be possible in such short time when using EM simulations. We investigated widely for slope angles $\alpha_{m,n}$, and $\beta_{m,n}$ to accomplish this optimization. With a 0.2° step size, the slope angle ranges from $\alpha_{m,n} \in [15 : 35]^\circ$ and $\beta_{m,n} \in [-10 : 10]^\circ$. Overall, more than 10,000 RCS pattern calculations were used to identify a more suitable HELIOS narrow beam and broad beam configuration, respectively.

It is important to remember that for narrow beams, the slope angle values for each of the 32 reflector parts stay constant, whereas, on the other hand, the slope angles must differ for broad beams. As such, there are two degrees of freedom to optimize the narrow beam HELIOS reflector configuration, i.e., $\alpha = \alpha_1 = \dots = \alpha_{32}$ and $\beta = \beta_1 = \dots = \beta_{32}$. For the revision of the broad beam HELIOS, we configure these variables precisely in our reflector design process. Our approach necessitates that each of the 32 modules have its slope angles carefully assigned inside the reflector design. With a step increment of 2.5° between each angle for both the slope angles, each module is specifically assigned one of seven different slope angles. This complex operation is as complex as described in the literature [10], and adjusting this step value has not been shown to result in meaningful improvements.

The RCS heatmap depicting our search for a narrow beam HELIOS inside our chosen region of interest is shown in Fig. 4.12. Here, each pixel in the heatmap is already the sum of the received power of the given HELIOS configuration. Finding the peak power received location, which acts as our reference point, is our main goal. We find the matching slope angles $\alpha_{m,n}$ and $\beta_{m,n}$ by locating the maximum value inside the heatmap. For instance, as seen by a little black box inside the image in Fig. 4.12, the maximum value happens at $\alpha = 30.2^\circ$ and $\beta = 4.2^\circ$.

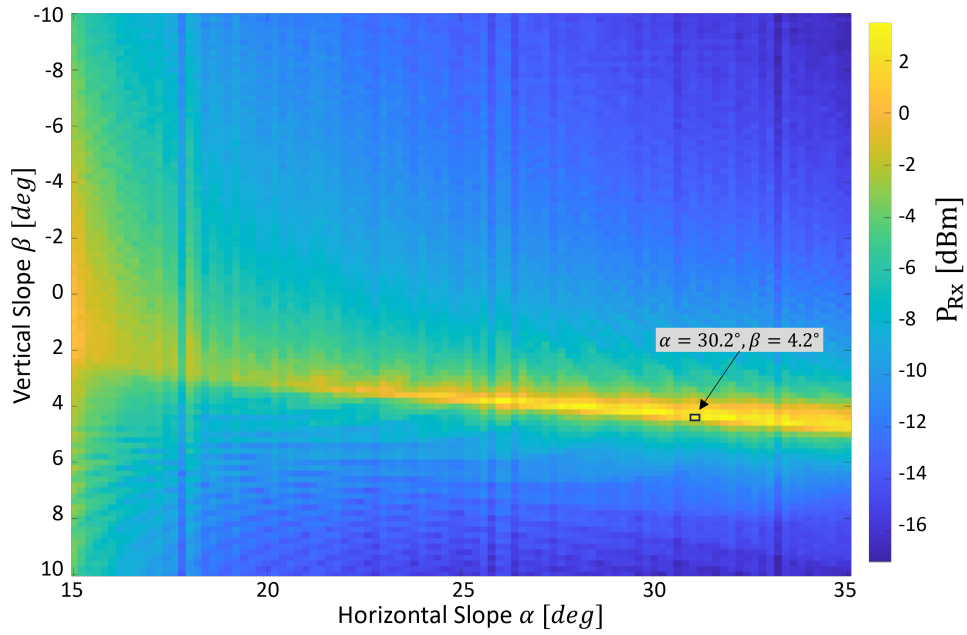


Figure 4.12: Power received RCS heatmap depicting the search for optimal slope angles to form narrow beams in the south street canyon of the urban scenario, resulting in the maximum power received at slope angle $\alpha = 30.2^\circ$ and $\beta = 4.2^\circ$, as depicted by the small black box.

Similarly, Fig. 4.13 provides the search heatmap for broad beam HELIOS, where the maximum receive power is with slope angles $\alpha_{1,1} = 20.2^\circ$ and $\beta_{1,1} = -10.2^\circ$.

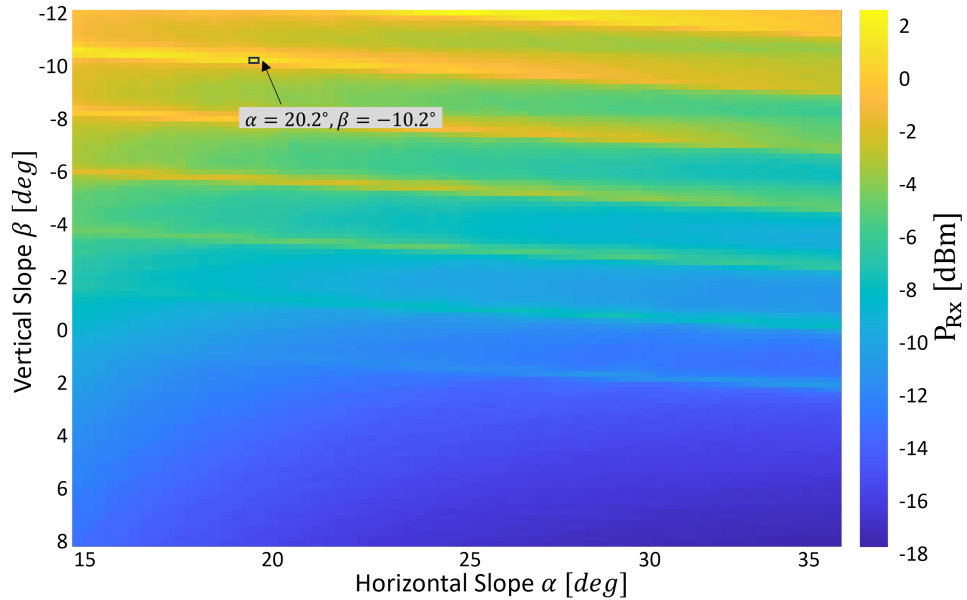


Figure 4.13: RCS received power depicting the search for optimal slope angles to form a broad beam in the south street canyon of the urban scenario. The 32 reflectors take seven different slope angles in the step of 2.5° with $\alpha = 20.2^\circ$ and $\beta = -10.2^\circ$ being its first value, where the maximum receive power is at this location.

The reflectors then take seven different slope angles in the step of 2.5° as depicted in Sec. 4.2.1. Summarizing the above two paragraphs, we have identified the following optimized HELIOS configurations:

- **Optimized narrow beam HELIOS:** Slope angle $\alpha_1 = \dots = \alpha_{32} = 30.2^\circ$, and $\beta_1 = \dots = \beta_{32} = 4.2^\circ$.
- **Optimized broad beam HELIOS:** Slope angle variation in the steps of 2.5° , $\alpha_1, \dots, \alpha_{32} \in [20.2 : 35.2]^\circ$, i.e., $\alpha_2, \alpha_1 = 20.2^\circ$, $\alpha_6, \dots, \alpha_3 = 22.7^\circ$, $\alpha_{11}, \dots, \alpha_7 = 25.2^\circ$, $\alpha_{17}, \dots, \alpha_{12} = 27.7^\circ$, $\alpha_{23}, \dots, \alpha_{18} = 30.2^\circ$, $\alpha_{28}, \dots, \alpha_{24} = 32.7^\circ$, and $\alpha_{32}, \dots, \alpha_{29} = 35.2^\circ$, and $\beta_1, \dots, \beta_{32} \in [-10.2 : 4.8]^\circ$, $\beta_2, \beta_1 = -10.2^\circ$, $\beta_6, \dots, \beta_3 = -7.7^\circ$, $\beta_{11}, \dots, \beta_7 = -5.2^\circ$, $\beta_{17}, \dots, \beta_{12} = -2.7^\circ$, $\beta_{23}, \dots, \beta_{18} = -0.2^\circ$, $\beta_{28}, \dots, \beta_{24} = 2.3^\circ$, and $\beta_{32}, \dots, \beta_{29} = 4.8^\circ$.

Compared to the previous configuration, the adoption of the elevation slope parameter is an important aspect of our optimization process. In Sec. 4.2.3, we have considered the case when $\beta_{m,n} = 0^\circ$, similar to that mentioned in [10]. However, given these intrinsic differences, comparing the optimized model to the earlier model is a little unfair.

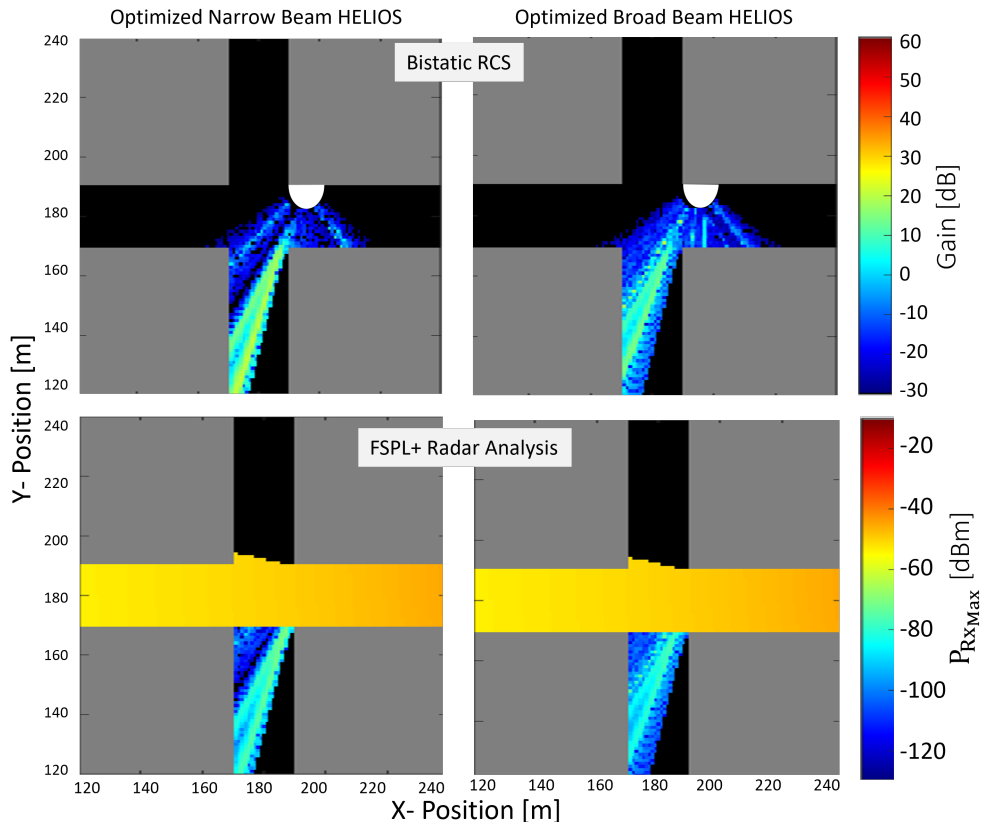


Figure 4.14: RCS comparison of narrow beam HELIOS (left column) and broad beams HELIOS (right column) in an urban scenario depicting the gain in dB (top row) and maximum power received in dBm (bottom row). The parameters are considered from Tab. 4.4 at 28 GHz frequency with the optimized slope angles.

Interestingly, we correct this imbalance in our methodology by utilizing recently unexplored aspects to strengthen the strength of the assessment, a tactical advantage not found in earlier methods. Analog to Fig. 4.11 in Sec. 4.2.3, we assess the expected performance in our street crossing scenario in Fig. 4.14. The maximum power received is displayed in the bottom row of the picture, while the top row depicts the gain behavior of the reflectors. When compared to Fig. 4.11, considerable improvements have been made by this optimization approach. The improved slope angles result in a maximum gain of 20.5 dB for narrow beams (+5.1 dB) and 19.9 dB for broad beams (+8.7 dB).

Our optimized slope angles have even more advantages, as seen by the comparison with Fig. 4.14. In addition to being more comprehensive, the coverage inside our chosen region of interest performs better, i.e., approx. 8.3% with narrow beam HELIOS and around 15.0 % with broad beam HELIOS. Our approach is thus effective in optimizing slope angles for both narrow and broad beams in the urban context, as demonstrated by the improved gain and power reception capabilities. In the given urban context, this improvement has proven to be crucial in obtaining enhanced signal strength and communication.

4.2.5 Optimizing Connectivity for Different Reflector Position

Our previous results, e.g., Fig. 4.14, indicate that a fraction of the region of interest is still not covered. This is due to the reflector position. Thus, we now move the reflector 3.5 m to the west, i.e., right to the building edge, and rerun the optimization process from Sec. 4.2.4. Thereby, we illustrate how the analytical model could be used during hybrid network planning. The optimization process yields the following configurations:

- **Optimized narrow beam HELIOS: Edge:** Slope angle $\alpha_1 = \dots = \alpha_{32} = 10.4^\circ$, and $\beta_1 = \dots = \beta_{32} = 2.2^\circ$.
- **Optimized broad beam HELIOS: Edge:** Slope angle variation in the steps of 2.5° , $\alpha_1, \dots, \alpha_{32} \in [-6.5 : 8.5]^\circ$, i.e., $\alpha_2, \alpha_1 = -6.5^\circ$, $\alpha_6, \dots, \alpha_3 = -4^\circ$, $\alpha_{11}, \dots, \alpha_7 = -1.5^\circ$, $\alpha_{17}, \dots, \alpha_{12} = 1^\circ$, $\alpha_{23}, \dots, \alpha_{18} = 3.5^\circ$, $\alpha_{28}, \dots, \alpha_{24} = 6^\circ$, and $\alpha_{32}, \dots, \alpha_{29} = 8.5^\circ$, and $\beta_1, \dots, \beta_{32} \in [-4.6 : 10.4]^\circ$, i.e., $\beta_2, \beta_1 = -4.6^\circ$, $\beta_6, \dots, \beta_3 = -2.1^\circ$, $\beta_{11}, \dots, \beta_7 = 0.4^\circ$, $\beta_{17}, \dots, \beta_{12} = 2.9^\circ$, $\beta_{23}, \dots, \beta_{18} = 5.4^\circ$, $\beta_{28}, \dots, \beta_{24} = 7.9^\circ$, and $\beta_{32}, \dots, \beta_{29} = 10.4^\circ$.

Similar to our analysis in Sec. 4.2.4, we consider RCS and received power heatmaps along the scenario using the two newly optimized HELIOS configurations at the new mounting positions. Fig. 4.15's top row shows the gain behavior, while the bottom row shows the maximum power, i.e., also considering LOS contributions, that were received. When comparing to Fig. 4.14, one can extract from Fig. 4.15 that the change of mounting of position and thereafter rerunning of the optimization algorithm is fruitful: In particular, maximum gains of 29.1 dB for narrow beams and 38.9 dB for broad beams are attained, constituting increases of 8.6 dB and 19 dB, respectively. These results highlight how important reflection beamwidth is in affecting the system's overall performance.

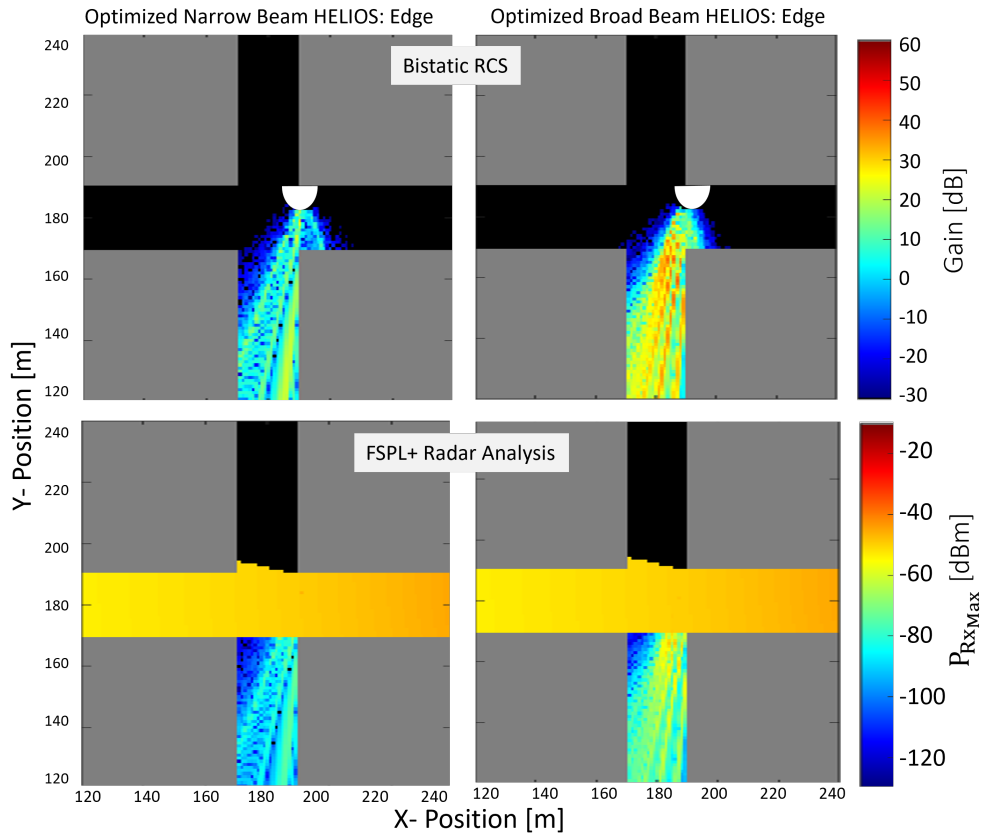


Figure 4.15: RCS comparison of optimized narrow beam HELIOS (left column) and broad beams HELIOS (right column) in an urban scenario depicting the gain in dB (top row) and maximum power received in dBm (bottom row). The parameters are considered from Tab. 4.4 at 28 GHz frequency with the optimized slope angles at the edge of the building.

Moreover, we can see that the adjusted reflector placement greatly improves both the coverage and performance within our region of interest. These constitute to coverage area of about 30.1 % with narrow beam HELIOS and 79.3 % with broad beam HELIOS. This coverage is better than the previous models in Fig. 4.14 and Fig. 4.11.

To conclude, we have thereby shown the potential gains HELIOS reflectors may provide in such a scenario. In this context, we have shown the benefits a thorough optimization in terms of geometry configuration and mounting position may have. However, one must note that our attained performance does not constitute the global maxima. Future work on this optimization topic, which is out of the scope of this thesis, is likely to achieve even better results.

4.2.6 Analyzing IRS Based Connectivity

Now that we have explored the performance of the analytical model for reflectors in urban scenarios, we may now compare the performance of HELIOS reflectors against IRSs using the respective

analytical models from Sec. 2.3.3. Like in Sec. 4.2.5, the IRS shall be mounted at the more suitable, changed mounting position at the edge of the building to maximize the coverage in the south street canyon. This section considers two cases: First, we use the IRS model by Özdogan *et al.* [46] Sec. 2.3.3 and consider it for a fixed configuration reflecting the energy in a bundle fashion into the region of interest. Second, we employ all three models [46–48] and consider the maximum gain throughout the scenario for the case that the IRS is set to beamform to each possible UE position, thus contrasting the previous case.

Similar to our analysis from Fig. 4.12, the performance results with $\gamma_{Rx}(\theta_{Rx}, \varphi_{Rx}) = \gamma_{Rx}$ (-2.5° , -25.75°) yields the best to serve the south street canyon. The gain and power received RCS heatmaps in Fig. 4.16 compare two separate instances shown in this model. In the first scenario, the user is positioned at the angle at which the IRS is precisely pointing also referred to as a "dynamic beam", i.e., when $\gamma_{Rx} = \gamma_{Dev}$. When $\gamma_{Rx} \neq \gamma_{Dev}$, i.e., a user-performed angle sweep is indicated in the second scenario which is also referred to as a "fixed beam". The latter scenario in this case leads to the narrow beams being generated.

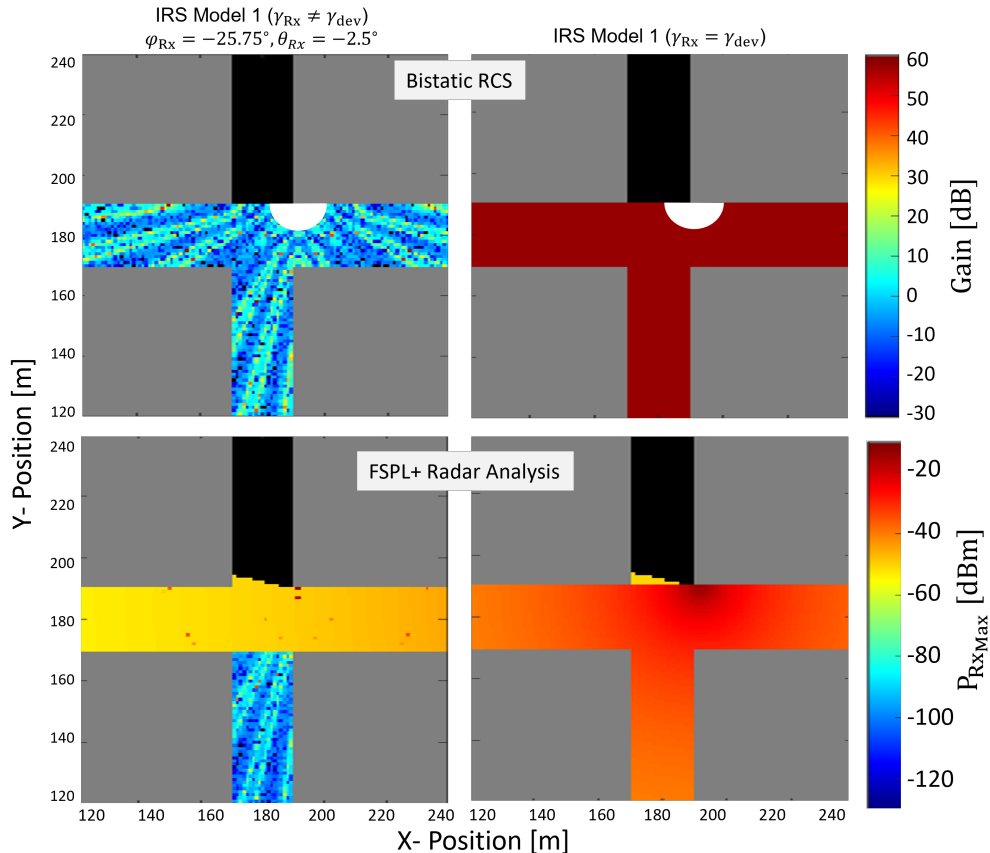


Figure 4.16: RCS comparison of two cases of IRS model 1 (Sec. 2.3.3): fixed beam case on the left column and dynamic beam on the right column in an urban scenario depicting the gain in dB (top row) and maximum power received in dBm (bottom row). The parameters are considered from Tab. 4.4 at 28 GHz frequency with the optimized slope angles at the edge of the building.

The examination of maximum gain in Fig. 4.16 shows that both fixed and dynamic beam cases of IRS model 1 have 57.5 dB gain, which constitutes to increase by 28.4 dB as compared to Fig. 4.15. Comparison between RCS heatmaps by both the scenarios of model 1 is mainly in terms of beam pattern and coverage. The coverage area is almost 100 % when $\gamma_{Rx} = \gamma_{Dev}$ (dynamic beam), whereas when the reflector focuses on the UE location (fixed beam), the coverage is 13.3 %. This disparity highlights the multifaceted performance features of IRS model 1, in which the dynamic redistribution of signals occurs in different beam patterns and coverage areas while attaining the same advantages.

Turning our attention to Fig. 4.17, which summarizes the results related to the other two IRS models discussed in Sec. 2.3.3. The peak gain for the second and third IRS models are 57.5 dB and 57.4 dB, respectively. These two models show coverage area in south street canyon by almost 97.7 % and 100 %, respectively, which are comparable to the results from the first IRS model with dynamic beam. The performance of IRS model 1 with the fixed beam is more comparable with our HELIOS analytical model in the urban scenarios with different reflector placement, see Sec. 4.2.5. A similar comparative analysis is carried out in Sec. 2.3.4, but without the scenario implementation.

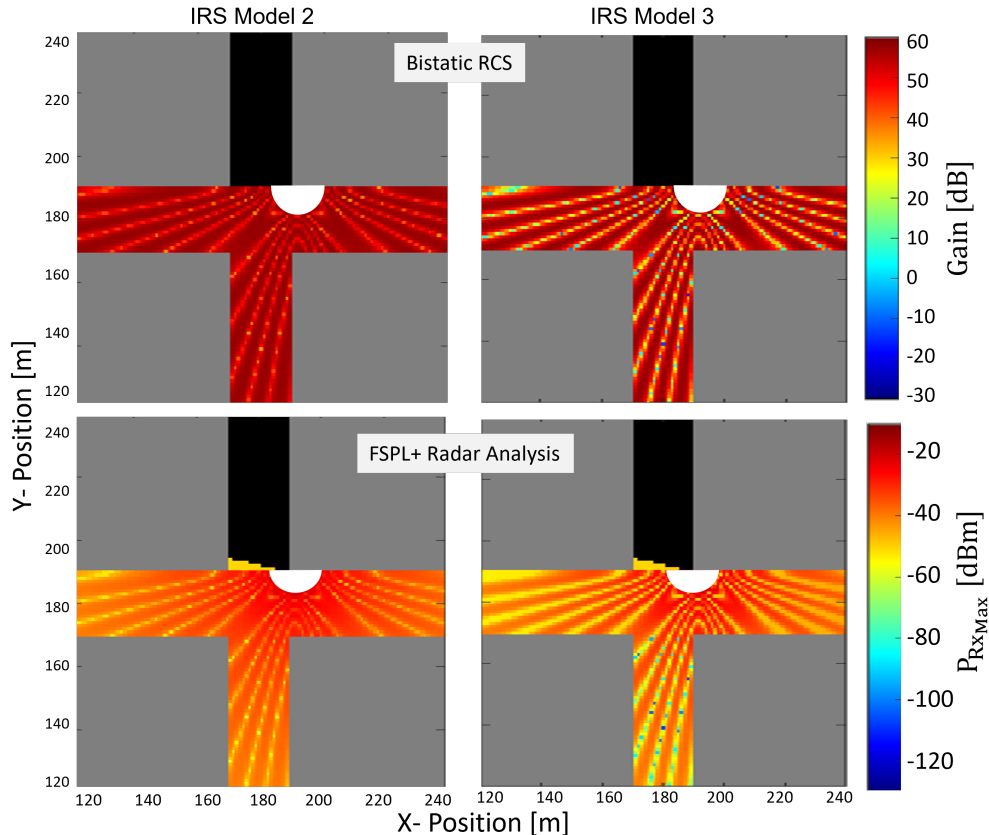


Figure 4.17: RCS comparison of IRS model 2 (left column) and IRS model 3 (right column) (Sec. 2.3.3) in an urban scenario depicting the gain in dB (top row) and maximum power received in dBm (bottom row). The parameters are considered from Tab. 4.4 at 28 GHz frequency with the optimized slope angles at the edge of the building.

Further moving on to the detailed assessments of these models in Fig. 4.11, Fig. 4.14, Fig. 4.15, Fig. 4.16, and Fig. 4.17 can be observed in Sec. 4.2.7. The intrinsic ability of IRS models to effectively serve several locations and their dynamic signal redirection capabilities, which let them modify and improve the transmission path to accommodate various user locations, is what distinguishes them. These IRS models' adaptability and versatility highlight how important they are for improving signal propagation and increasing coverage in a variety of settings.

4.2.7 Comparison of IRS and HELIOS based Connectivity Enhancements

We thoroughly investigated our HELIOS reflector performances in prior sections. This required a thorough examination of the baseline connectivity for a variety of channel models, which enabled us to make insightful comparisons with simulated outcomes from [10]. We conducted a lengthy investigation to improve the reflectors' performance in our particular area of interest. This entailed carefully adjusting the reflectors' geometry and placement to maximize their effectiveness and match the special qualities of the region we had chosen. Moreover, our investigation went beyond a theoretical examination, as we used the IRS models in our urban scenario. We showed the strong connectivity such large IRSs could provide in the whole area when beamformed to the respective UE positions.

In this section, we now directly compare the three IRS models with the analytical HELIOS reflectors in great detail. The goal of this analysis is to draw attention to the advantages, and disadvantages of these two strategies. A detailed ECDF plot shown in Fig. 4.18 illustrates the power received in dB m within the selected region of interest. Sec. 4.2.2, Sec. 4.2.4, Sec. 4.2.5, and Sec. 4.2.6 of this analysis provide a comparative examination of several reflector configurations. Our main goal is to clarify the differences in performance between different settings.

A significant finding is revealed when analyzing the reflector geometries covered in Sec. 4.2.2, and Sec. 4.2.3: The curves indicate that there is a potential coverage possible in the south street canyon region if the RCS directed to this area was higher. The changed HELIOS position shows that it is in a better mounting position for the intended south street coverage by 35–40 %. The deliberate emplacement of reflectors, five meters from the building's edge, is responsible for this decrease, as they do not serve some part of the intended coverage region. When moving the reflector to a more suitable mounting position closer to the edge of the building, we observe a great impact as the whole region of interest is now in LOS from the reflector. HELIOS indeed enables mmWave connectivity in 80.2 % of the area of interest, with mean and maximum receive powers of -75.2 dBm and -49.3 dBm . The behavioral analysis of IRS models is also included in Fig. 4.18. Compared to passive reflectors, the IRSs function better, offering better coverage and stronger signals. This superiority results from the IRS's dynamic nature, which allows them to focus on each UE position individually. The capacity of IRS to dynamically optimize signal propagation, surpassing conventional designs, makes them a clear advantage over passive reflectors.

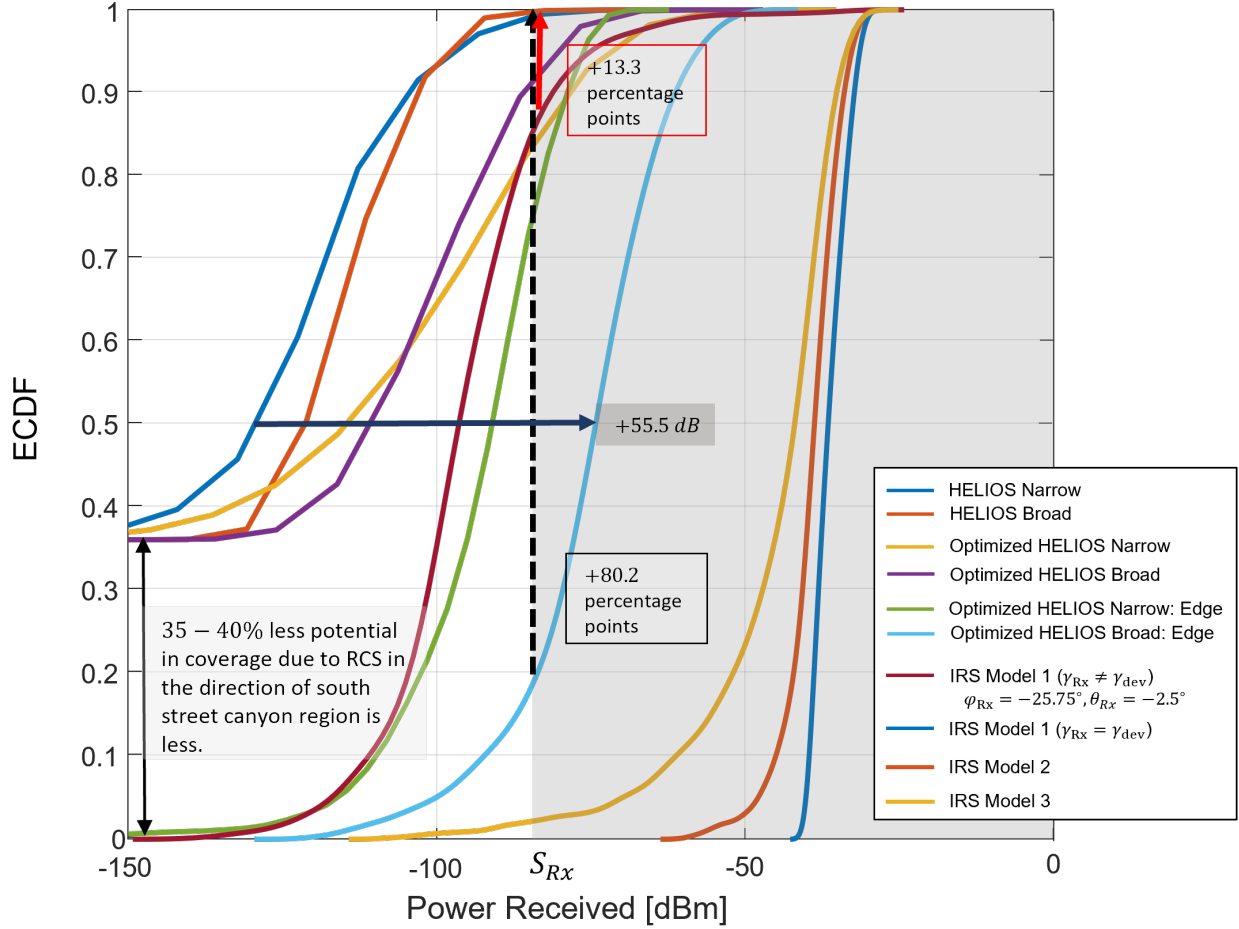


Figure 4.18: ECDF plot depicting the power received in the south street canyon thus showcasing the performance of HELIOS and IRSs as predicted by analytical models, cf. Sec. 2.3.3 ([46–48]). Notably, the optimized broad beam HELIOS (geometry configuration + mounting position) shows more than 80.2 % percentage coverage in our region of interest, while the fixed beam case of IRS model 1 exhibits 13.3 % coverage. Our optimization increased the mean receive power by 55.5 dB against [10]. However, when compared to IRS which may reconfigure the reflection such that any position in the range is deliberately targeted, we still observe on average tens of dB of loss as well as reduced coverage.

However, we note that when fixing an IRS to a fixed configuration, i.e., fixed beam case of first IRS model, we showed that HELIOS reflectors can perform better in comparison. An important takeaway from our case study is that reflector geometry and position optimization of a HELIOS reflectors have a significant effect on signal strength and coverage. This considerable improvement highlights the effectiveness of our approach in enhancing coverage area and signal propagation. Nonetheless, we point out the scope for more improvement as sophisticated algorithms should be considered for such purposes in the scope of hybrid network planning and HELIOS reflector customization processes.

Case Study: Analyzing Behavior of Optimized HELIOS (Geometry Configuration + Mounting Position) Reflector on Frequency Variation

Building upon the previous investigations conducted at 28 GHz frequency, this study delves into analyzing the peak gain behavior for a frequency range from 0.4 GHz to 71 GHz in the steps of 0.1 GHz for an optimized narrow beam HELIOS (Geometry configuration+ mounting position), see Sec. 4.2.5. Fig. 4.19 illustrates the reflector gain behavior across this spectrum, revealing three distinct regions: (a) $f \in [0.4 : 2.0]$ GHz, where lower gains are observed at lower frequencies. (b) $f \in [2.0 : 38.7]$ GHz shows higher gains indicating optimal performance of the reflectors. (c) $f \in [38.7 : 71]$ GHz is characterized by higher frequencies, a noticeable loss in gain exceeding 5 dB is observed.

Fig. 4.20 depicts the peak gains achieved in the green color-coded region, i.e., a peak gain value of 31.8 dB at 2.8 GHz being the highest, with 31.0 dB at 9 GHz, 15.1 GHz, and 21.1 GHz being the second highest peaks. Notably, at 28 GHz frequency, we observe a peak gain of 29 dB which is the same as the results we got from Sec. 4.2.5. The RCS gain and receive power behavior at 2 GHz, 28 GHz, and 48 GHz frequency is seen in Fig. 4.20. The three frequencies in the figure belongs to each of the three distinct regions in Fig. 4.19. Initially, we observe that the near-field region (white-colored region), increases as the frequency increases. This direct dependency on frequency can be observed from Eq. (4.3).

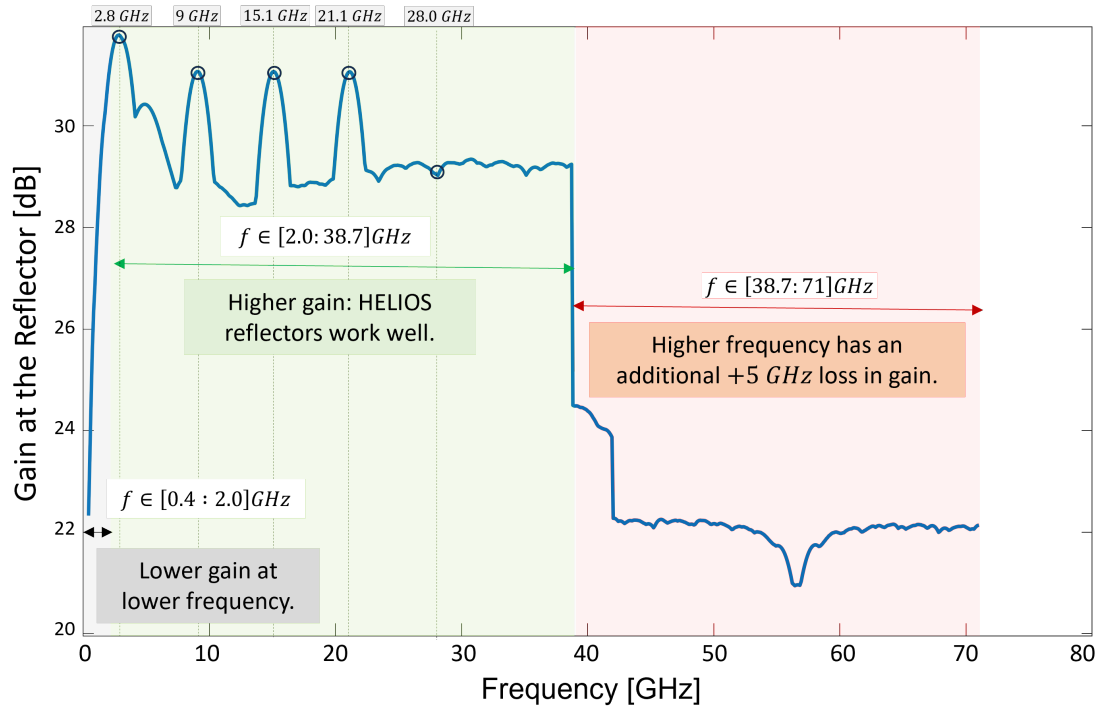


Figure 4.19: Variation of peak gain for span in frequency range $f \in [0.4 : 71]$ GHz in the steps of 0.1 GHz. Three distinct frequency ranges depend on the peak gain values as depicted with color coding. Higher gains are observed in the green region showcasing the better performance of the HELIOS reflectors in this frequency range.

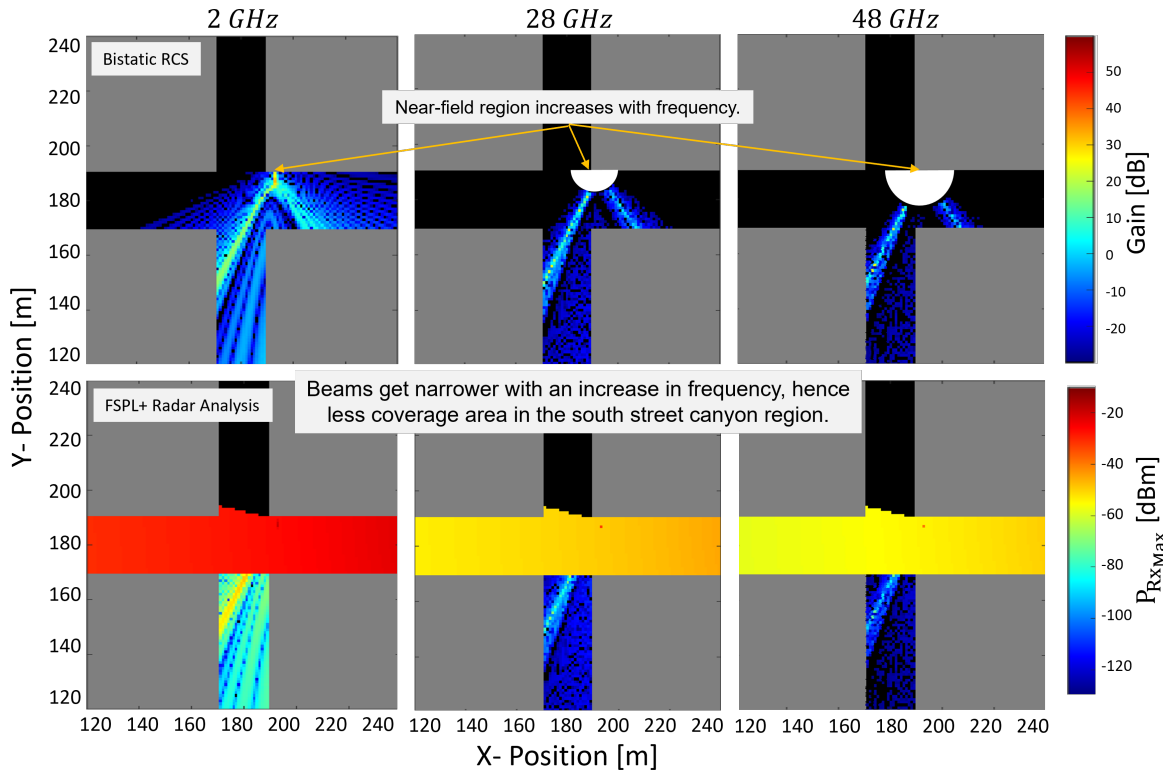


Figure 4.20: RCS comparison of optimized narrow beam HELIOS (Geometry configuration+ mounting position) at 2 GHz, 28 GHz, and 48 GHz frequency in an urban scenario depicting the gain in dB (top row) and maximum power received in dBm (bottom row).

Referring to Eq. (3.7), the direct dependency of frequency ($f = \frac{2\pi}{\lambda}$) inside the sinc function of a HELIOS module, due to which the value inside the sinc function reduces as frequency increases. Thus leading to the narrow beam, as observed in Fig. 4.20 from 2 GHz to 48 GHz. The coverage area in the south street canyon region accounts for 97.0%, 23.0%, and 6% for models operating with 2 GHz, 28 GHz, and 48 GHz, respectively. A drastic decrease in coverage area by almost 91% occurs as the frequency increases.

4.2.8 Sensitivity Point: HELIOS performance with UMi-Radar Equation

The above study items have used FSPL channel models in an urban setting. It is imperative to acknowledge, nevertheless, that other channel models like the 3GPP UMi and others are typically a better choice for such. The basic formula for representing radar behavior in different contexts is found in Fig. 4.8. Using the insights from Eq. (4.2), we now explicitly examine the behavior when coupled with different propagation models. To use these models together with the reflecting surface, the channel is split into two parts: LOS and NLOS region as mentioned in Tab. 2.2, unlike FSPL which considers LOS paths only. Using the factor $\Delta D_{ChainedFSPL}$ as introduced previously in

Sec. 4.2.2, we thus extend the UMi channel model to a radar equation-like formula as follows:

$$PL_{UMi_{Radar}}(r_{Tx,Ref}, r_{Ref,Rx}, f, \sigma_{Meta}, G_{Tx}, G_{Rx}) = PL_{UMi}(G_{Tx}, r_{Tx,Ref}, f) + PL_{UMi}(G_{Rx}, r_{Ref,Rx}, f) + \sigma_{Meta} - \Delta D_{UMi} \quad (4.4)$$

$$\Delta D_{UMi} = 52 \cdot \log_{10}(4 \cdot \pi) - 20 \cdot \log_{10}(c) + 20 \cdot \log_{10}(f). \quad (4.5)$$

Although resembling the $\Delta D_{ChainedFSPL}$ parameter used in FSPL, it incorporates a distinct offset of $52 \cdot \log_{10}(4 \cdot \pi)$ as seen in Eq. (4.5). The rationale behind selecting this changed offset lies in its ability to account for scenarios where reflectors are situated near the transmitter, typically within a few tens of meters. This offset ensures that the radar path loss neither exceeds the NLOS value nor proceeds LOS value, especially when the reflector is located near the transmitter. Using the above equation, Fig. 4.21 gives a brief comparison of predicted and radar path losses for an arbitrary scenario assuming $\sigma_{Meta} = 0$ dB and the reflector is located at 50 m. The same assumptions were carried out for FSPL in Fig. 4.8.

The minimum range of $r_{Tx,Rx}$ as seen from Tab. 2.2 is 10 m [37]. Observing the figure, there is a noticeable shift in the radar curve of about 13 dB, at the reflector's assigned position with an ideal offset of $52 \cdot \log_{10}(4 \cdot \pi)$. Having seen the new radar-like performance, we now consider the HELIOS deployment from Sec. 4.2.5 and consider the attained connectivity boost, see Fig. 4.22.

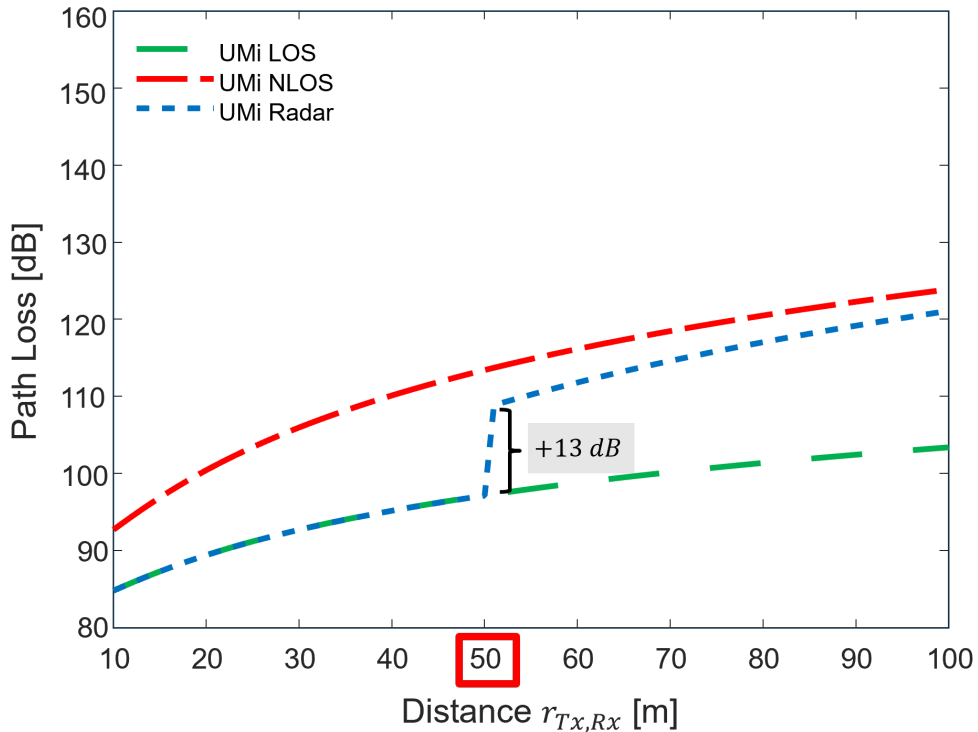


Figure 4.21: Comparison between predicted LOS, NLOS path loss of UMi channel model, and the radar equation over the total distance between Tx and Rx. For the radar curve, we assume LOS connectivity for the first 50 m, as the reflector is located at 50 m from Tx. Thereafter, it follows the radar path with $\sigma_{Meta} = 0$ dB and $r_{Tx,Rx} = r_{Ref,Rx}$.

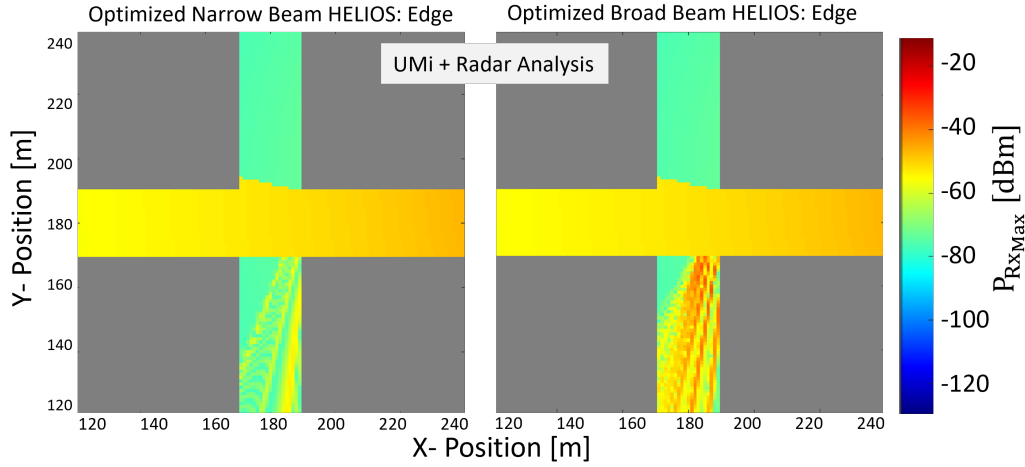


Figure 4.22: UMi channel model RCS comparison of optimized narrow beam HELIOS (left column) and broad beams HELIOS (right column) in urban scenario depicting maximum power received in dBm. The parameters are considered from Tab. 4.4 at 28 GHz frequency with the optimized slope angles at the edge of the building, see Sec. 4.2.5.

We find additional connectivity to the NLOS region using the UMi channel model in an urban scenario. When compared to the results in Sec. 4.2.5, the coverage area in the south street canyon enhanced by more than 60 %, and 19.3 % with optimized narrow and broad beam HELIOS, respectively. Similar to the deployment in Sec. 4.2.7 and for the same deployment of reflectors, we extend our study with new IRS channel models Sec. 2.3.3. Comparing the results between Fig. 4.23, and Fig. 4.16, we achieve enhanced coverage area with fixed beam case of IRS model by 78.1 %, whereas the other case dynamic beam provides 100 % coverage.

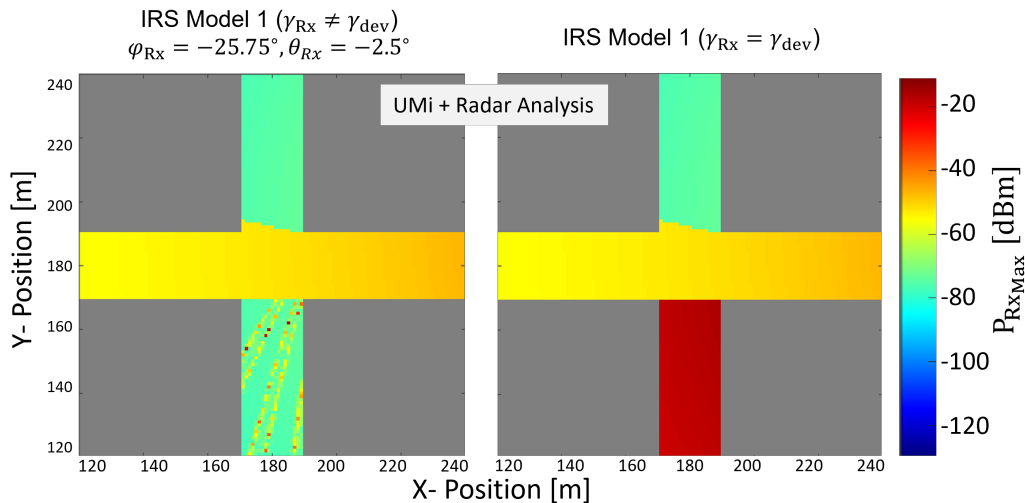


Figure 4.23: UMi channel model RCS comparison of two cases of IRS model 1 (Sec. 2.3.3): fixed beam case on the left column and dynamic beam on the right column in an urban scenario depicting maximum power received in dBm. The parameters are considered from Tab. 4.4 at 28 GHz frequency with the optimized slope angles at the edge of the building, see Sec. 4.2.5.

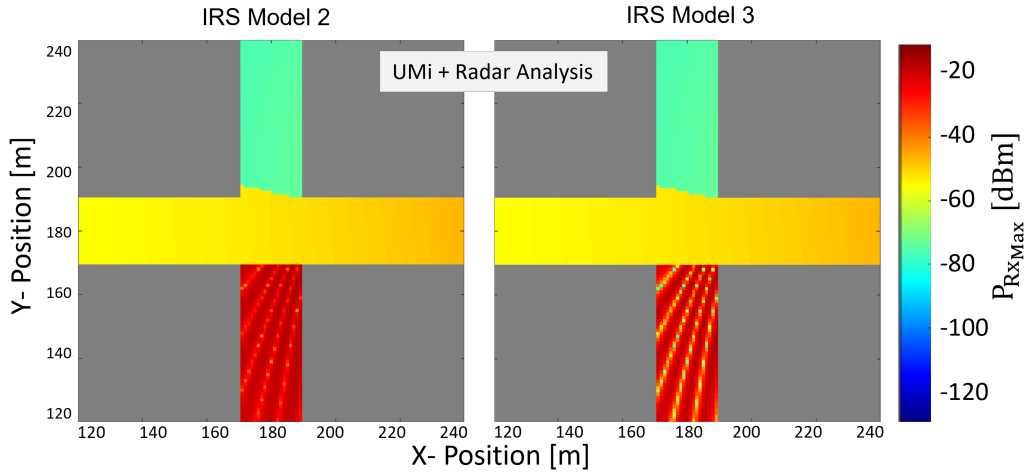


Figure 4.24: UMi channel model RCS comparison of two IRS models Sec. 2.3.3 in urban scenario depicting maximum power received in dBm. The parameters are considered from Tab. 4.4 at 28 GHz frequency with the optimized slope angles at the edge of the building, see Sec. 4.2.5.

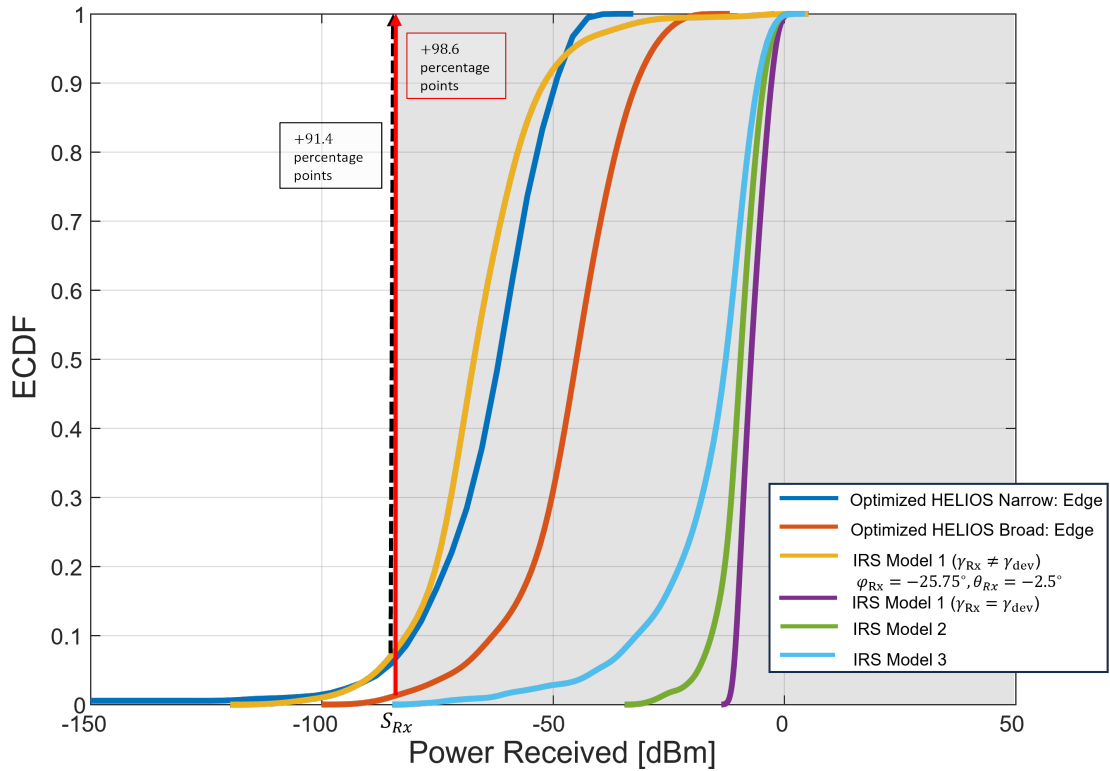


Figure 4.25: ECDF plot depicting the power received in the south street canyon in dBm by UMi channel model in urban scenario, highlighting the performance and coverage by our optimized HELIOS analytical model and IRS models [46–48] in Sec. 2.3.3. Notably, optimized HELIOS broad beam around the edge of the building shows more than 98.6 % percentage coverage in our region of interest, while fixed beam case of IRS model 1 exhibits 91.4 % coverage.

The comparison of Fig. 4.24, and Fig. 4.17, we achieve 100 % coverage in south street canyon using UMi channel modeling. In the above figure, the power is radiating in the direction of south street canyon with a coverage area of around 92.5 % with narrow beam and 98.6 % with broad beam HELIOS (geometry configuration + mounting position) (see Fig. 4.23). Whereas active IRS models show a coverage area of around 100 % in all the cases. Like in Sec. 4.2.7, we bundle the results from Fig. 4.22, Fig. 4.23, and Fig. 4.24 in Fig. 4.25 depicting the respective receive power ECDFs. Notably, the coverage area in the south street canyon by almost all reflecting surfaces of the curves approaches 100 %, contrasting to the ECDF plot in Fig. 4.18 with FSPL channel model. These much more optimistic results come from the UMi channel's behavior to account for the complex interactions found in urban environments, such as reflections, diffraction, and scattering. This leads to a more accurate representation of signal propagation in intricate urban landscapes. In contrast, FSPL oversimplifies the scenario by ignoring these environmental details, which results in an underprediction for the connectivity. However, if taken as the basis for network planning, this will ensure over-provisioning by network operators (using BSs and metasurfaces) which would be of interest for the users.

4.3 Outlook on Future Arbitrarily-Shaped HELIOS Reflecting Surfaces

We have used the simulation program in our endeavor to optimize reflector designs, and we have used both squared and rectangular reflecting surfaces. Moving away from such flat reflecting surfaces, e.g., by introducing curvature, cf. [10], such a HELIOS reflector is represented in the form of triangulated geometry. The use of a large number of triangle surface patches for complex 3D objects is typical in computer graphics and a key part of CAD programs and related file formats such as *.stl. To put our analytical model to use for more complex reflecting surface geometries, we briefly study to what regards the behavior changes and what this would mean for our analytical model.

One of the main differences between the triangle and rectangles is the surface area size. The area of a rectangle, denoted by A_{rect} , can be found by multiplying its sides $a \cdot b$. In contrast, the area of a triangle is just $A_{tri} = \frac{1}{2} \cdot (a \cdot b)$. Considering that the RCS is proportional to the area squared, see Eq. (3.9), one would expect a 6 dB loss in peak RCS. However, when using two triangles to construct a rectangle from two triangles, these differences should be remedied and the overall RCS pattern should match our current analytical model. In the following, we assess how the RCS pattern for triangular surface patches differs from the one from a rectangular surface. We consider four different triangles that fit into the space spanned by a quadratic surface patch of size $a = b = 0.1$ m, see top of Fig. 4.26. As a result, different edge alignments around the surface patches are realized. They are highlighted in black when parallel to the z -axis, yellow when parallel to the y -axis, and red and peach when in the y - z -plane with a rising or falling gradient. In the middle of the figure, we present the arising RCS heatmaps given a 28 GHz incident wave from direction

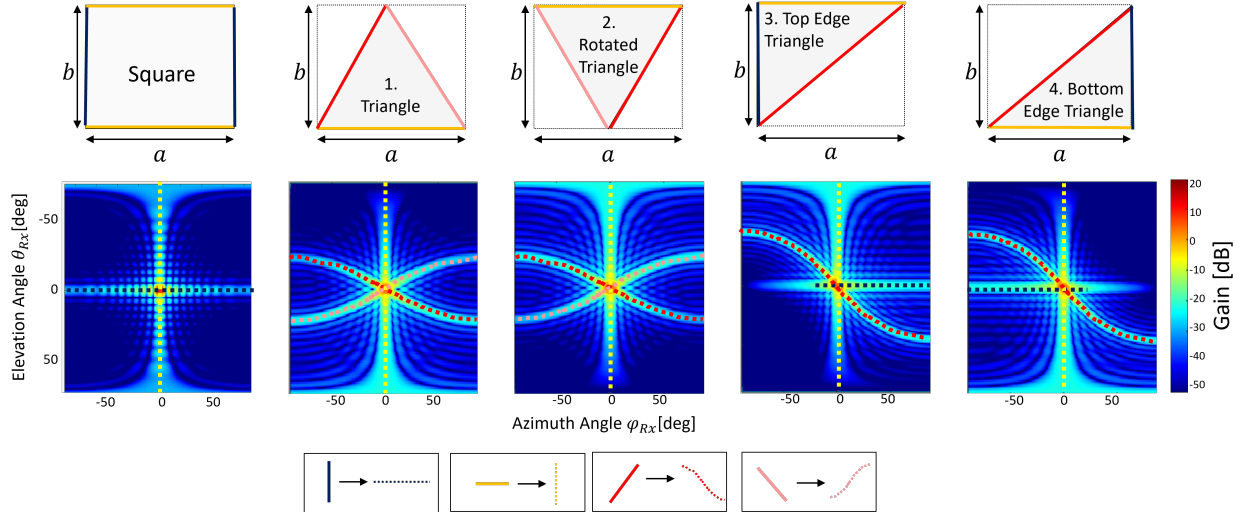


Figure 4.26: Illustration of the squared and triangle geometry models with different triangular orientations with their RCS behavior depicting the gain in dB. Assuming the flat plate geometry with $\varphi_{Tx} = \theta_{Tx} = 0^\circ$, the color coding on the geometry of square and triangle can be seen on the RCS heatmap, denoting the impact of the different sides of the geometry on the RCS behavior, which is the same for various orientations of the triangular plate.

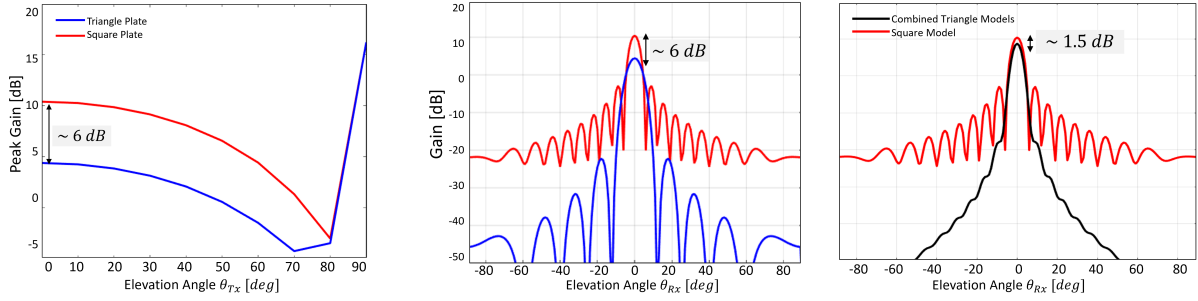
$\varphi_{Tx} = \theta_{Tx} = 0^\circ$. Interestingly, the four different triangles exhibit unique RCS patterns, although there are similarities with the RCS pattern of the square-shaped surface patch on the left if the respective triangle also contains an edge along the y-axis (black), and x-axis (yellow). The best match is for triangles number 3 and 4, which feature both a black and a yellow edge. Here we see that the red edge must be the reason why a diagonal-like pattern arises in the RCS pattern.

Due to this, we can also conclude that the peach-colored edge must be the origin for the 180° rotated diagonal-like pattern in the RCS. As such we concluded that an analytical model of the RCS pattern needs to factor in the orientation of the edges, respectively, to recreate such patterns.

Fixing $\varphi_{Tx} = 0^\circ$, Fig. 4.27(a) explores the peak RCS along different θ_{Tx} in the range from $[0 : 90]^\circ$. We observe a 6 dB difference for $\theta_{Tx} = 0^\circ$, as expected from our earlier consideration. For larger θ_{Tx} , the difference mitigates. This is because the main lobe changes and σ_{Tri} outside of the main lobe depends not only on A_{tri}^2 but also strongly on $\varphi_{Tx}, \theta_{Tx}, \varphi_{Rx}$, and θ_{Rx} .

As can be seen from Fig. 4.27(b) and Fig. 4.27(c), a different beamwidth pattern occurs for triangle and rectangle surfaces. Referring to Fig. 4.26 again, the RCS "summation" of the final two triangles, using Eq. (3.8), is now compared in Fig. 4.27(c) to the RCS of the equivalent square-shaped reflecting surface. We observe that the main lobe peak differs by approx. 1.5 dB, however, the form of the mainlobe matches nicely. We further find that the RCS patterns from two triangles are not able to represent the sidelobes of the rectangle accurately.

This outlines that RCS patterns of arbitrary complex geometries represented using triangles may be prone to errors, particularly in the sidelobe region. Nonetheless, it is important to note that the



(a) Variation of peak gain in dB for the sweep along the elevation angle θ_{rx} when $\varphi_{Tx} = 0^\circ$. A notable difference of 6 dB is observed at $\varphi_{Tx} = \theta_{Tx} = 0^\circ$ for triangle number 1 in Fig. 4.26. The other triangles yield the same result as this.

(b) Gain behavior in dB when plotted against elevation angle θ_{rx} , observing a 6 dB decrease in the gain from that of rectangle plate considering triangle number 1 in Fig. 4.26.

(c) Gain behavior in dB when plotted against elevation angle θ_{rx} . The RCS "summation" of triangle numbers 3 and 4 in Fig. 4.26 leads to a black curve, where we observe a 1.5 dB decrease in the gain from that of the rectangle plate.

Figure 4.27: Gain behavior in dB for the rectangle and triangle plate when $a = b = 0.1$ m, and $\varphi_{Tx} = \theta_{Tx} = 0^\circ$. The main difference between the two plates are is their areas, due to which we observe 6 dB between these models as depicted.

main lobe is still accurate such that a potential analytical model may still be used with sufficient accuracy to assess the performance in the intended reflection direction of the reflector.

5 Conclusion

In this master thesis, we dug into the complex environment of mmWave communication and its propagation properties, thus establishing the background for our work. Our main focus is on passive reflectors in the form of HELIOS reflectors [10], which demonstrates a scalable, non-reconfigurable option with immediate viability.

In Sec. 3.2, we first conducted EM simulations to identify key components of HELIOS reflection behavior. Notably, increasing the reflector size has an impact on the reflection gain and also on the reflection beamwidth. Sec. 3.3 then procured an analytical HELIOS reflection model for a single module, for which we identified a matching reflection main lobe behavior in terms of peak gain as well as horizontal and vertical beamwidths. Superimposing the formula and addressing potential self-shadowing effects, Sec. 3.4 provides the final RCS model for HELIOS consisting of $M \times N$ modules. By comparing to EM simulations, we identified, e.g., 0.02 dB and 0.20 dB differences for the peak gain for 1×8 and 8×8 HELIOS configurations, respectively, thus validating our analytical model. Moreover, we performed case studies to investigate the behavior of a fixed geometry along different frequencies, for varying reflecting surface sizes, and in what regard overprediction against simulation may occur. For the latter, we show that mean, median, and maximum value are rather underpredicted, which is a desirable characteristic in the context of network planning.

Sec. 4.1 then followed up with a computing time study, demonstrating the analytical model's higher speed against EM simulations by being up to, e.g., approximately 55,000 times faster for a 4×4 HELIOS with 1° angular resolution, thus enabling use cases as showcased throughout Sec. 4.2 as follows. A thorough comprehension of the urban setting is gained where we anticipate various communication channel models based on two unique reflector deployments: narrow and broad beam HELIOS. The overall coverage area in the south street canyon with FSPL channel modeling and radar realization for initial assessment from [10] is very little, nearly 1 %. The model's optimization concerning change in geometry and reflector position has greatly increased coverage regions, reaching up to 79.3% with the broad beam HELIOS and 30.1% with the narrow beam HELIOS. The examination of IRS models indicates the increase in the coverage area by all the models, especially the third IRS model Sec. 2.3.3 with 100% coverage. Further interpreting with UMi channel models using radar realization, a significant increase in coverage area is observed for optimized geometry and reflector placement with almost 98.6% with the broad beam HELIOS and 94.5% with the narrow beam HELIOS.

5.1 Outlook

During the derivation and evaluation of our analytical model, we pointed out effects by self-shadowing and diffraction. Whereas we already addressed the former, one may still extend the current implementation from horizontal/vertical shadowing to also include diagonal shadows, cf. Sec. 3.4.2. Further, this thesis recommends future work on including the diffraction behavior, but also reflection contributions of diffracted incident waves. For this purpose, existing edge and wedge diffraction concepts need to be investigated. Similarly, analytical models for trihedral corner reflectors which consider contributions of reflections of self-reflections are also a starting point for this [62, 63].

Abbreviations

IoT Internet of Things

ITS Intelligent Transportation Systems

mmWave millimeter-Wave

IRS Intelligent Reflecting Surface

3GPP Third Generation Partnership Project

FR1 Frequency Range 1

FR2 Frequency Range 2

FR3 Frequency Range 3

FR4 Frequency Range 4

FR5 Frequency Range 5

EM Electro-Magnetic

ITU International Telecommunication Union

EHF Extremely High Frequency

UHF Ultra High Frequency

XR extended Reality

SNR Signal-to-Noise Ratio

LOS Line-of-Sight

VLOS Virtual-Line-of-Sight

NLOS Non-Line-of-Sight

UMa Urban Macro

UMi Urban Micro

5GCM 5G Channel Model

METIS Mobile and wireless communications Enablers for the Twenty-twenty Information Society

MiWEBA Millimeter-Wave Evolution for Backhaul and Access

QuaDRiGa QUAsi Deterministic Radio channel GenerAtoR

ISD Inter-Site Distance

HELIOS Holistic Enlightening of bLackspots with passIve reflectOr moduleS

SRE Smart Radio Environments

RCS Radar Cross Section

RIS Reconfigurable Intelligent Surface

RSS Received Signal Strength

JCAS joint communication and sensing

Bibliography

- [1] S. He, Y. Zhang, J. Wang, J. Zhang, J. Ren, Y. Zhang, W. Zhuang, and X. Shen, "A survey of millimeter-Wave communication: Physical-layer technology specifications and enabling transmission technologies," *Proceedings of the IEEE*, vol. 109, September 2021.
- [2] T. L. Ericsson, "6G : Connecting a cyber-physical world - ericsson," July 2023, accessed: 02 Jan 2024. [Online]. Available: <https://www.ericsson.com/en/reports-and-papers/white-papers/a-research-outlook-towards-6g>
- [3] Nokia Bell Labs, "6G: The network behind the complete metaverse experience," Accessed: 02 Jan 2024. [Online]. Available: <https://www.bell-labs.com/research-innovation/what-is-6g/6g-technologies>
- [4] C. Wang, J. Huang, H. Wang, X. Gao, Y. Xiaohu, and Y. Hao, "6G wireless channel measurements and models: Trends and challenges," *IEEE Vehicular Technology Magazine*, vol. 15, December 2020.
- [5] X. Wang, L. Kong, F. Kong, F. Qiu, M. Xia, S. Arnon, and G. Chen, "Millimeter wave communication: A comprehensive survey," *IEEE Communications Surveys & Tutorials*, vol. 20, June 2018.
- [6] K. Heimann, S. Häger, and C. Wietfeld, "Demo abstract: Experimental 6G research platform for digital twin-enabled beam management," *ACM Conference on Modeling Analysis and Simulation of Wireless and Mobile Systems(MSWIM)*, pp. 125–128, October 2023.
- [7] F. Okogbaa, Q. Ahmed, F. Khan, W. Abbas, F. Che, S. A. R. Zaidi, and T. Alade, "Design and application of Intelligent Reflecting Surface (IRS) for beyond 5G wireless networks: A review," *Sensors*, vol. 22, March 2022.
- [8] S. Shen, B. Clerckx, and R. Murch, "Modeling and architecture design of reconfigurable intelligent surfaces using scattering parameter network analysis," *IEEE Transactions on Wireless Communications*, vol. 21, August 2021.
- [9] Q. Wu and R. Zhang, "Towards smart and reconfigurable environment: Intelligent reflecting surface aided wireless network," *IEEE Communications Magazine*, vol. 58, November 2019.
- [10] S. Häger, K. Heimann, S. Böcker, and C. Wietfeld, "Holistic enlightening of blackspots with passive tailorable reflecting surfaces for efficient urban "mmWave" networks," *IEEE Access*, vol. 11, April 2023.
- [11] C. Balanis, "Advanced engineering electromagnetics, 2nd ed. john wiley & sons," vol. 31, no. 6, April 2012.
- [12] L. B. L. D. E. Kerr, S. A. Goudsmit and E. A.M. Stone, "Propagation of short radio waves, ser. electromagnetics and radar. institution of engineering and technology," April 1987.

- [13] M. Banafaa, I. Shaya, J. Din, M. Hadri Azmi, A. Alashbi, Y. Ibrahim Daradkeh, and A. Al-hammadi, “6G mobile communication technology: Requirements, targets, applications, challenges, advantages, and opportunities,” *Alexandria Engineering Journal*, vol. 64, August 2022.
- [14] Y. Xiaohu, C.-X. Wang, J. Huang, X. Gao, Z. Zhang, M. Wang, Y. Huang, C. Zhang, Y. Jiang, J. Wang, M. Zhu, B. Sheng, D. Wang, Z. Pan, P. Zhu, Y. Yang, Z. Liu, Z. Ding, X. Tao, and Y.-C. Liang, “Towards 6G wireless communication networks: Vision, enabling technologies, and new paradigm shifts,” *Science China Information Sciences*, vol. 64, January 2021.
- [15] C. Diakhate, “Propagation channel modeling at centimeter and millimeter wave frequencies in 5G urban microcellular context,” Ph.D. dissertation, Communities of universities and institutions (ComUE), September 2019.
- [16] W. Hong, Z. H. Jiang, C. Yu, D. Hou, H. Wang, C. Guo, Y. Hu, L. Kuai, Y. Yu, Z. Jiang, Z. Chen, J. Chen, Z. Yu, J. Zhai, N. Zhang, L. Tian, F. Wu, G. Yang, Z.-C. Hao, and J. Y. Zhou, “The role of millimeter-Wave technologies in 5G/6G wireless communications,” *IEEE Journal of Microwaves*, vol. 1, January 2021.
- [17] K. Sakaguchi, T. Haustein, S. Barbarossa, E. C. Strinati, A. Clemente, G. Destino, A. Pärssinen, I. G. Kim, H. S. Chung, J. Kim, W. Keusgen, R. J. Weiler, K. Takinami, E. Ceci, A. S. Sadri, L. Xian, A. Maltsev, G. K. Tran, H. Ogawa, K. Mahler, and R. W. Heath, “Where, when, and how mmWave is used in 5G and beyond,” *IEICE Transactions on Electronics*, pp. 790–808, April 2017.
- [18] 3GPP, “5G; System architecture for the 5G System (5GS),” 3rd Generation Partnership Project (3GPP), Technical Specification, September 2021.
- [19] Qualcomm, “2020 IEEE radio and wireless week,” in *2020 IEEE Topical Conference on RF/Microwave Power Amplifiers for Radio and Wireless Applications (PAWR)*, March 2020.
- [20] C. Keerthi, B. Sunella, P. Jyothi, and M. Ajay Kumar, “Novelty of millimeter Wave transceivers: The future mobile communications,” vol. 8, pp. 88 – 96, February 2023.
- [21] E. Ali, M. Ismail, R. Nordin, and N. F. Abdulah, “Beamforming techniques for massive MIMO systems in 5G: Overview, classification, and trends for future research,” *Frontiers of Information Technology & Electronic Engineering*, vol. 18, June 2017.
- [22] D. d. S. Brilhante, J. C. Manjarres, R. Moreira, L. de Oliveira Veiga, J. F. de Rezende, F. Müller, A. Klautau, L. Leonel Mendes, and F. A. P. de Figueiredo, “A literature survey on AI-aided beamforming and beam management for 5G and 6G systems,” *Sensors*, vol. 23, April 2023.
- [23] Y.-N. R. Li, B. Gao, X. Zhang, and K. Huang, “Beam management in millimeter-Wave communications for 5G and beyond,” *IEEE Access*, vol. 8, January 2020.
- [24] T. S. Rappaport, S. Sun, R. Mayzus, H. Zhao, Y. Azar, K. Wang, G. N. Wong, J. K. Schulz, M. Samimi, and F. Gutierrez, “Millimeter Wave mobile communications for 5G cellular: It will work!” *IEEE Access*, vol. 1, May 2013.
- [25] T. S. Rappaport, R. W. Heath Jr., R. C. Daniels, and J. N. Murdock, *Millimeter Wave Wireless Communications*, 1st ed. Pearson Education, June 2014.
- [26] A. Saleem, X. Zhang, Y. Xu, U. A. Albalawi, and O. S. Younes, “A critical review on channel modeling: Implementations, challenges and applications,” *Electronics*, vol. 12, September 2023.

- [27] A. Weissberger, "New ITU report in progress: Technical feasibility of IMT in bands above 100 GHz (92 GHz and 400 GHz)," International Telecommunication Union (ITU), Tech. Rep., July 2023.
- [28] A. S. Seraj, "Study on propagation characteristics of 5G millimeter-Wave wireless communication systems for dense urban environments," *Department of Computer Science and Communications Engineering, Waseda University*, February 2019.
- [29] S. Sun, T. S. Rappaport, M. Shafi, P. Tang, J. Zhang, and P. J. Smith, "Propagation models and performance evaluation for 5G millimeter-Wave bands," *IEEE Transactions on Vehicular Technology*, vol. 67, June 2018.
- [30] S. Jana, A. Mishra, and M. Khan, "Evaluation of visualization algorithms for commsense system," June 2022, pp. 1–5.
- [31] I. A. Hemadeh, K. Satyanarayana, M. El-Hajjar, and L. Hanzo, "Millimeter-Wave communications: Physical channel models, design considerations, antenna constructions, and link-budget," *IEEE Communications Surveys & Tutorials*, vol. 20, December 2017.
- [32] M. Talib, N. B. M. Aripin, N. S. Othman, and A. H. Sallomi, "Comprehensive overview on mmWave communications for 5G networks concentrating on propagation models for different urban environments," *Journal of Physics: Conference Series*, vol. 2322, August 2022.
- [33] V. Nurmela, A. Karttunen, A. Roivainen, L. Raschkowski, V. Hovinen, J. Y. EB, N. Omaki, K. Kusume, A. Hekkala, R. Weiler *et al.*, "METIS channel models (D1.4)," *Mobile and wireless communications Enablers for the Twenty-twenty Information Society (METIS)*, vol. 1, February 2015.
- [34] C.-X. Wang, J. Bian, J. Sun, W. Zhang, and M. Zhang, "A survey of 5G channel measurements and models," *IEEE Communications Surveys & Tutorials*, vol. 20, August 2018.
- [35] R. J. Weiler, M. Peter, W. Keusgen, A. Maltsev, I. Karls, A. Pudeyev, I. Bolotin, I. Siaud, and A.-M. Ulmer-Moll, "Quasi-deterministic mmWave channel models in MiWEBA," *EURASIP Journal on Wireless Communications and Networking*, March 2016.
- [36] E. I. Adegoke, E. Kampert, and M. D. Higgins, "Empirical indoor path loss models at 3.5 GHz for 5G communications network planning," in *2020 International Conference on UK-China Emerging Technologies (UCET)*, August 2020.
- [37] 3GPP, "5G; Study on channel model for frequencies from 0.5 to 100 GHz," 3rd Generation Partnership Project (3GPP), Technical Report (TR) 38.901 Release 16, September 2021.
- [38] E. Basar, M. Di Renzo, J. De Rosny, M. Debbah, M.-S. Alouini, and R. Zhang, "Wireless communications through reconfigurable intelligent surfaces," *IEEE Access*, vol. 7, July 2019.
- [39] C. Cai, X. Yuan, W. Yan, Z. Huang, Y.-C. Liang, and W. Zhang, "Hierarchical passive beam-forming for reconfigurable intelligent surface aided communications," *IEEE Wireless Communications Letters*, June 2021.
- [40] S. A. H. Mohsan, M. Khan, M. Alsharif, P. Uthansakul, and A. Solyman, "Intelligent reflecting surfaces assisted UAV communications for massive networks: Current trends, challenges, and research directions," July 2022.
- [41] A. Li, S. Singh, and D. Sievenpiper, "Metasurfaces and their applications," *Nanophotonics*, June 2018.

- [42] Z. Fang, H. Li, Y. Chen, S. Sun, S. Xiao, Q. He, and L. Zhou, "Deterministic approach to design passive anomalous-diffraction metasurfaces with nearly 100 percent efficiency," *Nanophotonics*, March 2023.
- [43] C. Anjinappa, F. Erden, and I. Guvenc, "Base station and passive reflectors placement for urban mmWave networks," November 2020.
- [44] W. A. Gulzar Khawaja, O. Ozdemir, F. Erden, I. Guvenc, M. Ezuma, and Y. Kakishima, "Effect of passive reflectors for enhancing coverage of 28 GHz mmWave systems in an outdoor setting." 2019 IEEE Radio and Wireless Symposium (RWS), January 2019.
- [45] A. Rodriguez-Molares, A. Fatemi, H. Torp, and L. Løvstakken, "Adaptive beamforming based on Snell's law of reflection," in *2016 IEEE International Ultrasonics Symposium (IUS)*, September 2016.
- [46] Özdogan, E. Björnson, and E. G. Larsson, "Intelligent reflecting surfaces: Physics, propagation, and pathloss modeling," *IEEE Wireless Communications Letters*, vol. 9, December 2019.
- [47] K. Ntontin, D. Selimis, A.-A. A. Boulogeorgos, A. Alexandridis, A. Tsolis, V. Vlachodimitropoulos, and F. Lazarakis, "Optimal reconfigurable intelligent surface placement in millimeter-Wave communications," in *European Conference on Antennas and Propagation (EuCAP)*, April 2021.
- [48] W. Tang, M. Z. Chen, X. Chen, J. Y. Dai, Y. Han, M. Di Renzo, Y. Zeng, S. Jin, Q. Cheng, and T. J. Cui, "Wireless communications with reconfigurable intelligent surface: Path loss modeling and experimental measurement," *IEEE Transactions on Wireless Communications*, vol. 20, 2021.
- [49] L. Bariah, L. Mohjazi, S. Muhamadat, P. C. Sofotasios, G. K. Kurt, H. Yanikomeroglu, and O. A. Dobre, "A prospective look: Key enabling technologies, applications and open research topics in 6G networks," *IEEE Access*, vol. 8, August 2020.
- [50] R. Alghamdi, R. Alhadrami, D. Alhothali, H. Almorad, A. Faisal, S. Helal, R. Shalabi, R. Asfour, N. Hammad, A. Shams, N. Saeed, H. Dahrouj, T. Y. Al-Naffouri, and M.-S. Alouini, "Intelligent surfaces for 6G wireless networks: A survey of optimization and performance analysis techniques," *IEEE Access*, vol. 8, October 2020.
- [51] Y. Zhao, J. Zhao, W. Zhai, S. Sun, D. Niyato, and e. K. Lam, Kwok-Yan", "A survey of 6G wireless communications: Emerging technologies," in *Advances in Information and Communication. Future of Information and Communication Conference (FICC) 2021*, April 2021.
- [52] W. Saad, M. Bennis, and M. Chen, "A vision of 6G wireless systems: Applications, trends, technologies, and open research problems," *IEEE Network*, vol. 34, October 2020.
- [53] G. vom Boegel, A. Sezgin, N. Pohl, M. Vossiek, M. Weimer, J. Wessel, C. Wietfeld, R. Thill, T. T. Braun, M. Haferkamp, S. S. Sivadevuni, T. Koegel, S. Häger, S. Boecker, and J. Geiss, "6GEM perspective on joint communication and sensing," in *WSA & SCC 2023; 26th International ITG Workshop on Smart Antennas and 13th Conference on Systems, Communications, and Coding*, April 2023.
- [54] M. Z. Chowdhury, M. Shahjalal, S. Ahmed, and Y. M. Jang, "6G wireless communication systems: Applications, requirements, technologies, challenges, and research directions," *IEEE Open Journal of the Communications Society*, July 2020.

- [55] F. Liu, Y. Cui, C. Masouros, J. Xu, T. X. Han, Y. C. Eldar, and S. Buzzi, "Integrated sensing and communications: Toward dual-functional wireless networks for 6G and beyond," *IEEE Journal on Selected Areas in Communications*, March 2022.
- [56] Q. Zeeshan, D. Yunfeng, A. Kamran, A. Rafique, and K. Nisar, "Stealth considerations for aerodynamic design," *International Journal of Computer Aided Drafting, Design and Manufacturing*, January 2009.
- [57] M. Rezende, I. Martin, M. Miacci, and E. Nohara, "Radar cross section measurements (8-12 GHz) of flat plates painted with microwave absorbing materials," vol. 1, February 2001.
- [58] H. Hamd, H. Hatem, and W. Mohamed, "Evaluation of bistatic and monostatic RCS for simple and complex targets in X-band," *International Journal of Microwave and Optical Technology*, vol. 15, pp. 583–591, January 2021.
- [59] L. Leyva, D. Castanheira, A. Silva, A. Gameiro, and L. Hanzo, "Cooperative multiterminal radar and communication: A new paradigm for 6G mobile networks," *IEEE Vehicular Technology Magazine*, October 2021.
- [60] A. Neubauer, *Design of 3D-Reflectors for Near Field and Far Field Problems*. Springer New York, April 1997, pp. 101–118.
- [61] J. E. Hansen, *Spherical near-field antenna measurements*. The Institution of Engineering and Technology, January 1988, vol. 26.
- [62] J. Baldauf, S.-W. Lee, L. Lin, S.-K. Jeng, S. Scarborough, and C. Yu, "High frequency scattering from trihedral corner reflectors and other benchmark targets: SBR versus experiment," *IEEE Transactions on Antennas and Propagation*, vol. 39, September 1991.
- [63] B. Brock and A. Doerry, "Radar cross section of triangular trihedral reflector with extended bottom plate," pp. 1–38, June 2009.

List of Figures

1.1 mmWave communication links from the transmitter (TX) to two differently positioned receivers (RXs): (a) RX1 in LOS has a good connection, whereas RX2 in NLOS cannot connect to the network. In (b) we illustrate how a metasurface that is mounted in the vicinity of the transceivers provides VLOS connectivity to the NLOS RX.	1
2.1 Illustration of typical deployment of mmWave communications with use cases and future applications with the communication established between macrocell base stations at sub-6 GHz to the microcell base stations [16, 17].	4
2.2 Illustration of a simple communication system with the transmitter Tx with gain G_{Tx} in LOS path with Rx1 with gain G_{Rx1} and NLOS path with Rx2 with gain G_{Rx2} . The sample CIR graphs on the right include both the LOS and NLOS paths for the general grasp of the idea [27].	7
2.3 Free-space path loss propagation in dB as a function of Tx-Rx distance in m for the LOS condition at 38 GHz, 28 GHz, and 2 GHz frequency. A notable decrease in the path loss is observed as the frequencies decrease.	9
2.4 Illustration of 6G downlink transmission without (left) and with metasurface (right). In this work, we are particularly interested in deploying IRSs to enable efficient communication in NLOS regimes by using two LOS subchannels.	12
2.5 Design and architecture of IRS with an array of active elements where the transmitted wave is reflected in a controllable manner in the reflection region for the overall dimensions of $(M \times a) \cdot (N \times b)$	13
2.6 Illustration of HELIOS reflector arrays with different dimensions, sizes, and slope angles, showcasing the high degree of flexibility of the model.	15
2.7 Horizontal and vertical tilting of the reflecting surface enables deliberate steering of the reflection towards the desired direction.	16
2.8 Plane wave impinges along direction \mathbf{k} on reflecting surface in y - z -plane with elevation angle θ_{el} and azimuth angle φ_{az} in deg.	18
2.9 Illustrating the setup of the IRS model with the 3D angles for the transmitted and reflected wave [46].	20
2.10 Investigation of path loss at 3 GHz for three different IRS sizes when $\theta_{Rx} = 60^\circ$. One can observe that, the larger the reflector size the better it can compensate for path loss and also realize a more narrow reflection.	22
2.11 Considered setup of the IRS model with NLOS conditions between the transceivers and an IRS-based virtual LOS connectivity [47].	23
2.12 Illustration of the geometry of IRS-based channel and definitions used in the derivation of IRS channel model in [48].	25
2.13 Gain at the reflector in dB depicting the comparative results of the three IRS models [46–48] at 28 GHz frequency, $a = b = 50 \cdot \lambda$, $\theta_{Tx} = \varphi_{Tx} = 0^\circ$, and $\theta_{Rx} = 0^\circ$ with sweep along φ_{Rx}	28

2.14 Gain at the reflector depicting the support of radiation pattern in [46] when sweeping along the receiver i.e., $\gamma_{Rx} \neq \gamma_{Dev}$ for different placement of the receiver γ_{Rx} . A notable peak is observed for each γ_{Rx} curve and the curve gradually decreases after this point. Additional parameters, $a = b = 50 \cdot \lambda$ at 28 GHz frequency and $\theta_{Tx} = \varphi_{Tx} = 0^\circ$.	29
3.1 Illustration of the EM simulation workflow of the HELIOS reflectors. Simulation parameters in terms of base station configuration, far-field settings, and HELIOS reflector may be changed as desired for each simulation using an automation script.	32
3.2 HELIOS module with the implementation of α and β slope angles with incident wave orthogonal to the reflector base i.e., $\theta_{Tx} = \varphi_{Tx} = 0^\circ$ and reflected wave validating HELIOS concept [10] with two times shift in the slope angles.	34
3.3 Assessment of the peak reflection angle given $\varphi_{Tx} = \theta_{Tx} = 0^\circ$ and different module slopes. We observe that reflection angle $\varphi_{Rx} = -\varphi_{Tx} + 2 \cdot \alpha$ and we note that the saturation for slopes $< 45^\circ$ is misleading as this depends on the angle of arrival of the incident wave and, in particular, is caused by the maximum reflection angle being outside the specified observation angle range for the simulation. This is because the energy is reflected behind the reflector as sketched on the right side.	34
3.4 Illustration of the impact of the variations in reflector sizes of HELIOS module on the beam pattern and peak gain at the reflector as the size increases.	35
3.5 The influence of a reflecting surface on gain for various materials based on their conductivity and relative permittivity.	36
3.6 Geometric relation between HELIOS footprint size given by $(a \cdot b)$, and reflecting surface size given by $(a \cdot \sqrt{1 + \tan^2(\alpha)} \cdot b \cdot \sqrt{1 + \tan^2(\beta)})$, where a and b are the length and width of the module.	40
3.7 Comparison of peak RCS value yielded by simulation and analytical model for rectangular ($10\text{ cm} \times b$) and quadratic ($b \times b$) HELIOS module footprints, where we observe a matching behavior. Further parameters: $\varphi_{Tx} = \theta_{Tx} = 0^\circ$ and, $\alpha_{m,n} = \beta_{m,n} = 10^\circ$.	41
3.8 Validating the HELIOS concept along azimuth and elevation angle at the receiver and highlighting the similarities and differences between simulated and analytical models for a HELIOS module when $a = 10\text{ cm}$, $b = 20\text{ cm}$, $\alpha = 10^\circ$, and $\beta = 5^\circ$, and both $\varphi_{Tx} = \theta_{Tx} = 0^\circ$. A notable match in the peak gain is observed between the simulation results and the analytical model.	42
3.9 Sample RCS pattern of individual HELIOS module (1×1): (left) analytical model, (right) EM simulations for parameters $a = b = 10\text{ cm}$ and $\alpha = \beta = 10^\circ$ at 28 GHz frequency with peak gain of 10.4 dB.	43
3.10 Sample RCS pattern of individual HELIOS module (1×1): (left) analytical model, (right) EM simulations for parameters $a = b = 10\text{ cm}$ and $\alpha = \beta = 10^\circ$ at 38 GHz frequency with peak gain of 13.0 dB.	43
3.11 Plot against HELIOS array and maximum gain between simulated and analytical model highlighting the difference in gain in dB for the case when $\alpha_{m,n} = \beta_{m,n} = 10^\circ$ and $a_{m,n} = b_{m,n} = 10\text{ cm}$ for $M = N \in [1 : 8]$ at 28 GHz frequency.	45
3.12 RCS pattern behavior of HELIOS reflectors with different number of modules for simulation and analytical model highlighting the similarities in gains and beam patterns without the consideration of diffraction effect for $\alpha_{m,n} = \beta_{m,n} = 10^\circ$ and $a_{m,n} = b_{m,n} = 10\text{ cm}$.	46

3.13 Gain vs ECDF plot for 2×2 and 8×8 HELIOS array with $a_{m,n} = b_{m,n} = 10$ cm for simulated and analytical results with a notable difference in gain between both the models when slope angles $\alpha_{m,n} = \beta_{m,n} = 10^\circ$ with incident angles $\theta_{Tx} = \varphi_{Tx} = 0^\circ$	47
3.14 Illustrating the RCS behavior of a HELIOS module and HELIOS array for different beamwidth correction factors in comparison with the simulated results when $\alpha_{m,n} = \beta_{m,n} = 10^\circ$ and $a_{m,n} = b_{m,n} = 10$ cm for $M = N \in [1, 4]$	48
3.15 Illustrating the impact of different beamwidth correction factors in comparison with the simulations when $\alpha_{m,n} = \beta_{m,n} = 0^\circ$ for a single big flat plate with $a_{m,n} = 40$ cm, and $b_{m,n} = 10$ cm and multiple small flat plates with $a_{m,n} = b_{m,n} = 10$ cm, where both the cases 1×1 and 1×4 represent the same physical plate. Notably, with beamwidth factor of $(\frac{1}{2}, \frac{1}{2})$, and $(\frac{M}{2}, \frac{N}{2})$, there's a match with the simulations at 1×1 , but at 1×4 HELIOS reflectors, the match is observed with beamwidth factor $(\frac{M}{2}, \frac{N}{2})$	49
3.16 Violin plot comparison for a flat plate scenario for different beamwidth correction factors. (a) A single big flat plate with $a_{m,n} = 40$ cm, and $b_{m,n} = 10$ cm, and a notable match with EM simulations with beamwidth factor of $(\frac{1}{2}, \frac{1}{2})$, and $(\frac{M}{2}, \frac{N}{2})$ with no overpredictions. (b) 4 small flat plates with $a_{m,n} = b_{m,n} = 10$ cm and a match with the simulations with beamwidth factor $(\frac{M}{2}, \frac{N}{2})$ with no overpredictions. Both the cases 1×1 and 1×4 represent the same physical plate.	49
3.17 Violin plots illustrating the $\Delta Gain = RCS_{Sim} - RCS_{Anal}$, in dB for different beamwidth correction factors along the x -axis and varying HELIOS size scaling factors K along the four subfigures. Here, $\varphi_{Tx} = \theta_{Tx} = 0^\circ$, $\beta_1 = \dots = \beta_{32} = 0^\circ$, and $\alpha_1 = \dots \alpha_{32} = 27.6^\circ$	50
3.18 Comparing peak RCS value for φ_{Rx} , $\theta_{Rx} \in [-90, 90]^\circ$ range between analytical model and EM simulations along different reflecting surface size. Parameters: $\varphi_{Tx} = \theta_{Tx} = 0^\circ$, 1×32 HELIOS with $\alpha_{m,n} = \beta_{m,n} = 0^\circ \forall n \in 1, \dots, N$	51
3.19 Pairwise realization of shadowing region η_a, η_b along y and z axis for incident wave $(\theta_{Tx}, \varphi_{Tx})$ along the edge for a sample HELIOS array of 2×2 along row and column.	53
3.20 Different cases of pairwise realization for simple cases with current and neighboring slope angles $\alpha_{m,n}$, and $\alpha_{m,n+1}$. (a) Both positive slope angles (b) Both negative slope angles (c) Positive-negative slope angles (d) Negative-positive slope angles.	53
3.21 Depiction of the shadowing factor $\eta_{a_{m,n}}$ for the case when the incident angles $\theta_{Tx} = 0^\circ$, $\varphi_{Tx} > 0^\circ$ and the slope angles $\alpha_{m,n}$, and $\alpha_{m,n+1}$ are positive with $a_{m,n}$ and $a_{m,n+1}$. Here, $h_{m,n}$ and $h_{m,n+1}$ are the heights of the current and neighboring reflectors.	54
3.22 Plot depicting the amount of region shadowed for different incident azimuth angles $\varphi_{Tx} \in [-90 : 90]^\circ$ for simple case with $\alpha_{m,n} = \alpha_{m,n+1} = 10^\circ$ and $a_{m,n} = b_{m,n} = 10$ cm while $\beta_{m,n} = 0^\circ$, and $\theta_{Tx} = 0^\circ$	57
3.23 Plot against HELIOS array and maximum gain between simulated and analytical model after the elimination of the shadowed region, highlighting the difference in maximum gain in dB for the case when $a_{m,n} = b_{m,n} = 10$ cm and $\alpha_{m,n} = \beta_{m,n} = 10^\circ$	57
4.1 Methodological flowchart of this section's HELIOS computing time assessment comparing EM simulations and our analytical model for $m \in 1, \dots, M$, $n \in 1, \dots, N$	60
4.2 Mean computing time for a HELIOS module with different angular resolutions focusing on the speed-up factor X between different processors. Here, we find that the analytical model implementation is up to ca. 14,600 times faster than the EM simulations with 4 core and ca. 8,740 times faster than 128 core at 0.5° angular resolution.	61

4.3	Mean computing time analysis for a HELIOS module (1×1) with varying angular resolutions highlighting the speed-up factors X between varying reflector sizes. Notably, as the reflector size increases, the mean computing time also increases in EM simulations with 4 core, but analytical model shows very little impact for varying sizes.	61
4.4	Mean computing time analysis for various HELIOS reflector array sizes ($1 \times 1, 2 \times 2$, and 4×4) highlighting the speed-up factor X between different angular resolutions. A notable faster performance by the analytical model is observed for the large-scale array configurations as compared to that of the simulation model.	63
4.5	Illustration of urban scenario [10] with a well-aligned LOS path from the base station to the reflector center. The scenario highlights the reflections from the $3\text{ m} \times 3\text{ m}$ reflector mounted on the building to serve the NLOS south street canyon region, as depicted.	64
4.6	Top view illustration of original "narrow beam" and "broad beam" configuration for 1×32 HELIOS. We note that due to the symmetry of the original work, we adopt the flipped indices order.	66
4.7	Sample illustration of received power analysis in the urban scenario to highlight the region of interest, i.e., south street canyon, where received power is greater than receiver sensitivity and the outage region.	66
4.8	Comparison between predicted path loss of FSPL and radar equations over the total distance between Tx and Rx. For the radar equation curve, we assume LOS connectivity for the first 50 m. Thereafter, it holds $\sigma_{Meta} = 0\text{ dB}$, $r_{Tx,Ref} = 50\text{ m}$ and $r_{Ref,Rx} = r_{Tx,Rx}$	67
4.9	RCS comparison heatmaps between the HELIOS analytical model and EM simulation results in urban scenarios highlighting the gain behavior for both narrow and broad beams. Notably, a concentrated single lobe appears in narrow beam HELIOS, as the beams are focused in one direction at $(\theta_{Rx}, \varphi_{Rx}) = (-2.5^\circ, -25.75^\circ)$, whereas with broad beam HELIOS, we observe multiple side lobes.	68
4.10	ECDF vs gain at the reflector plot for narrow and broad beam HELIOS highlighting the difference along the mean between simulated results and analytical model in dB. The parameters are considered from Tab. 4.4 at 28 GHz frequency.	69
4.11	RCS comparison of narrow beam HELIOS (left column) and broad beams HELIOS (right column) in an urban scenario depicting the gain in dB (top row) and maximum power received in dBm (bottom row). The parameters are considered from Tab. 4.4 at 28 GHz frequency. Notably, the power is radiating in the direction of south street canyon with a peak gain of 15.4 dB with narrow beam and 11.2 dB with broad beam.	70
4.12	Power received RCS heatmap depicting the search for optimal slope angles to form narrow beams in the south street canyon of the urban scenario, resulting in the maximum power received at slope angle $\alpha = 30.2^\circ$ and $\beta = 4.2^\circ$, as depicted by the small black box.	72
4.13	RCS received power depicting the search for optimal slope angles to form a broad beam in the south street canyon of the urban scenario. The 32 reflectors take seven different slope angles in the step of 2.5° with $\alpha = 20.2^\circ$ and $\beta = -10.2^\circ$ being its first value, where the maximum receive power is at this location.	72
4.14	RCS comparison of narrow beam HELIOS (left column) and broad beams HELIOS (right column) in an urban scenario depicting the gain in dB (top row) and maximum power received in dBm (bottom row). The parameters are considered from Tab. 4.4 at 28 GHz frequency with the optimized slope angles.	73

4.15 RCS comparison of optimized narrow beam HELIOS (left column) and broad beams HELIOS (right column) in an urban scenario depicting the gain in dB (top row) and maximum power received in dBm (bottom row). The parameters are considered from Tab. 4.4 at 28 GHz frequency with the optimized slope angles at the edge of the building.	75
4.16 RCS comparison of two cases of IRS model 1 (Sec. 2.3.3): fixed beam case on the left column and dynamic beam on the right column in an urban scenario depicting the gain in dB (top row) and maximum power received in dBm (bottom row). The parameters are considered from Tab. 4.4 at 28 GHz frequency with the optimized slope angles at the edge of the building.	76
4.17 RCS comparison of IRS model 2 (left column) and IRS model 3 (right column) (Sec. 2.3.3) in an urban scenario depicting the gain in dB (top row) and maximum power received in dBm (bottom row). The parameters are considered from Tab. 4.4 at 28 GHz frequency with the optimized slope angles at the edge of the building.	77
4.18 ECDF plot depicting the power received in the south street canyon thus showcasing the performance of HELIOS and IRSs as predicted by analytical models, cf. Sec. 2.3.3 ([46–48]). Notably, the optimized broad beam HELIOS (geometry configuration + mounting position) shows more than 80.2 % percentage coverage in our region of interest, while the fixed beam case of IRS model 1 exhibits 13.3 % coverage. Our optimization increased the mean receive power by 55.5 dB against [10]. However, when compared to IRS which may reconfigure the reflection such that any position in the range is deliberately targeted, we still observe on average tens of dB of loss as well as reduced coverage.	79
4.19 Variation of peak gain for span in frequency range $f \in [0.4 : 71]$ GHz in the steps of 0.1 GHz. Three distinct frequency ranges depend on the peak gain values as depicted with color coding. Higher gains are observed in the green region showcasing the better performance of the HELIOS reflectors in this frequency range.	80
4.20 RCS comparison of optimized narrow beam HELIOS (Geometry configuration+ mounting position) at 2 GHz, 28 GHz, and 48 GHz frequency in an urban scenario depicting the gain in dB (top row) and maximum power received in dBm (bottom row).	81
4.21 Comparison between predicted LOS, NLOS path loss of UMi channel model, and the radar equation over the total distance between Tx and Rx. For the radar curve, we assume LOS connectivity for the first 50 m, as the reflector is located at 50 m from Tx. Thereafter, it follows the radar path with $\sigma_{Meta} = 0$ dB and $r_{Tx,Rx} = r_{Ref,Rx}$	82
4.22 UMi channel model RCS comparison of optimized narrow beam HELIOS (left column) and broad beams HELIOS (right column) in urban scenario depicting maximum power received in dBm. The parameters are considered from Tab. 4.4 at 28 GHz frequency with the optimized slope angles at the edge of the building, see Sec. 4.2.5.	83
4.23 UMi channel model RCS comparison of two cases of IRS model 1 (Sec. 2.3.3): fixed beam case on the left column and dynamic beam on the right column in an urban scenario depicting maximum power received in dBm. The parameters are considered from Tab. 4.4 at 28 GHz frequency with the optimized slope angles at the edge of the building, see Sec. 4.2.5.	83
4.24 UMi channel model RCS comparison of two IRS models Sec. 2.3.3 in urban scenario depicting maximum power received in dBm. The parameters are considered from Tab. 4.4 at 28 GHz frequency with the optimized slope angles at the edge of the building, see Sec. 4.2.5.	84

4.25 ECDF plot depicting the power received in the south street canyon in dBm by UMi channel model in urban scenario, highlighting the performance and coverage by our optimized HELIOS analytical model and IRS models [46–48] in Sec. 2.3.3. Notably, optimized HELIOS broad beam around the edge of the building shows more than 98.6 % percentage coverage in our region of interest, while fixed beam case of IRS model 1 exhibits 91.4 % coverage.	84
4.26 Illustration of the squared and triangle geometry models with different triangular orientations with their RCS behavior depicting the gain in dB. Assuming the flat plate geometry with $\varphi_{Tx} = \theta_{Tx} = 0^\circ$, the color coding on the geometry of square and triangle can be seen on the RCS heatmap, denoting the impact of the different sides of the geometry on the RCS behavior, which is the same for various orientations of the triangular plate.	86
4.27 Gain behavior in dB for the rectangle and triangle plate when $a = b = 0.1\text{ m}$, and $\varphi_{Tx} = \theta_{Tx} = 0^\circ$. The main difference between the two plates is with their areas, due to which we observe 6 dB between these models as depicted.	87

List of Tables

2.1	mmWave channel modeling efforts by different organizations with their operating frequencies and the kind of propagation models that they support.	8
2.2	UMi path loss model for LOS and NLOS conditions with their applicability parameters that can be deemed to be suitable for many scenarios as defined by 3GPP [37].	11
2.3	UMa path loss model for LOS and NLOS conditions with their applicability parameters that can be deemed to be suitable for many scenarios as defined by 3GPP [37].	12
2.4	Comprehensive standardization of parameters: Units and abbreviations for meta-surface channel modeling across the entire thesis.	19
2.5	Gains at the reflector from the three IRS models [46–48] which are derived from the respective receive power equations.	27
2.6	Characterization of IRS gain models [46–48] with their parameter dependencies at 28 GHz frequency. The green and red boxes depict the similarities and dissimilarities between the three IRS models, respectively.	28
3.1	Properties of different materials in terms of conductivity and relative permittivity. . . .	36
3.2	Standard RCS values which are commonly observed [56, 57].	38
3.3	Comparing the existing equation for flat plate, cf. Eq. (3.5) which is used for the adaptation of our RCS equation for the HELIOS analytical module, cf. Eq. (3.6), focusing on the changes implemented.	39
3.4	Shadowed region for the first reflector along the row and column for cases in Fig. 3.20.	55
3.5	Shadowed region for the second reflector along the row and column for cases in Fig. 3.20.	56
4.1	Mean computing time for a HELIOS module (1×1) with different angular resolutions of the bistatic RCS.	60
4.2	Mean computing time for different angular resolutions depicting variations for varying reflector sizes for a HELIOS module. We observe that the analytical model's computing time is independent to the reflector dimensions whereas the EM simulations scale poorly, thus demonstrating infeasibility for large reflecting surfaces size as expected for 6G, cf. case study in Sec. 4.2.	62
4.3	Mean computing time for various HELIOS reflector array sizes (1×1 , 2×2 , and 4×4) with different angular resolutions. A notable performance of our analytical model in ms for an increase in reflector array demonstrates the advantage of the model to assess large-scale HELIOS configurations as compared to the simulation models. Parameters: $a_{m,n} = b_{m,n} = 10$ cm.	62
4.4	Key parameters and their values at transmitter, receiver, and the reflector applicable to the urban street corner scenario at 28 GHz frequency.	65